Artificial non-Gaussian operations and states for quantum information processing applications

Dissertation thesis by

Jan Provazník

Palacký University
Olomouc

2024

Abstract: Quantum non-Gaussian operations are one of the essential ingredients needed for universal quantum computation with continuous-variable quantum states of light. The scarcity of naturally occurring non-Gaussian interactions can be compensated with suitable measurement-induced non-Gaussian operations. Their implementations still require high-quality quantum non-Gaussian states that can be manufactured artificially with various techniques of quantum state synthesis.

Several original research papers are covered in this dissertation, starting with a proposal for improved single photon subtraction procedure which can be utilized within specific protocols for state synthesis and in entanglement distillation. Another avenue of research focuses on preparation of ancillary non-Gaussian states needed in measurement-induced cubic phase interaction and studies the effects of different photonic detectors on the quality of prepared physical approximations of cubic phase states. The analysis is complemented by a novel approach towards dealing with numerical issues inherent to numerical simulations of continuous-variable quantum systems.

Quantum non-Gaussian states, despite their critical role in quantum computation and communication, are susceptible to loss. A particular decoherence mitigation strategy based on Gaussian operations is presented and investigated in the dissertation. Its effects against decoherence due to loss combined with thermal noise are discussed and analyzed for the family of quantum-optical Schrödinger states of light.

Ongoing research directions presented in the dissertation include an analysis of realistic experimental conditions required for synthesis of certifiable quantum states of four photons, and a novel algorithm with exponential improvement in computational complexity is introduced for calculation of a special qualitative measure of non-Gaussian resources, enabling its application in complex scenarios.

The dissertation concludes with a brief incursion into the realm of genuine multi-partite entangled states. Certain classes of these states can be detected using optimal witnesses obtained with the aid of semi-definite programming. The pertinent semi-definite programs were implemented in collaboration with experimental group aiming to prepare and certify a special discrete-variable state of light with genuine multi-partite entanglement provable solely from its separable two-body marginals. In further theoretical collaboration similarly exotic states were discovered in the domain of continuous-variable light. These efforts eventually culminated in development of open-source software libraries presented within the dissertation.

Keywords: quantum optics, quantum states of light, quantum information processing, quantum non-Gaussianity, continuous-variables, numerical simulation, numerical optimization, cubic phase states, decoherence mitigation, coherent Schrödinger states, Fock state capability, genuine multi-partite entanglement

Acknowledgements

I am eternally grateful to my family and friends for their support. It has certainly been a long a perilous journey. I would like to thank the people I have collaborated with over the years, including, in no particular order, Olga Solodovnikova, Peter Marek, Radim Filip, Julien Laurat, Ladislav Mišta, Robert Stárek, Michal Mičuda and Olga Leskovjanová.

I have had many interesting and thought provoking scientific discussions with my friends and colleagues, some of which led to further scientific collaboration. I would like to express my gratitude to everyone who had time and patience. The list is long and incomplete and some of the names were already mentioned. I sincerely thank Barbora Šonská, Šimon Bräuer, Vojtěch Kala, Michal Matulík, Robert Stárek, Olga Leskovjanová, Olga Solodovnikova, Petr Marek, Michal Mičuda, Miroslav Ježek, Ladislav Mišta, Radim Filip, and many others.

I believe the support I have received at the Department of Optics should be rightfully recognized. I am grateful for being allowed to build the necessary computational infrastructure, without which many of the results presented in this dissertation would not be possible, at least now within the time-frame of my studies.

At last, but not least, I would like to thank my supervisor, Peter Marek, for his hard work, time, guidance and endless patience over the last years.

Contents

Introduction

Universal quantum computers hold a great promise for the future [1]. The field of quantum computation has grown, thrived and flourished in the decades since it was conceived by Feynman [2, 3]. Some of the ground-breaking advancements [4] offering significant advantages include prime factorization with polynomial time complexity [5, 6], efficient solutions to a number of algebraic problems [7], applications in machine learning [8], quadratic improvement in search complexity through unordered lists [9], and advancements in quantum simulation [10, 11] and quantum chemistry [12]. The leverage of quantum algorithms over their classical counterparts arises from their utilization of the remarkable features unique to quantum systems — quantum entanglement and quantum superposition.

Quantum computers, whether universal or not, exploit the peculiar qualities of quantum physics by encoding the information into observable physical properties of quantum objects. Quantum computation can be naturally divided into two primary types based on the spectral behavior of the employed observables. Those with discrete spectra, for example, spin and polarization, are called discrete variables, whereas continuous variables refer to properties with continuous spectra, such as position or momentum. Quantum systems with two-level discrete-variable properties are known as qubits [13], in a close analogy with bits from the classical theory of information [14], while discrete multi-level systems are generally recognized as qudits [15, 16]. The notion of universality in discrete-variable quantum computers is connected to the possibility of realizing arbitrary unitary operations between the logical qubits [3, 17, 18]. Universal quantum computation with continuous variables is understood as the ability to implement arbitrary interactions with Hamiltonians that are polynomial functions in the respective continuous-variable operators [19].

The relationship between discrete-variable and continuous-variable quantum computers is similar to the distinction between the classical digital [20] and analogue [21] computers, where the continuous-variable quantum computers effectively represent analogue quantum computers [11, 19] with applications in quantum simulation [11, 22–24]. Simulating the behavior and time evolution of general quantum systems is a notoriously difficult task for classical computers [2, 11, 25–27]. The exponential increase in computational complexity due to the extraordinary features inherent to quantum systems limits the feasibility and scope of their simulation using classical computers. Universal quantum computers offer significant advantages in the simulation of general quantum systems [2, 10, 11] because the classically challenging aspects of quantum physics, such as quantum non-linearities, quantum entanglement and quantum superposition, are intrinsic to them. In quantum analogue simulation, the dynamics of the studied quantum system can be directly mimicked using precise continuous control of the parameters within a continuous-variable quantum computer [11]. Alternatively, the time evolution can be divided into a finite sequence of small time steps in digital quantum simulation with discrete-variable quantum computers [11]. The computational advantage of quantum computers in quantum simulation is not absolute. Certain classes of quantum systems can be simulated efficiently with classical computers, ranging from those where specific conditions, such as sufficiently high loss, must be met [28–30], to those where the classical simulation is always efficient [31].

Quantum computation has been shown to be possible with various physical platforms, including atomic ensembles [32–34], trapped ions [35–40], superconducting circuits [41–47] and quantized light [48–60]. Photonic platforms made their way to the spotlight around the turn of

the century with a pair of landmark proposals [49, 50] for fault-tolerant quantum computation. One method relied solely on linear optics, high quality single photon detectors and sources of single photons [49]. The other approach proposed error correction realized with embedding of logical qubits into continuous-variable states of light [50] while only needing Gaussian operations and measurements to implement fault-tolerant computation with the embedded logical qubits and non-Gaussian interactions to achieve universality. The amalgamation of the embedding protocol [50] and measurement-based quantum computation paradigm [57, 61, 62] with continuous-variable optical cluster states [63–68] resulted in recent proposals of scalable universal fault-tolerant optical quantum computer architectures [58–60, 69–73].

Quantized light offers an extremely versatile platform. Both the discrete-variable features of individual photons and continuous-variable aspects of quantized light are utilized in applications as diverse as quantum communication [74–77], quantum key distribution [78], and quantum computation. Quantized fields of light can be modeled as collections of independent linear harmonic oscillators representing quantized modes of the field [79] with individual modes characterized by continuous-variable quadrature operators. Interaction between the modes and transformation of their quadratures is carried out by interaction with matter. Complex non-linear transformations require optical non-linearities in the material, however, optical non-linearities of higher orders are generally too weak for practical use. Moreover, their utility in direct applications is dubious [80, 81]. As a consequence, complex interactions between travelling fields of light, especially on the level of individual photons, are practically impossible. Light can be efficiently manipulated only with Gaussian operations — a superset of quantum interactions including elements of linear optics and squeezing [82] — that are unfortunately insufficient; implementation of non-Gaussian interactions is required for both analogue and fault-tolerant universal quantum computation with continuous variables [19, 50] and for endeavours such as entanglement distillation [83–85].

The scarcity of suitable naturally occurring non-Gaussian interactions can be compensated with measurement-induced operations [86–91]. Ancillary non-Gaussian states are still needed for their implementation, however, the non-Gaussian interaction no longer needs to be universal. The bespoke non-Gaussian ancillaries can be tailored exactly to their purpose and synthesized with a number of methods, for example by alternating displacement operations with single photon creation [92], interchanging displacement with single photon subtraction from a squeezed vacuum state [87, 93], performing multi-photon subtraction from squeezed states [94], generalizing the subtraction procedure [95, 96], manipulating an entangled pair and measuring one of its parts [50, 97, 98], using boson sampling [26], and employing its Gaussian variant [99–101]. Desired non-Gaussian quantum states can be also produced by combining multiple non-Gaussian resources together in intricate breeding protocols [102–105].

This dissertation introduces several research articles pertinent to preparation of artificial quantum non-Gaussian states and their characterization. The original articles are treated individually in separate chapters. An improved single photon subtraction is proposed in the first chapter with possible applications in the creation of photonic non-Gaussian resources such as the squeezed single photon state, distillation of quantum entanglement, and possibly in the state synthesis protocol based on single photon subtraction [93]. The second paper studies preparation of physical approximations of cubic-phase states using different modes of detection. These states can be employed in implementations of measurement-induced cubic phase gates acting on arbitrary photonic states. The numerical methods introduced in the paper are discussed separately. In the third paper, currently under review, protective strategies for photonic coherent Schrödinger states transmitted through noisy lossy channels are examined, aiming to mitigate the adverse effects of the hostile environment. The next two papers overview a current work in progress. The first paper of the two discusses a particular measure of non-Gaussianity and introduces an improved method of its computation with exponential decrease in computational complexity. The second paper of the two investigates the possibility of preparing photonic states of four photons under realistic experimental conditions. The final chapter reviews contributions to a couple of papers regarding genuine multi-partite entanglement in discrete-variable and continuous-variable quantum systems and the resulting software packages.

Chapter 1

Improving on Single Photon Subtraction

This chapter summarizes the article *"Loop-based subtraction of a single photon from a traveling beam of light"* [106].

Single photon subtraction, realized with a heavily unbalanced beam splitter of high transmittance and a single photon detector, is the physical approximation of the non-Hermitian field annihilation operator [93]. This subtraction procedure implements a measurement-induced non-Gaussian operation. It can be readily employed in construction of arbitrary non-Gaussian states. One of the experimentally feasible protocols for state synthesis [93] utilizes alternating sequences of Gaussian displacement and non-Gaussian single photon subtraction from squeezed vacuum to prepare arbitrary superpositions of Fock states. It was successfully used to prepare approximate low-amplitude coherent Schrödinger states [107–111]. Being a non-Gaussian operation it has applications beyond state preparation; including noiseless amplification [112, 113] and entanglement distillation [114–118].

The major disadvantage of the subtraction procedure lies in its severely limited success rate. The probability of successful subtraction scales with the reflectance of the beam splitter. In fact, a single photon is subtracted in the limit of high transmittance, making the success rate negligible and effectively rendering the procedure impractical. In the article [106] discussed in this chapter, we aimed to improve the subtraction procedure by increasing its success rate without hindering its ability to subtract single photons. Its performance was analyzed in the context of a particular entanglement distillation protocol [115] and the preparation of squeezed single photon states.

This chapter is divided into three sections; the methodology, including a brief discussion of the limitations of the standard subtraction procedure, is presented in the first section, followed by a discussion of our findings and concluded with a brief summary.

A Methodology

Single photon subtraction can be realized in a measurement-induced fashion with a heavily unbalanced beam splitter of high transmittance and a single photon detector [93]. In realistic experimental settings, the subtraction of single photon from a traveling mode of light usually relies on an avalanche photon detector (APD), rather than a true single photon detector [93]. The main difference between the two is that an APD can only distinguish between the presence of any non-zero number of photons and no photons. When the detector registers a photon, the subtraction procedure is considered successful and the remaining state of light is kept, otherwise it is discarded.

Limitations of the standard subtraction procedure

The subtraction procedure, when successful, transforms an arbitrary quantum state $\hat{\varrho}_0$ into

$$\hat{\varrho}_0' = \mathrm{tr}_1 \left[\hat{U}_{01} (\hat{\rho}_0 \otimes |0\rangle_1\langle 0|) \hat{U}_{01}^\dagger \hat{\Pi}_1^\bullet \right] , \tag{1.1}$$

The unitary evolution due to the beam splitter of transmittance τ acting on the modes labeled by 0 and 1 is expressed by the operator

$$\hat{U}_{01} = \exp\left[\kappa (\hat{a}_0 \hat{a}_1^\dagger - \hat{a}_0^\dagger \hat{a}_1) \right] \quad \text{where} \quad \kappa = \cos(\tau) , \tag{1.2}$$

where the operators $\hat{a}_k$ (with $k = 0, 1$) are the annihilation operators of the two modes . The operators satisfy the standard commutation relations $[\hat{a}_j, \hat{a}_k^\dagger] = \delta_{kj}$. The two possible outcomes of the measurement facilitated by an ideal APD are represented by their respective POVM elements,

$$\hat{\Pi}_1^\circ = |0\rangle_1\langle 0| \quad \text{and} \quad \hat{\Pi}_1^\bullet = \hat{\mathbb{1}}_1 - |0\rangle_1\langle 0| , \tag{1.3}$$

where the latter element indicates successful subtraction. When the beam splitter is strongly unbalanced ($\tau \to 1 \iff \kappa \to 0$), the unitary operator (1.2) can be replaced by its Taylor expansion up to the first order and the output state can be approximated with

$$\hat{\varrho}_0' \approx \kappa^2 \hat{a}_0 \hat{\varrho}_0 \hat{a}_0^\dagger . \tag{1.4}$$

The procedure approaches the perfect subtraction of a single photon in the limit of $\kappa \to 0$, but alas, the probability of success, given by the trace of (1.4), approaches zero as well.

Improving the subtraction procedure

The probability of success can be improved with the modification depicted in Figure 1.1. This alteration was inspired by the recent experimental proposals [119, 120]. Unlike as in the standard subtraction procedure, the quantum state is not discarded on unsuccessful subtraction attempts; it is instead looped back to the beam splitter again. The looping procedure is repeated until a photon is successfully subtracted, as indicated by the favourable detection outcome $\hat{\Pi}_n^\bullet$. If the operation does not succeed within a pre-determined number N of attempts, the state is discarded. The loop-based procedure is probabilistic, just like the standard subtraction protocol.

If the subtraction procedure succeeds in its nth step, the output state can be expressed as

$$\hat{\varrho}_0^{(n)} = \mathrm{tr}_{1,\ldots,n} \left[\hat{U}_{(n)} \left(\hat{\rho}_0 \otimes \bigotimes_{k=1}^{n} |0\rangle_k\langle 0| \right) \hat{U}_{(n)}^\dagger \hat{\Pi}_{(n)} \right] , \tag{1.5}$$

where the unitary operator $U_{(n)}$ encompasses the sequence of beam splitter operations U_{0k} between the input state and the ancillary modes k in each successive step,

$$\hat{U}_{(n)} = \bigotimes_{k=1}^{n} \hat{U}_{0k} . \tag{1.6}$$

The transmission coefficient τ of the internal beam splitter is kept constant over the course of the procedure. The collective POVM element $\Pi_{(n)}$ reflects the sequence of unsuccessful subtraction attempts until the first successful one in the nth step,

$$\hat{\Pi}_{(n)} = \bigotimes_{k=1}^{n-1} \hat{\Pi}_k^\circ \otimes \hat{\Pi}_n^\bullet . \tag{1.7}$$

The density matrix (1.5) is not normalized; its norm equals to the probability $P^{(n)} = \mathrm{tr}[\hat{\varrho}_0^{(n)}]$ of successful subtraction in the nth step. This probability necessarily converges to zero with the increasing number of steps.

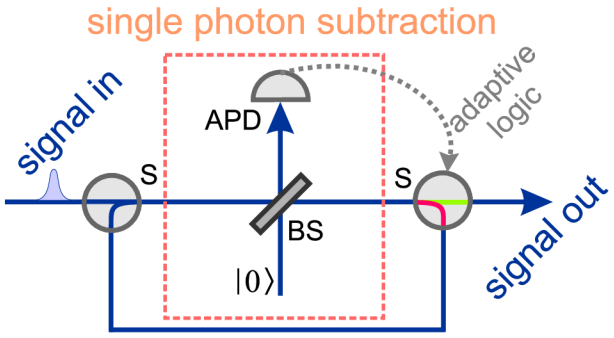

Figure 1.1. Schematic representation of the loop-based photon subtraction. Part of the input signal is tapped off at the mostly transmissive beam splitter (BS) and directed towards avalanche photo-diode (APD). Positive detection event results in successfully transformed signal while negative one prompts the optical switches (S) to feed the signal back for the next attempt if a predetermined number of maximal steps was not reached yet.

The subtraction procedure is considered successful if it succeeds within N steps. The actual step in which it succeeds is not known beforehand; the final resulting state $\hat{\varrho}_{(N)}$ is the average over all the acceptable (statistically independent) possibilities (1.5),

$$\hat{\varrho}_{(N)} = \frac{1}{P}\sum_{n=1}^{N} \hat{\varrho}_0^{(n)} \,, \tag{1.8}$$

where the overall probability of success,

$$P_{(N)} = \sum_{n=1}^{N} \mathrm{tr}[\hat{\varrho}_0^{(n)}] = \sum_{n=1}^{N} P^{(n)} \,, \tag{1.9}$$

is necessarily greater than or equal to any of the individual $P^{(n)}$ probabilities. The overall probability of successful single photon subtraction is increased at the cost of decoherence of the output state; it is now a mixture a quantum states which underwent different noiseless attenuation processes [121].

The overall probability of success (1.9) is bounded from above,

$$P_{(N)} \leq \mathrm{tr}\left[\hat{\varrho}_0 \hat{\Pi}_0^{\bullet}\right] \,, \tag{1.10}$$

by the probability of detecting any number of photons in the input state $\hat{\varrho}_0$. This is equal to reflecting all of the incident light into the detector in the first step of the subtraction procedure. For sufficiently intense states the success rate approaches one.

Taking realistic detectors with limited quantum efficiency into account

The subtraction procedure can be readily extended to account for realistic detectors available in experimental settings. Detectors limited in their quantum efficiency η can be modeled as ideal detectors where the measured state undergoes loss,

$$\mathrm{tr}\left[\Big(\sum_{k=0}^{\infty} \hat{M}_k \hat{\varrho} \hat{M}_k^{\dagger}\Big)\hat{\Pi}\right] \quad \text{where} \quad \hat{M}_k = \frac{\sqrt{1-\eta}^{\,k}}{\sqrt{k!}} \sqrt{\eta}^{\,\hat{a}^{\dagger}\hat{a}} \hat{a}^k \tag{1.11}$$

where the Kraus operators $\hat{M}_k$ describe the process of signal attenuation [122] and Π represents the respective POVM element of the ideal detector. Because the trace operation is linear and

invariant under cyclic permutation, the relation (1.11) can be equally rewritten as

$$\mathrm{tr}[\hat{\varrho}\hat{\Pi}_\eta] \quad \text{where} \quad \hat{\Pi}_\eta = \sum_{k=0}^{\infty} \hat{M}_k^\dagger \hat{\Pi} \hat{M}_k \ . \tag{1.12}$$

In the case of the APD detector, the element Π° respective to the measurement outcome when no photons are detected, is transformed into

$$\hat{\Pi}_\eta^\circ = \sum_{k=0}^{\infty} (1-\eta)^k \, |k\rangle\langle k| \ . \tag{1.13}$$

The complementary element can be simply obtained as $\hat{\Pi}_\eta^\bullet = \mathbb{1} - \hat{\Pi}_\eta^\circ$. It is possible to neglect the dark counts as they are negligibly small for high quality superconducting detectors [123]. Adapting the procedure to account for realistic detectors is trivial; the POVM elements in (1.7) are simply substituted with $\hat{\Pi}_\eta^\circ$ and $\hat{\Pi}_\eta^\bullet$.

B Discussion and results

The advantage of the loop-based subtraction procedure lies in the increased probability of success. The major drawback is the inherent decoherence of the subtracted state; it is necessarily mixed for any number of subtraction steps $N > 1$. To determine to what degree the decoherence poses an issue, the procedure was studied in three distinct applications; it was used to prepare squeezed single photon states from squeezed vacua, to facilitate parity change in coherent Schrödinger states, and to distill entanglement from a two mode squeezed vacuum state.

Producing squeezed single photon states from squeezed vacuum

Subtraction of a single photon from a pure squeezed vacuum state of light leads to creation of a squeezed single photon state. A distinctive property of this state is the negativity of its Wigner function; a hallmark feature of non-classical and quantum non-Gaussian [124–127] quantum states. Negativity generally deteriorates under decoherence; its survival was even proposed as one of the measures of non-classicality [128]. To determine the effects of the particular decoherence inflicted by our loop-based procedure, we studied the behavior of the central negativity of the prepared state, represented by the value $W(0,0)$ of its Wigner function.

We found that the proposed procedure yields a significant improvement in success probability at the cost of minimal decrease in the attainable Wigner negativity with even as little as $N = 10$ steps. It is possible to reach the maximal negativity with maximal probability of success (1.10) when using an ideal detector by taking a sufficient number of steps; realistic detectors preclude this possibility.

This is demonstrated in Figure 1.2 for the ideal case of a pure squeezed vacuum state with 6dB of squeezing and 6dB of anti-squeezing. The relation between the central negativity $W(0,0)$ of the resulting state and the overall success probability P_S is presented for different numbers of steps N. In the case of the ideal detection low numbers of allowed steps exhibit a distinctive trade-off between the achieved negativity and the probability of success. However, with increasing numbers of steps it becomes possible to approach maximal negativity at the maximal possible success rate (1.10) and the improvement is significant already for ten steps. In the case of realistic detectors with quantum efficiency $\eta = 0.8$ the maximal achievable negativity is lower; the reduced efficiency effectively acts as loss on the initial squeezed state. Consequently, the trade-off between the achievable negativity and the success probability never vanishes as in the ideal case. Nevertheless, for all values of success probability and negativity the improvement by considering multiple steps is clearly visible.

We also observed a fascinating phenomenon appearing when the operation was applied to a squeezed vacuum state which was not pure. The presence of extra noise led to larger negativity of $W(0,0)$. In the case of impure squeezed states it is possible to simultaneously increase both the

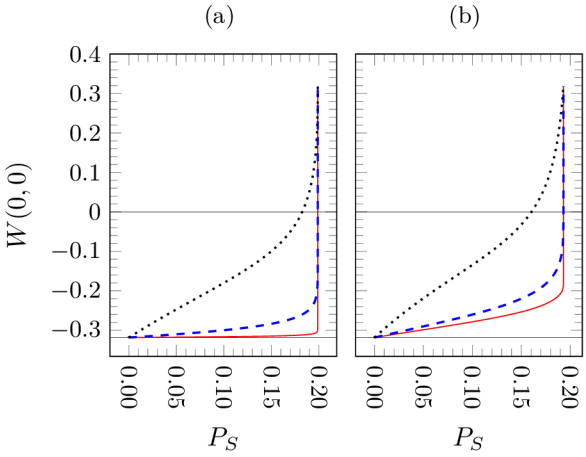

Figure 1.2. Central negativity of non-Gaussian quantum state prepared from a pure vacuum state with 6dB of squeezing relative to the achievable probability of success for (a) ideal and (b) realistic detectors with quantum efficiency $\eta = 0.8$. The performance of the original single step subtraction protocol (black dotted) is significantly surpassed by taking as little as 10 steps (dashed blue) and which can be further improved by performing 100 steps (solid red). While the improvement is significant for both the ideal and the realistic detection, the losses due to quantum inefficiency make it impossible to attain maximal negativity with maximal probability of success.

negativity and the probability of success. This behavior, which manifests for sufficiently efficient detectors and sufficiently high number of allowed steps, is illustrated in Fig. 1.3 on the case of subtraction of photon from a squeezed state with 8dB of squeezing and 10dB of anti-squeezing.

Transitions between coherent Schrödinger states

While the negativity of Wigner function is an important quantum feature, it does not provide a complete picture of the decoherence. Under ideal conditions the mixed state obtained by subtracting a single photon from the squeezed vacuum consists of states with maximal negativity at the origin of the phase space. Additional information about the effects of the decoherence inherent to our procedure can be deduced from its action on coherent Schrödinger (CS) states,

$$|\xi,\pm\rangle = \frac{|\xi\rangle \pm |-\xi\rangle}{\sqrt{2(1 \pm \exp(-2|\xi|^2))}}\,, \tag{1.14}$$

defined in terms of coherent states $|\xi\rangle$ satisfying the eigenvalue relation $\hat{a}\,|\xi\rangle = \xi\,|\xi\rangle$. Their utility in many applications, including quantum computation protocols [51, 52, 75, 102, 129–135], quantum computation protocols, quantum error correction [50, 134, 136–138], quantum communication [75, 139–141], quantum sensing [142], spectroscopy [143] and construction [50, 102, 135] of GKP states [50], stems from their non-Gaussian nature. But alas, their non-Gaussian features quickly succumb to decoherence [109, 144–149] and their superposition decays into a mixture of coherent states. Although their fragility severely limits their practical use, they make an excellent test case for our subtraction procedure.

Transitions between the two variants of the CS state, $|\xi,+\rangle$ and $|\xi,-\rangle$, are facilitated by the ideal subtraction of a single photon. We used our subtraction procedure to realize the transition $|\xi,+\rangle \mapsto |\xi,-\rangle$ and measured the quality of the resulting state $\hat{\varrho}_{(N)}$ using fidelity

$$F = \langle \xi,-|\hat{\varrho}_{(N)}|\xi,-\rangle \tag{1.15}$$

with the ideal target state $|\xi,-\rangle$. Even though fidelity is not a good quantifier of non-classical

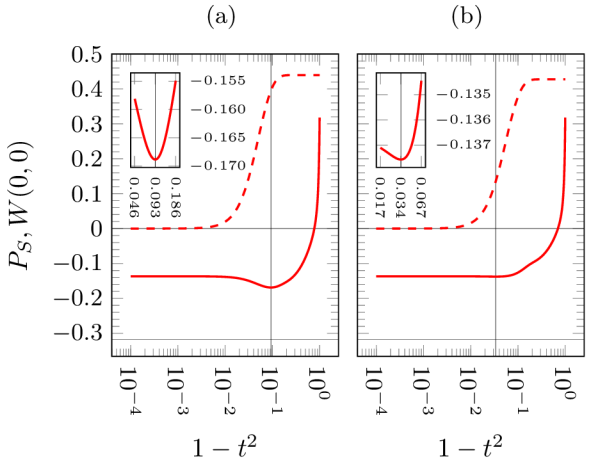

Figure 1.3. The central negativity of the Wigner function (solid red line) and the achievable probability of success (dashed red line) in relation to the transmission coefficient of the tapping beam splitter for using the (a) ideal and (b) realistic detectors with quantum efficiency $\eta = 0.8$ on an impure squeezed state with 8dB of squeezing and 10 dB of anti-squeezing. The black vertical lines mark the points in which the Wigner function negativity reaches the local minima even though the success probability is not saturated. The insets show the detail of these points. The effect becomes observable for sufficiently squeezed states after a higher number of steps; the present figure is obtained for $N = 100$ step procedure.

features in general, the finicky nature of CS states makes it sensitive even to the slightest decoherence. Its dependence on the probability of success P_S and the number of steps is illustrated in Figure 1.4. With ideal detectors, even the fragile CS states can be transformed with both fidelity and the success probability achieving the maximal values. The improvement over the standard subtraction procedure is significant already for ten steps. In the case of imperfect detectors the decoherence can not be avoided and the maximal fidelity is achievable only in the limit of $P_S \to 0$. However, already ten steps of our method lead the same fidelities with significantly higher probabilities of success.

Distillation of entanglement

Photon subtraction is a crucial part of the entanglement distillation protocols [114–118] and has been successfully demonstrated in experimental settings [116, 118, 150]. It could be substituted by other non-Gaussian operations such as photon addition [151, 152]. Because entangled states are especially susceptible to decoherence, the distillation protocols based on single photon subtraction offer another direction from which we can analyze our subtraction procedure. We consider a pure two mode squeezed vacuum (TMSV) state

$$|\psi\rangle = \sqrt{1-\lambda^2} \sum_{f=0}^{\infty} \lambda^f |f\rangle |f\rangle \tag{1.16}$$

where the coefficient $\lambda = \tanh r$ connects to the squeezing rate r. In order to increase the entanglement of the state our photon subtraction is applied to both of its modes, as depicted in Figure 1.5.

The entanglement of both the initial and the subtracted state is quantified using Gaussian logarithmic negativity [153]. While it is an inadequate measure of entanglement for non-Gaussian states and does not even establish a lower bound on the logarithmic negativity [154] of general

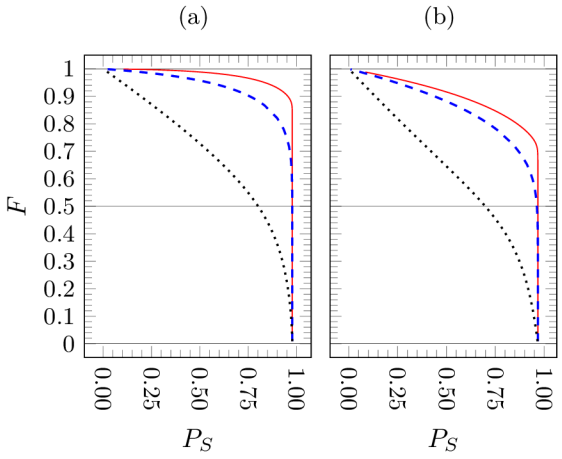

Figure 1.4. Fidelity in respect to probability of success of the $|\xi,+\rangle \mapsto |\xi,-\rangle$ transition facilitated by the subtraction procedure employing (a) ideal and (b) realistic detectors with quantum efficiency $\eta = 0.8$. The CS states $|\xi,\pm\rangle$ are investigated for realistic $\sqrt{2}\xi = 3$ in both modes of detection. Our procedure shows a significant improvement in success probability over the original subtraction protocol (dotted black) with as little as 10 steps (dashed blue). The maximal probability relative to the desired fidelity of the transition can be further increased by taking, for example, 100 steps (solid red).

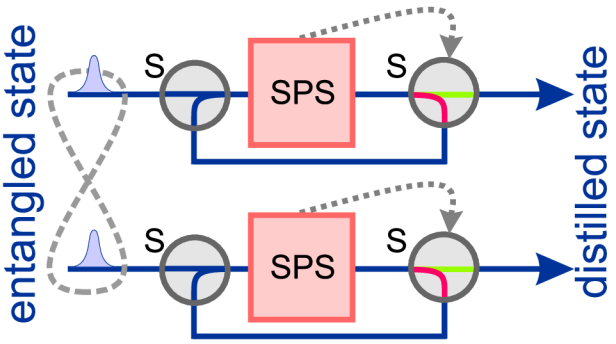

Figure 1.5. Schematic representation of the distillation of entanglement with help of the loop-based photon subtraction. Single photon subtractions (SPS, depicted in detail in Figure 1.1) are attempted at both modes of the initial entangled state. If the subtraction was not successful and a predetermined number of steps was not reached yet, the optical switches are used for feeding the signal back for the next attempt.

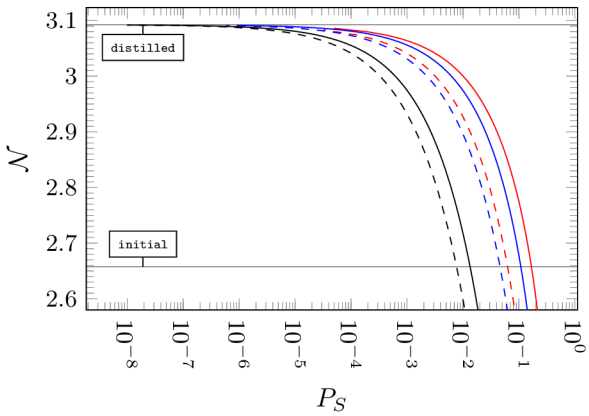

Figure 1.6. Gaussian logarithmic negativity $\mathcal{N}$ in respect to success probability for distillation of entanglement from two mode uniformly squeezed vacuum state with 8dB of generalised squeezing. The behaviour is investigated for ideal (solid curves) and realistic detectors (dashed curves) with quantum efficiency $\eta = 0.8$. Our procedure shows a significant improvement in terms of probability for as little as 10 allowed steps (blue). The attainable probability is roughly greater by an order of magnitude in comparison with the original procedure (black). Going to 75 steps (red) improves the probability even further, but the improvement rate steeply declines at that point.

states [155], its application on the subtracted state is justified by our ultimate interest in the properties of its Gaussian approximation. The measure can be calculated from the covariance matrix σ of the state as

$$\mathcal{N} = \max\left\{0, -\log_2\sqrt{2\left(\Delta - \sqrt{\Delta^2 - 4\det\sigma}\right)}\right\}$$
$$\text{where} \quad \Delta = \det\alpha + \det\beta - 2\det\gamma \quad \text{and} \quad \sigma = \begin{pmatrix} \alpha & \gamma \\ \gamma^\intercal & \beta \end{pmatrix}. \tag{1.17}$$

The dependence of the logarithmic negativity on the probability of success and the number N of allowed steps is presented in Figure 1.6 for the symmetric scenario in which both modes of the entangled state were subjected to loop-based subtraction with the identical number N of allowed steps. The maximally achievable distilled Gaussian logarithmic negativity is preserved and the loop-based procedure reaches higher probabilities of success compared to the original technique. The probability of successful operation in regimes achieving non-maximal logarithmic negativity improves roughly by an order of magnitude just by taking $N = 10$ steps in the subtraction process. Increasing the number of steps offers additional increase in success rate, however, the capacity for improvement quickly saturates. The qualitative improvement in success rate is preserved even for realistic detectors with limited quantum efficiency.

C Conclusions

The proposed loop-based single photon subtraction procedure achieved higher probability of success while retaining and even improving on the quality of the operation. We analyzed its performance in several distinct applications, namely in preparation of a squeezed single photon state by subtracting a single photon from a squeezed vacuum state of light, transition between different parties of coherent Schrödinger states facilitated by photon subtraction and finally, in an entanglement distillation from a two mode squeezed vacuum state.

In all the cases, the procedure with ideal detectors allowed obtaining the quality of the stan-

dard simple single photon subtraction procedure while significantly increasing the success probability, often up to its theoretical maximum. For the realistic detectors with limited unit quantum efficiency, the maximal probabilities could no longer be reached, but the improvement was still clearly visible. In both cases the improvements were significant already for ten steps of the loop-based procedure.

Chapter 2

Preparing Approximate Cubic States

This chapter focuses on the physics presented within the article *"Taming numerical errors in simulations of continuous variable non-Gaussian state preparation"* [156].

Quantum information theory exploits fundamental features of quantum physics to design protocols and algorithms that offer significant improvements over their classical counterparts [4, 25, 48, 157]. There are several candidate physical systems suitable for these applications, each with distinct advantages. Continuous variable quantum information processing with light offers feasible and fast generation and manipulation of entangled Gaussian quantum states that are at the core of the information protocols [64, 66–68, 72, 82, 158–160]. However, truly universal quantum information processing also requires elements of quantum non-Gaussianity [19, 50, 161–163]. Protocols based on Gaussian states and Gaussian operations are not universal [19] and can be efficiently simulated on a classical device [126].

For continuous variables of light, the non-Gaussianity is commonly introduced by photon number counting detectors, either the most basic on-off detectors capable of discerning presence of light [164], or the more advanced detectors truly distinguishing the photon numbers [165–174]. Such detectors can be employed for direct conditional implementation of non-Gaussian operations [87, 90, 92, 93, 107, 112, 151, 175], or for conditional preparation of non-Gaussian quantum states [88, 96–99, 108, 176–183]. The latter can be then used as a resource in deterministic implementation of non-Gaussian gates [50, 89, 90]. One thing these approaches have in common is the inherent probabilistic nature of measurement that results in several trade-offs between quality of the implemented operation or the prepared quantum state, the rate with which the desired operation succeeds, and the experimental challenges of the photon number resolving detector [171–174, 184]. For any given set of realistic detectors and any desired task we then need the ability to faithfully simulate the optical circuit to find out the required parameters leading to the optimal performance, or to find out whether the task is even feasible.

However, numerical simulation of simple quantum optical circuits, even though it is often employed in continuous variable quantum information processing [100, 185–188], is not a straightforward task. It is burdened by various difficulties, including discretization errors in numerical models relying on continuous representation, truncation errors in discrete models [185], the omnipresent rounding errors due to finite precision of arithmetics [189–193] and numerical truncation errors occurring in finite approximations of infinite processes [191, 193]. If not prevented by rigorous analysis, these numerical artifacts can dominate the computed values and lead to rapid divergence from correct results.

In this chapter we fully simulate an optical circuit suitable for preparation of non-Gaussian resource states for the cubic phase gate [89]. The goal is to find the optimal trade-offs between

the quality of the states and the probability of success for a range of available photon counting detectors [165, 171–174, 184, 194].

Numerical errors arising in simulations of optical circuits on classical computers and some of the methods we devised to analyse and overcome their influence are thoroughly discussed in the following Chapter 3: The Perils of Numerical Simulation.

This chapter is structured as follows. In the first section we introduce the necessary methodology, including cubic phase gates and the concept of non-linear quadrature, an assortment of photonic state preparation circuits, the actual variant of the circuit used to obtain the results, and the essentials of its numerical simulation. We discuss the results in the second section of this chapter and summarize the findings in the final, third section.

A Methodology

The necessary physical concepts and tools used to analyse the results are covered in this section. These include the essentials of non-linear variance of approximate cubic states, a special class of circuits used in quantum state synthesis, the particular circuit used in the paper, and finally, a brief explanation of its numerical simulation. The finer details of possible issues occurring in numerical simulations are discussed separately in Chapter 3: The Perils of Numerical Simulation.

Cubic interaction, cubic states and non-linear variance

The origins of the quest for realizable cubic phase gates $\exp(\imath\kappa\hat{X}^3)$ reach as far back as to the definition of universal continuous variable quantum computing [19] and the inception of fault tolerant computing realized with embedding of logical qubits into continuous variable quantum systems [50]. The action of the cubic phase gate on the canonical quadrature operators, $\hat{x}$ and $\hat{p}$, is best expressed in the Heisenberg picture

$$\begin{aligned} \hat{x} &\mapsto \hat{x} \,, \\ \hat{p} &\mapsto \hat{p} + 3\kappa\hat{x}^2 \,. \end{aligned} \tag{2.1}$$

One of the early proposed experimental implementations of the gate relied on quantum non-demolition (QND) interaction with a special ancillary cubic phase state

$$|\kappa\rangle = \int_{-\infty}^{\infty} \exp(\imath\kappa x^3)\, |x\rangle \, \mathrm{d}x \tag{2.2}$$

with the signal mode, followed by homodyne measurement on the ancillary mode and a subsequent unitary correction performed on the signal mode [50]. The cubic phase state is is not normalizable, in fact, it is not physical at all. It is, however, possible to synthesize a physical approximation of the cubic state in the limit of weak cubic interaction [87, 88], either using displacements and photon subtractions from a squeezed vacuum state [93] as proposed in [87] or by manipulating a TMSV state and projecting it onto the target as was done experimentally in [88]. Measuring the quality of the approximate states beyond the weak limit is challenging; the computation of fidelity with an unnormalizable state such as (2.2) is problematic to say the least.

The actual demonstration of the cubic phase gate [89] introduced a novel approach towards its measurement-induced implementation. Instead of employing a QND interaction, which would be also implemented in the measurement-induced fashion [195], the cubic phase gate is realized with the aid of two ancillary states. One of the ancillary states is a strongly squeezed state, while the other one approximates a cubic phase state. A pair of homodyne detectors and a classical non-linear feed-forward are used to control a Gaussian correction of the signal, thus realizing

the cubic phase gate. While the quadrature operators are transformed similarly to (2.1), there is one important difference,

$$\begin{aligned} \hat{x} &\mapsto \hat{x} \ , \\ \hat{p} &\mapsto \hat{p} + 3\kappa\hat{x}^2 + (\hat{p}_A - 3\kappa\hat{x}_A^2) \ . \end{aligned} \tag{2.3}$$

The additional term $\hat{p}_A - 3\kappa\hat{x}_A^2$ in the transformed momentum quadrature, called the non-linear quadrature in the literature [89, 90, 196, 197], represents the excess noise stemming from the approximate ancillary cubic phase state. The expectation value and the variance of the non-linear quadrature vanishes for the ideal cubic phase state (2.2), an eigenstate of the operator. The non-linear quadrature can be advantageously utilized to measure the quality of approximate cubic states.

The essential goal is to find quantum states minimizing its expectation value and variance. To rule out potential influence of Gaussian operations, the non-linear operator can be transformed into

$$\hat{q} = \mu\hat{p} - z\frac{\hat{x}^2}{\mu^2} \tag{2.4}$$

where the parameter μ represents Gaussian squeezing. It is practical to set $z = \frac{1}{\sqrt{2}}$ [197]. The variance of the non-linear quadrature $\hat{q}$ with respect to some state $\hat{\varrho}$ can be obtained as

$$V(\hat{\varrho}) = \langle(\hat{q} - \langle\hat{q}\rangle_{\hat{\varrho}})^2\rangle_{\hat{\varrho}} \ . \tag{2.5}$$

The measure of the quality of the quantum state $\hat{\varrho}$ can be defined with

$$\zeta(\hat{\varrho}) \coloneqq \frac{\min_\mu V(\hat{\varrho})}{\min_{\hat{\varrho}_G}\min_\mu V(\hat{\varrho}_G)} \equiv \frac{4}{3}\min_\mu V(\hat{\varrho}) \tag{2.6}$$

where the effects of the Gaussian squeezing are eliminated by the minimization [89, 197]. The variance is normalized against the least variance $\min_\mu V(\hat{\varrho}_G)$ achievable by Gaussian states $\hat{\varrho}_G$ [197].

Quantum state synthesis through measurement

Quantum states of light can be synthesized in a number of ways, the more prominent include alternating displacements and single photon additions to a vacuum state [92], alternating displacements and single photon subtractions from a squeezed vacuum state [93], exploiting Gaussian boson sampling [99], and using entangled states, combined with suitable unitary evolution and followed up by photon number measurement [50, 176]. The latter approach has proven to be experimentally viable in various applications, such as the construction of quantum non-Gaussian states [88, 97, 98, 178, 198], including the highly valued approximate cubic states.

At the very heart of the method, schematically outlined in Figure 2.1 (a), lies the source of perfectly correlated quantum states, such as the elusive

$$|\Psi\rangle = \frac{1}{\sqrt{d}}\sum_{k=0}^{d-1}|k\rangle\otimes|k\rangle \ , \tag{2.7}$$

where d gives the maximal dimension. This state is perfectly correlated in photon numbers. The unitary evolution of the state, given by the unitary operator $\hat{U}$ acting only on one of the modes, followed up by the detection of n photons, produces the state

$$\begin{aligned} |\varphi\rangle &= \sum_{k=0}^{d-1}\langle n|\hat{U}|k\rangle\,|k\rangle \\ &= \hat{U}^\intercal\,|n\rangle \end{aligned} \tag{2.8}$$

with the probability of success P inversely proportional to the dimension. The **infinite** dimension of CV quantum systems poses a practical problem — the entangled state $|\Psi\rangle$ is not physical. The

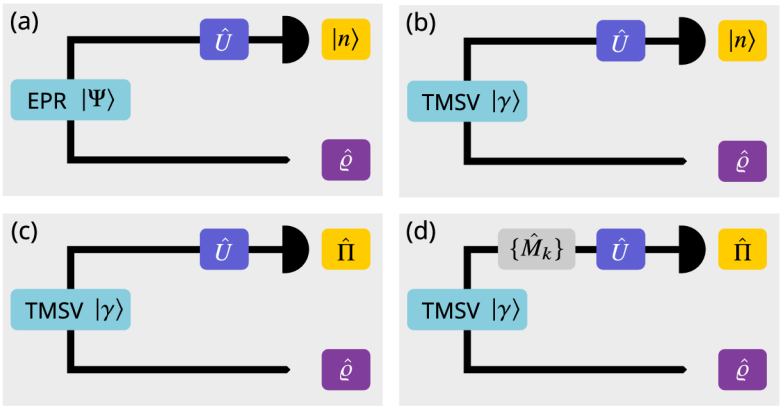

Figure 2.1. Methods of conditional quantum state preparation based on suitable unitary evolution of an entangled state, followed by a photon number measurement. **(a)** The essence of the method, utilizing a perfect, but unphysical, entangled state $|\Psi\rangle$. **(b)** A physical TMSV state $|\gamma\rangle$ is used instead. **(c)** Allowing for non-projective measurements, permitting the use of APD cascades for example, the detection outcomes are characterized by their respective POVM elements $\hat{\Pi}$. **(d)** Including imperfections (loss) in the model of the circuit described with a set of Kraus operators $\{\hat{M}_k\}$.

physically feasible version of the method, depicted in Figure 2.1 (b), instead relies on its physical version, the two mode squeezed vacuum (TMSV). This state is Gaussian and perfectly correlated in photon numbers, however, its coefficients in the expansion are no longer equal, but rather

$$|\gamma\rangle = \sqrt{1-\lambda^2}\sum_{k=0}^{\infty}\lambda^k\,|k\rangle\,|k\rangle \quad \text{with} \quad \lambda = \tanh(\gamma)\,, \tag{2.9}$$

where γ determines its squeezing rate. The resulting state is given by

$$\begin{aligned}|\varphi\rangle &= \sum_{k=0}^{\infty}\lambda^k\,\langle n|\hat{U}|k\rangle\,|k\rangle \\ &= \lambda^{\hat{n}}\hat{U}^{\intercal}\,|n\rangle \quad \text{where} \quad \hat{n} \coloneqq \hat{a}^{\dagger}\hat{a}\end{aligned} \tag{2.10}$$

with the probability of success $P = (1-\lambda^2)\lambda^{2n}$ of detecting $|n\rangle$. The operator $\hat{a}$ denotes the annihilation operator respective to the first mode and $\hat{n} \coloneqq \hat{a}^{\dagger}\hat{a}$ defines the photon number operator.

The detection process does not have to be limited to projective measurements; the inclusion of generalized measurements represented with POVM elements $\hat{\Pi}$ is laid out in Figure 2.1 (c). Because of the non-projective measurement, the resulting states may be mixed. The circuit can no longer be described in terms of pure states. Instead, the prepared state is given by the density operator

$$\hat{\varrho} = P^{-1}\,\mathrm{tr}_1\left[\hat{U}\hat{\varrho}_{\gamma}\hat{U}^{\dagger}\hat{\Pi}\right] \qquad \text{where} \quad \hat{\varrho}_{\gamma} = |\gamma\rangle\langle\gamma| \tag{2.11}$$

with the probability of successful measurement of the outcome $\hat{\Pi}$ given by the full trace

$$P = \mathrm{tr}\left[\hat{U}\hat{\varrho}_{\gamma}\hat{U}^{\dagger}\hat{\Pi}\right]\,. \tag{2.12}$$

The preparation circuit can be further generalized to include experimental imperfections, as in Figure 2.1 (d). These can be described with quantum channels and their effects expressed in terms of suitable Kraus operators $\{\hat{M}_k\}$. The resulting marginal state $\hat{\varrho}$, obtained upon mea-

suring the outcome associated with the POVM element $\hat{\Pi}$, is given by the density matrix

$$\hat{\varrho} = P^{-1}\,\mathrm{tr}_1\left[\hat{U}\Big(\sum_k \hat{M}_k\hat{\varrho}_\gamma\hat{M}_k^\dagger\Big)\hat{U}^\dagger\hat{\Pi}\right]$$

with the probability of success (2.13)

$$P = \mathrm{tr}\left[\hat{U}\Big(\sum_k \hat{M}_k\hat{\varrho}_\gamma\hat{M}_k^\dagger\Big)\hat{U}^\dagger\hat{\Pi}\right].$$

The exact forms of the Kraus operators $\hat{M}_k$ and the POVM elements $\hat{\Pi}$ are discussed in the following sections with detailed analysis of the state preparation circuit.

The circuit capable of producing approximate cubic states

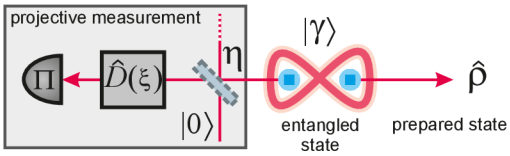

Figure 2.2. Conditional quantum state preparation scheme based on a TMSV state $|\gamma\rangle$. One of its modes is displaced with $\hat{D}(\xi)$ and measured, using either APD, PNRD or an APD cascade. The detection outcome is characterized by the POVM element $\hat{\Pi}$. Overall losses and inefficiencies are modeled using a beam splitter with intensity transmittance η.

The variation of the state preparation circuit, illustrated in Figure 2.2, was used to prepare approximate cubic states. It is based on the generalized circuit Figure 2.1 (d). The unitary evolution $\hat{U}$ is realized as a coherent displacement [199] given by the unitary operator

$$D(\xi) \coloneqq \exp\left[\xi\hat{a}^\dagger - \xi^*\hat{a}\right], \tag{2.14}$$

where $\xi \in \mathbb{C}$ represents the complex amplitude of the displacement operation. The subsequent photon number measurement is carried out either using an ideal photon number resolving detector (PNRD), or its approximation based on a cascade of avalanche photodiode (APD) detectors [184, 194]. The circuit accounts for basic imperfections of the experimental realization. Detection inefficiencies and propagation losses in the first mode are modeled using a beam splitter with intensity transmittance η. Its action on the affected mode can be represented in terms of Kraus operators [122] with

$$\hat{\varrho} \longmapsto \sum_{k=0}^{\infty}\hat{M}_k\hat{\varrho}\hat{M}_k^\dagger \quad \text{where} \quad \hat{M}_k = \frac{1}{\sqrt{i!}}(\sqrt{1-\eta})^i(\sqrt{\eta})^{\hat{n}}\hat{a}^k \tag{2.15}$$

where $\hat{a}$ denotes the annihilation operator respective to the affected mode. The parameter η characterizes the overall efficiency of the circuit; on the other hand, its converse, $1-\eta$, characterizes the overall propagation losses and detector inefficiencies. Following the general expression (2.13), this circuit produces quantum states with density matrix

$$\hat{\varrho} = P^{-1}\,\mathrm{tr}_1\left[\hat{D}(\xi)\Big(\sum_k \hat{M}_k\hat{\varrho}_\gamma\hat{M}_k^\dagger\Big)\hat{D}^\dagger(\xi)\hat{\Pi}\right]$$

with the probability of success (2.16)

$$P = \mathrm{tr}\left[\hat{D}(\xi)\Big(\sum_k \hat{M}_k\hat{\varrho}_\gamma\hat{M}_k^\dagger\Big)\hat{D}^\dagger(\xi)\hat{\Pi}\right]$$

conditioned on the detection outcome associated with the POVM element $\hat{\Pi}$. From the experimental perspective the parameters γ and ξ can be fine tuned to engineer a desired state $\hat{\varrho}$ with optimal performance given particular experimental configuration characterized by the overall efficiency η and conditioning on the detection outcome associated with the POVM element $\hat{\Pi}$ of the detector.

Simulating the circuit on a classical computer

The CV nature of the preparation scheme introduced in Figure 2.2, described with the relations (2.16), makes its exact numerical simulation not only impractical, but outright impossible. It is possible to perform approximate numerical simulation of the formulae on a truncated Fock space (TFS). The dimension d_0 of the TFS should be large enough to support all the quantum states occurring in the simulation and optimally as low as possible to minimize the computational complexity of the simulation.

The circuit begins with the TMSV state. One of its modes is attenuated by the loss channel (2.15). This only reduces its energy and, as a consequence, the required support shrinks in size. The attenuating channel can be therefore safely disregarded in the estimation of the necessary dimension. A similar argument can be made about the detection process; the detectors in question target subspaces with dimensions lower than d_0. Consequently, the operator $\hat{\Pi}$ does not impact the dimension and can be removed from the search. Finally, the displacement operation can only increase the size of the support required to accurately represent the TMSV state. With all those simplifications, the search reduces into finding the least dimension d_0 such that the displaced TMSV state is faithfully approximated on the d_0 dimensional TFS for **all the possible** values of γ and ξ used in the simulation. By taking the largest displacement $\xi_\star$ and squeezing rate $\gamma_\star$ considered in the analysis, it is possible to iteratively determine d_0 as the lowest positive integer such that the cutoff error

$$1 - (1 - \lambda_\star^2) \sum_{i=0}^{d_0-1} \lambda_\star^{2i} \sum_{j=0}^{d_0-1} \left| \langle i | \hat{D}(\xi_\star) | j \rangle \right|^2 \leq \epsilon_0 \tag{2.17}$$

falls below some reasonable threshold ϵ_0. In effect the total probability associated with contributions of order higher than d_0 is bound by ϵ_0. The coefficients of the TMSV state are powers of $|\lambda| < 1$ and consequently trivial to compute. The matrix elements of the displacement operator are more challenging to obtain; while an analytical formula exists [199],

$$\langle m | \hat{D}(\xi) | n \rangle = \sqrt{\frac{n!}{m!}} \xi^{m-n} \exp\left(-\frac{1}{2}|\xi|^2\right) L_n^{(m-n)}(|\xi|^2) \quad \text{for} \quad m \geq n \tag{2.18}$$

with $L_\beta^\alpha(x)$ denoting the associated Laguerre polynomial function [200], its direct evaluation can easily lead to numerical overflows and otherwise numerically inaccurate results in general. Alternative means of its computation are discussed within sections 3.B and 3.C. In particular, the TAME method (3.22) was used instead of the closed form formula.

We considered $0 \leq \gamma \leq 1$, corresponding to roughly 8.7dB squeezing, and $0 \leq \xi \leq 1$ in the numerical simulation. We found the optimal $d_0 = 70$ of the base TFS by using $\gamma_\star \equiv \xi_\star \equiv 1$ in (2.17) and setting the threshold $\epsilon_0 \equiv 10^{-13}$. The associated dimension d_1, required in the numerical computations and discussed in section 3.C, was determined with the help of the Algorithm 3.1 as $d_1 = 90$. The relations (2.16) describing the state preparation circuit were approximated with finite dimensional objects from the d_0-dimensional TFS.

The analysis of the cubic state preparation was approached with a rudimentary grid-based exploratory strategy. We divided the $[0 \leq \gamma \leq 1] \otimes [0 \leq \xi \leq 1]$ region of tunable parameters into an equidistant 1001×1001 grid of points $u_j \coloneqq (\gamma_j, \xi_j)$ and numerically evaluated the approximated relations (2.16) for each point u_j and each experimental scenario $v_j \coloneqq (\eta_j, \Pi_j)$ with distinct overall efficiency of the circuit η and every POVM element $\hat{\Pi}$ under our consideration. Those included the positive detection outcome $\mathbb{1} - |0\rangle\langle 0|$ of a single APD, the detection of three photons $|3\rangle\langle 3|$ with a PNRD, and the outcomes of APD cascades associated with the detection of three photons, $\hat{\Pi}_3^4$, $\hat{\Pi}_3^5$ and $\hat{\Pi}_3^{10}$, defined with

$$\hat{\Pi}_n^m \coloneqq \sum_{k=0}^{d_0-1} w(k,n,m)\, |k\rangle\langle k|$$
$$\text{where} \quad w(k,n,m) \coloneqq \begin{cases} m^{-k} \binom{m}{n} \sum_{l=0}^{n} \binom{n}{l} (-1)^l (n-l)^k i & \text{when} \quad k \geq n \\ 0 & \text{otherwise .} \end{cases} \tag{2.19}$$

The $\hat{\Pi}_n^m$ elements represent detection outcomes where exactly n detectors click within APD cascade comprising m detectors [184, 194].

This way we procured an assortment of probabilities $P(i,j)$ and density matrices $\varrho(i,j)$ corresponding to the sequences u_i and v_j of points. We then computed the individual moments required in the calculation of the measure (2.6) directly from elements of the density matrices $\varrho(i,j)$. We avoided the matrix representation of the operators involved in the moment computation to avert unnecessary truncation errors. The minimization with respect to the Gaussian squeezing rate μ within the measure $\zeta(\hat{\varrho})$ was solved analytically. We thus obtained $\zeta(i,j)$ values for their respective $\varrho(i,j)$ matrices and $P(i,j)$ probabilities. We then divided the dataset corresponding to each experimental scenario v_j into bins based on values of the measure $\zeta(i,j)$ and found the maximal attainable probability $P(i,j)$ within each bin. The results are discussed in the next section.

B Discussion and results

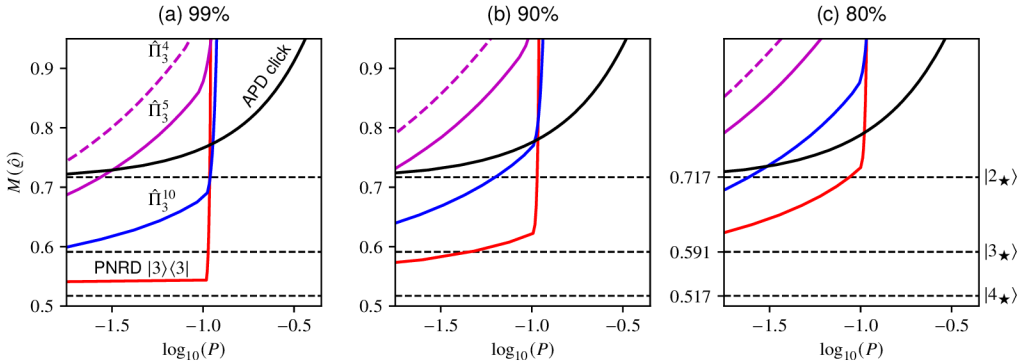

Figure 2.3. A comparison of attainable variance $M(\hat{\varrho})$ as a function of success probability. The variance is normalized with respect to the minimal variance achievable by Gaussian states. We use the same vertical and horizontal axes in the plots to show the contrast between the almost ideal (a) and lossy (b, c) scenarios with 99%, 90% and 80% transmission efficiencies. Horizontal dashed lines are used to mark the optimal cubic state approximations $|n_\star\rangle \in \mathcal{H}_n$ constructed on low-dimensional TFS. We encode the information about the POVM elements as follows: APD click with solid black line, PNRD projection onto $|3\rangle$ with solid red, APD cascades comprising four ($\hat{\Pi}_3^4$, dashed magenta), five ($\hat{\Pi}_3^5$, magenta) and ten ($\hat{\Pi}_3^{10}$, blue) detectors where three detectors click. Overall, utilizing the PNRD $|3\rangle$ (solid red) produces states with lowest non-linear variance, therefore producing comparatively better approximations of the cubic state. In both (b) and (c) a single APD outperforms the APD cascades comprising five and four detectors for probabilities greater than 1%. In this regime the cascade comprising ten detectors still offers advantage over single APD. In (c) a single APD outperforms APD cascades comprising either four, five or ten detectors for success probabilities larger than roughly 5%.

A comparison of the attainable non-linear variance $\zeta(\hat{\varrho})$ as a function of success probability P is presented in Figure 2.3. Different detection outcomes are examined, in particular a single APD detecting any number of photons (black line), the measurement of three photons with a PNRD (red line) and the its approximations realized through an APD cascade [184] where three APD detectors out of four (dashed magenta), five (magenta) and ten (blue) click. The plots show (a) 99%, (b) 90%, and (c) 80% overall efficiency η. The optimal cubic state approximations [89] $|n_\star\rangle \in \mathcal{H}_n$ constructed on n dimensional TFS are marked with dashed horizontal lines. These states were found by searching for pure states spanning the first n Fock states that would minimize the variance $\zeta(\hat{\varrho})$ of the non-linear quadrature [89]. Their inclusion makes it possible for qualitative comparison with the states produced by our scheme.

Using PNRD yields the best results in general. In the idealized scenario with 99% efficiency the PNRD projecting onto $|3\rangle$ approaches the variance of the optimal $\mathcal{H}_4$ non-linearly squeezed state $|4_\star\rangle$. It also attains the best values consistently across the considered transmission efficiencies, therefore producing comparatively better approximations of the cubic state than either the APD cascades or a single APD. In both the 90% and 99% regimes, the APD cascade comprising ten detectors promises better performance than a single APD or any other cascade configuration for that matter. In the low-efficiency mode (80%) we can see that a single APD outperforms APD cascades for probabilities of success greater than 5%. This can be attributed to the imperfections inherent to APD cascades [184]. Their flaws become emphasized with increased loss, rendering a single APD to be the better choice.

Unless a PNRD capable of distinguishing at least three photons is available, it is advantageous to use a single APD in any practical scenario with non-ideal transmission efficiency as long as success probabilities larger than approximately 5% are desired. The advantage of a single APD can be offset by using an exorbitant number of detectors within APD cascade.

In a more realistic analysis of the preparation circuit it would be straightforward to include the propagation losses affecting the mode carrying the resulting state. This form of decoherence can be accounted for by modifying the squeezing strength of the non-linearly squeezed state [197]. Consequently we did not consider this additional attenuation since it does not influence the fundamental properties of these non-Gaussian states.

C Conclusions

We analyzed the non-Gaussian state preparation scheme based on suitable manipulation of a two mode squeezed vacuum with subsequent photon counting measurement [50, 88, 97, 198] in the context of engineering non-linearly squeezed cubic states [50, 89, 176] for measurement induced cubic gates [50, 89, 90]. We have compared the effects of different detection mechanisms, including APD, PNRD and its approximations using APD cascades [184, 194] with varying number of APD detectors, to determine practical approach towards state preparation. In our analysis we have optimized the free parameters of the preparation scheme, the initial squeezing and the displacement, to attain optimal results.

This analysis can be also used to quantify the quality of APD cascades. We found that in practical applications when PNRD is not available, using a single APD to engineer non-linearly squeezed states offers better performance compared to employing APD cascades comprising small numbers of detectors. We attribute this counter-intuitive result to the imperfections inherent to APD cascades [184] which are exaggerated with increased loss; these flaws became significant for 20% overall loss. The primary cause of this behaviour lies within the employed avalanche detectors as a single click may be triggered by multiple photons. This is a critical issue when engineering multi-photon states.

Our circuit can be extended to utilize multiple displacements and detectors. Furthermore, the method could be employed in preparation of a wider variety of quantum states with practical applications, such as GKP states [50]. Similarly the proposed method for numerical construction of truncated unitary operators (see Chapter 3: The Perils of Numerical Simulation for details) is not limited to displacement only can be applied to, for example, squeezing or cubic phase-shift operators.

Chapter 3

The Perils of Numerical Simulation

This chapter remarks on the finer points of numerical computation and outlines the numerical aspects of the article *"Taming numerical errors in simulations of continuous variable non-Gaussian state preparation"* [156].

Classical digital computers [20] encode information into finite sequences of bits and it is therefore impossible to represent arbitrary real numbers. The standard approach [190–193, 201] is to approximate real numbers with **floating point** numbers. Real numbers are then rounded to their closest representable floating point neighbors. This generally introduces **rounding errors**. To make matters worse, floating point arithmetic with floating point numbers does not necessarily produce exactly representable floating point numbers. Results of floating point arithmetic must be rounded, possibly introducing additional rounding errors [190–193, 201]. Consequently complex sequences of arithmetic operations possess the potential to accumulate and even amplify rounding errors. Even the most straightforward tasks such as adding up a sequence of floating point numbers can produce widely different results with varying degrees of accuracy based on the algorithm of choice [190–192]. Rounding error analysis is therefore a crucial part of algorithm design [189–192] and commonly used numerical algorithms are frequently accompanied by rigorous rounding error analysis. Nevertheless numerical simulation cannot be considered completely accurate as the error analysis only establishes upper bounds on the numerical errors [189, 191–193].

The practical concerns, when dealing with numerical simulation, are therefore always related to extent of the errors, rather than to their presence. This is a familiar concept in physics, a discipline which is well acquainted with limited precision of measured quantities [202, 203]. Numerical simulation of continuous variable (CV) systems suffers from further issues related to the fundamental representation of quantum states and quantum operations. CV states reside in infinite-dimensional Hilbert spaces and can be, in principle, described in two distinct ways. The first description employs continuous functions, either wave functions given in position or momentum representation, or quasi-probability distributions [82, 158, 159] which combine the two quadratures. The practical issue with this approach is the continuous nature and generally infinite support of these functions. In numerical simulations using classical digital computers their support must be limited to finite intervals and both their domains and ranges discretized during numerical integration [192, 193], introducing additional numerical errors.

It is alternatively possible to take the advantage of the discrete Fock basis spanned by eigenstates of the number operator. This basis is still infinite but, unlike in the case of basis spanned by eigenstates of continuous operators, the number of its elements is countable. Even though exact representation of CV states in Fock basis remains impossible, we can truncate the basis to a finite number of elements and approximate the original Hilbert space with this truncated, finite-dimensional, restriction. It is possible to avoid various discretization errors at the cost of introducing truncation errors instead. Consequently, numerical simulations utilizing vector spaces

spanned by the truncated Fock basis are often employed in detailed analysis of CV quantum circuits.

A Truncated Fock spaces

Let $\mathcal{H}_\infty$ denote the original Hilbert space and let $S_\infty \coloneqq \{|j\rangle \in \mathcal{H}_\infty \| \ j = 0, 1, \dots\}$ be the original infinite dimensional Fock basis. Its elements, the individual Fock states $|j\rangle \in S_\infty$, are orthonormal. Their vector components, expressed in the Fock basis, satisfy $[|j\rangle]_i^{S_\infty} \coloneqq \langle i|j\rangle \equiv \delta_{ij}$.

The **truncated Fock basis** S_F can be formed by taking the first F elements of the Fock basis,

$$\{|0\rangle, \dots, |F-1\rangle\} \subset S_\infty \tag{3.1}$$

and truncating their vector forms, expressed in the Fock basis, to the first F components. This makes

$$S_F = \{|0\rangle^{(F)}, \dots, |F-1\rangle^{(F-1)}\} \tag{3.2}$$

where the upper right indices in $|j\rangle^{(F)}$ denote dimensions of said vectors. The elements of the basis are also orthonormal; their vector components satisfy

$$[|j\rangle^{(F)}]_i^{S_F} \coloneqq {}^{(F)}\langle j|i\rangle^{(F)} \equiv [|j\rangle]_i^{S_\infty} \equiv \delta_{ij} \quad \forall i = 0, 1, \dots, F-1 \ . \tag{3.3}$$

The linear hull of S_F forms the F-dimensional **truncated Fock space** (TFS) $\mathcal{H}_F$.

The definition of the TFS itself, along with the transition between the original and the truncated Fock basis, is sufficient to formalize the transition of vectors from $\mathcal{H}_\infty$ into $\mathcal{H}_F$ and linear operators from $\mathcal{L}(\mathcal{H}_\infty)$ to $\mathcal{L}(\mathcal{H}_F)$. Let $|\psi\rangle \in \mathcal{H}_\infty$ be an arbitrary state expressed in the Fock basis as

$$|\psi\rangle = \sum_{i=0}^{\infty} c_\psi(i) \, |i\rangle \tag{3.4}$$

where $|i\rangle \in S_\infty$ with coefficients $c_\psi(i) = [|\psi\rangle]_i^S \coloneqq \langle i|\psi\rangle \in \mathbb{C}$. The expression

$$\underset{F}{\text{trunc}}\{|\psi\rangle\} \coloneqq \sum_{i=0}^{F-1} c_\psi(i) \, |i\rangle^{(F)} \tag{3.5}$$

where $|i\rangle^{(F)} \in S_F$ then defines its truncated variant from $\mathcal{H}_F$. Similarly, let $\hat{G} \in \mathcal{L}(\mathcal{H}_\infty)$ be a linear operator on $\mathcal{H}_\infty$ expressed as

$$\hat{G} = \sum_{i=0}^{\infty} \sum_{j=0}^{\infty} g(i,j) \, |i\rangle\langle j| \tag{3.6}$$

where $|i\rangle \in S_\infty$ with matrix elements $g(i,j) = [\hat{G}]_{ij}^S \coloneqq \langle i|\hat{G}|j\rangle \in \mathbb{C}$. Then the expression

$$\underset{F}{\text{trunc}}\{\hat{G}\} \coloneqq \sum_{i=0}^{F-1} \sum_{j=0}^{F-1} g(i,j) \, |i\rangle^{(F)}\langle j| \tag{3.7}$$

where $|i\rangle^{(F)} \in S_F$ defines its truncated analogue on $\mathcal{L}(\mathcal{H}_F)$. A natural extension of this approach allows for transitions from higher-dimensional truncated spaces to lower-dimensional truncated spaces.

Navigating truncated Fock spaces

In this description, pure quantum states become complex F dimensional vectors of numbers, linear operators turn into complex $F \times F$ matrices and the operations reduce to linear algebraic

expressions such as matrix multiplication, Kronecker products and matrix traces. There is, however, a hefty price to be paid for this simplification, manifesting in the form of truncation errors with several distinct effects on the simulation.

Firstly, it is impossible to represent general quantum states exactly. Take an arbitrary quantum state $|\zeta\rangle \in \mathcal{H}_\infty$ and its truncated variant $\mathrm{trunc}_F\{|\zeta\rangle\} \in \mathcal{H}_F$. The quality of the truncated state can be determined from its normalization, or rather the lack of it, using the cutoff error

$$\mathrm{cutofferror}_F\{|\zeta\rangle\} \coloneqq 1 - \sum_{i=0}^{F-1} |c_\zeta(i)|^2 \,, \tag{3.8}$$

where $c_\zeta(i) = [|\zeta\rangle]_i^S \equiv \langle i|\zeta\rangle$ are the vector components of the state $|\zeta\rangle$ in Fock representation. In essence the quality of the representation is loosely given by the support of the state relative to the dimension of the TFS. This is not the only conceivable metric, but it is a convenient one as it is straightforward to calculate.

Secondly, the algebraic structure of the space changes with the transition to finite dimension. As a result the usual commutation rules no longer apply since for any pair of operators $\hat{G}$ and $\hat{H}$ the relation

$$\underset{F}{\mathrm{trunc}}\{[\hat{G}, \hat{H}]\} = [\underset{F}{\mathrm{trunc}}\{\hat{G}\}, \underset{F}{\mathrm{trunc}}\{\hat{H}\}] \tag{3.9}$$

does **not necessarily hold** anymore. We can illustrate the change in algebraic structure on bosonic creation and annihilation operators, $\hat{a}^\dagger$ and $\hat{a}$. In the infinite-dimensional case we have $[\hat{a}, \hat{a}^\dagger] = \hat{\mathbb{1}}$, that is, the two operators commute to identity. With the truncated commutator the result remains the same $\mathrm{trunc}_F\{[\hat{a}, \hat{a}^\dagger]\} = \mathrm{trunc}_F\{\hat{\mathbb{1}}\} \equiv \mathbb{1}^{(F)}$, which is an identity matrix of the corresponding dimension F. Conversely the commutator of the truncated annihilation and creation operators differs from identity in the final element on the diagonal

$$[\mathrm{trunc}_F\{\hat{a}\}, \mathrm{trunc}_F\{\hat{a}^\dagger\}] = \mathbb{1}^{(F)} - F\,|F-1\rangle^{(F)}\langle F-1| \tag{3.10}$$

which can be understood as a truncation error due to the product of two truncated matrices.

Thirdly and finally, replacing infinite-dimensional operators in arguments of operator functions with their truncated versions may not be without consequences. Consider an operator function $f(\hat{Q})$. In principle

$$\underset{F}{\mathrm{trunc}}\{f(\hat{Q})\} \neq f(\underset{F}{\mathrm{trunc}}\{\hat{Q}\}) \tag{3.11}$$

for general operator arguments. This has grave consequences for numerical simulation of unitary evolution. It is customary to approximate the exponential operator, $\mathrm{trunc}_F\{\exp(\hat{Q})\}$, with the matrix exponential $\mathrm{expm}(\mathrm{trunc}_F\{\hat{Q}\})$ of the truncated operator argument [185]. However, this method **can not be relied upon** as

$$\underset{F}{\mathrm{trunc}}\{\exp(\hat{Q})\} \neq \mathrm{expm}(\underset{F}{\mathrm{trunc}}\{\hat{Q}\}) \,. \tag{3.12}$$

We must therefore seek alternative approaches: there are three primary techniques available for numerical simulation. The first one relies on the knowledge of a closed form formula for elements of the unitary operator. It has to be derived analytically and is not always attainable. The second method, proposed in the recent paper [185], is numerical and derives individual elements of unitaries by recurrent formulae. In the third approach the matrix exponential is simply computed with the truncated matrix argument as $\mathrm{expm}(\mathrm{trunc}_F\{\hat{Q}\})$ and the dimension of the computation space is chosen large enough so that the errors are irrelevant in the particular simulation.

Neither approach is perfect. Each suffers from specific numerical errors. This is a valid concern even for the first method which uses analytical forms: it is because mathematical expressions, especially those involving factorials, large powers of non-negligible numbers or relying on special functions, which are often defined using similar expressions or recurrent formulae, still need to be evaluated numerically with finite precision in floating point arithmetic, leading to introduction and eventual accumulation of rounding errors. The numerical errors cannot be straightforwardly calculated without a priori knowledge of the ideal operator or without thorough numerical analysis of rounding errors, an area of expertise that is mostly out of the scope of theoretical physics and therefore scarcely present in research reports.

In the following section we apply these methods of construction to the simplest experimentally testable example, coherent displacement, and use this particular case study to demonstrate the fundamental shortcomings of each approach.

B The curious case of coherent displacement

Coherent displacement is a fundamental Gaussian operation in quantum optics used in a broad range of quantum protocols for quantum state preparation, manipulation, and measurement [19, 50, 82, 158, 159, 199]. Coherent displacement is represented by the unitary operator

$$\hat{D}(\xi) \coloneqq \exp(\xi\hat{a}^\dagger - \xi^*\hat{a}) \tag{3.13}$$

where $\xi \in \mathbb{C}$ gives the displacement amplitude and $\hat{a}, \hat{a}^\dagger$ represent the annihilation and creation operators. It is one of the operations for which a closed form formula exists [199], given as

$$\langle m|\hat{D}(\xi)|n\rangle = \sqrt{\frac{n!}{m!}}\xi^{m-n}\exp\left(-\frac{1}{2}|\xi|^2\right)L_n^{(m-n)}(|\xi|^2)\,, \quad m \geq n \tag{3.14}$$

where $L_\beta^\alpha(x)$ denotes the associated Laguerre polynomial function [200]. This relation only covers the lower triangular matrix; the rest of the matrix can be easily recovered from (3.14) using

$$\langle m|\hat{D}(\xi)|n\rangle = (-1)^{m-n}\left(\langle n|\hat{D}(\xi)|m\rangle\right)^*\,, \quad m < n\,. \tag{3.15}$$

The formula (3.14) can be computed in multiple different ways with varying numerical accuracy impacted by the simplifications made in the expression and the order of their evaluation. When implemented exactly as it stands in (3.14), it is plagued by the limitations of FP arithmetic. Its first term underflows for comparatively large m, while the second term overflows for $|\xi| > 1$ and large enough difference $m - n$. When both the numerical underflow and the overflow coincide, the ill-defined expression $0 \times \infty$ is evaluated, resulting in error.

The limitations of the direct approach can be partially alleviated by replacing the fraction in the first term with

$$\frac{1}{n+1}\frac{1}{n+2}\cdots\frac{1}{m-1}\frac{1}{m}, \quad \text{or (almost) equally,} \quad \frac{1}{(n+1)(n+2)\cdots(m-1)m}\,. \tag{3.16}$$

Nevertheless, this substitution is not going to prevent the pathological $0 \times \infty$ as expressions with either sufficiently high difference $m - n$ will still occur. The substitution affects the numerical accuracy of (3.14) which also depends on the way the it is evaluated. Multiplying the individual fractions gives a different outcome than inverting the product as a whole.

One of the pathological occurrences of $0 \times \infty$ can be observed for $\langle m|\hat{D}(\xi)|0\rangle$ with $|\xi| > 1$. The denominator in the substitution (3.16) reduces into $m!$ and the factorial overflows for sufficiently large m. This threshold can be estimated with the aid of the improved error bounds [204] for Stirling's approximation

$$\sqrt{2\pi}\exp\left[\ln(m)\left(m+\frac{1}{2}\right) - m + \frac{1}{12m+1}\right] < m! < \sqrt{2\pi}\exp\left[\ln(m)\left(m+\frac{1}{2}\right) - m + \frac{1}{12m}\right]\,. \tag{3.17}$$

The upper bound can be exploited to determine the largest safe value of m for which the factorial $m!$ does not overflow by comparing the bound with the largest representable FP number within the particular FP system used in calculation of (3.14). Similarly the value of m for which $m!$ definitely overflows can be determined from the lower bound.

The overall qualitative behaviour of the formula (3.14) can be discerned from

$$\frac{|\xi|^m}{m!} \tag{3.18}$$

analyzed in the context of the standard double FP precision. This expression comprises the disputable components of the first two terms in the original formula and becomes **invalid** under the same circumstances. Four regions with qualitatively distinctive outcomes are identified

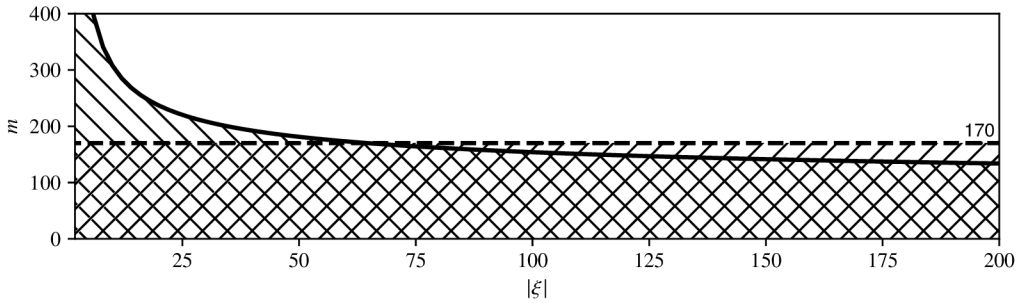

Figure 3.1. Demonstration of the qualitative behavior of (3.14) on a surrogate model (3.18) with numerical limits of the standard double precision floating point arithmetic. The solid curve shows maximal m such that $|\xi|^m$ does not overflow; the dashed line shows maximal m such that $m!$ does not overflow. These two divide $|\xi|$ and m parameters into four distinct regions. The pathological $0 \times \infty$ expression appears in the top unmarked region. In the slashed region on the right, the expression diverges to infinity. In the left back-slashed region, the expression incorrectly zeroes out due to overflow in $m!$. Neither region provides satisfactory values of (3.18) and consequently of the formula (3.14). Only the parameters from the bottom cross-stitched region lead to numerically valid, finite valued results.

within Figure 3.1 for different combinations of the $|\xi|$ and m parameters. The *dashed horizontal* line determines the maximal m for which $m!$ does not overflow and the *solid* curve marks the maximal possible m such that $|\xi|^m$ does not overflow. These lines divide the area into four regions. In the *top-left back-slashed* region $m!$ overflows, while $|\xi|^m$ remains finite. Even though (3.18) is numerically valid in this region, its value might be incorrect as it always zeroes out due to the overflown denominator. Similarly the formula remains a valid, albeit incorrect, expression in the *central-right slashed* region where $m!$ is a regular number, however, $|\xi|^m$ overflows and therefore (3.18) reaches numerical infinity. In the *top* (unmarked) region the pathological $0 \times \infty$ is obtained since both $|\xi|^m$ and $m!$ overflow at the same time.

Neither of the regions discussed so far provides a satisfactory result. The formula (3.18) can only attain suitable numerical values within the *cross-stitched* region. While no overflows happen within this region resulting value should still be treated with utmost care as it might still succumb to loss of accuracy due to rounding errors since large numbers are generally involved in the computation. In its essence this region only provides a necessary, rather than sufficient, condition for different combinations of the parameters $|\xi|$ and m.

The established range of viable parameters of the model (3.18) shows that, when utilizing double precision for the numerical simulation, the maximal attainable dimension is upper-bound by 170, regardless of the displacement modulus $|\xi|$. One of the implications is that (3.14) can not be used to construct the displacement matrix on arbitrarily large truncated Fock spaces.

Another possible workaround around the numerical limitations is to carefully employ a logarithmic-exponential substitution to the problematic terms. In particular, the expression

$$\exp\left\{-\frac{1}{2}|\xi|^2 - \frac{1}{2}\left[\log(n+1) + \log(n+2) + \cdots + \log(m)\right] + (m-n)\log(\xi)\right\} \tag{3.19}$$

makes it possible to access values of m, n and ξ outside of the regions discussed previously in Figure 3.1 as long as the argument of the exponential remains below the practical numerical limit of the exponential. The maximal value of the argument within the exponential is slightly below 710. In double precision a numerical overflow occurs for arguments larger than 709. A similar approach is currently employed in the state of art frameworks [186, 188, 205] targeting numerical simulations of quantum circuits.

The novel recurrent formulae [185] or the plain matrix exponential [206, 207] with a truncated argument can be utilized instead of the closed form formula (3.14). While it is not possible to ascertain their accuracy without a priori knowledge of the ideal operator, it can be easily de-

termined whether the generated matrices G are outright incorrect by checking the normalisation

$$\|G\,|j\rangle^{(F)}\|_2 \coloneqq \sqrt{\sum_{i=0}^{F-1}\left|[G]_{ij}^{S_F}\right|^2} \tag{3.20}$$

of displaced truncated Fock states $\{|0\rangle^{(F)},\ldots,|F-1\rangle^{(F)}\}$. It corresponds to the sum of squared absolute values of elements in the jth column of the truncated displacement matrix $G \coloneqq \mathrm{trunc}_F\{\hat{D}(\xi)\}$ or its approximation employing the matrix exponential $\mathrm{expm}(\mathrm{trunc}_F\{\hat{Q}\})$ with the argument

$$\underset{F}{\mathrm{trunc}}\{\hat{Q}\} \coloneqq \xi \underset{F}{\mathrm{trunc}}\{\hat{a}^\dagger\} - \xi^* \underset{F}{\mathrm{trunc}}\{\hat{a}\} \tag{3.21}$$

comprising the truncated creation and annihilation operators.

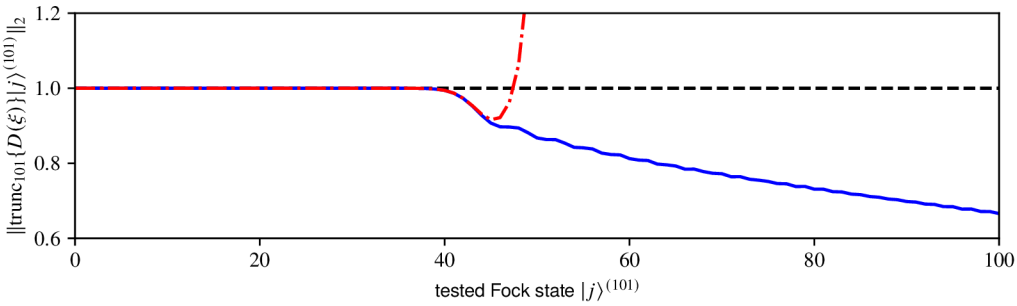

Figure 3.2. Normalisation (3.20) of individual displaced truncated Fock states $|j\rangle^{(101)}$ with $0 \le j \le 100$. The displacement operator $\mathrm{trunc}_{101}\{\hat{D}(3-2\imath)\}$ is constructed on 101 dimensional TFS using the closed form formula (blue solid), the recurrent formula (red dash-dotted), and approximated with the matrix exponential (black dashed line).

The normalisation (3.20) is demonstrated in Figure 3.2 for $\mathrm{trunc}_{101}\{\hat{D}(3-2\imath)\}$ constructed using the closed form formula (3.14), represented with a blue solid line, the recurrent formula [185] shown with a red dash-dotted line, and approximated with the matrix exponential (black dashed line). Double precision [191, 201] is utilized in the computation. The outright numerical issues plaguing the direct method (3.14) are avoided by keeping the working dimension sufficiently low. There are two regions of qualitatively distinct behaviour in the plot. The first region, spanning the first 40 Fock states, shows correct normalization for all three methods of construction. In the following region the normalisation dwindles for both the closed form and the recurrent formulae whilst the matrix exponential remains *incorrectly* normalized. It remains normalized only because the matrix exponential function, by definition, produces unitary matrices from anti-Hermitian arguments. Unitarity is not necessarily the desired outcome here since the goal is to obtain the correct $\mathrm{trunc}_{101}\{\mathrm{expm}(\hat{Q})\}$ matrix rather than the computed approximation $\mathrm{expm}(\mathrm{trunc}_{101}\{\hat{Q}\})$.

Let us explicitly discuss the issue at hand. The displacement operator (3.13) is unitary by definition. Columns of its matrix representation can be understood as coefficient vectors of displaced Fock states. In the infinite-dimensional case these states should be normalized, that is the vector 2–norm [208] of each column should satisfy $\|\hat{D}(\xi)\,|j\rangle\|_2 \equiv 1\;\forall\,|j\rangle \in S$. However, this will not generally hold in finite dimension where we can find a threshold state $|\tau\rangle^{(F)} \in S_F$ that, when displaced, will not be properly represented on the TFS. The states $j \ge \tau$ will suffer from non-negligible errors (3.8), making their normalization $\|\mathrm{trunc}_F\{\hat{D}(\xi)\}\,|j\rangle^{(F)}\|_2 < 1$.

The plot in Figure 3.2 reveals that when the matrix is constructed via (3.14), the higher states are correctly denormalized. Conversely the matrix exponential produces *incorrectly* normalized states. In this context such behavior can be considered a manifestation of truncation errors.

The normalisation of the recurrently computed matrix starts to rise exponentially somewhere around $j \approx 50$ due to accumulation of rounding errors. This behavior depends on the chosen ξ and the breakdown is more prominent when $|\xi|$ is large. Here the displacement $\xi = 3 - 2\imath$ was chosen to emphasize this effect. For instance, when $\xi = 1$, a similar exponential breakdown appears for $j \approx 400$ instead.

C Truncated approximate matrix exponential (TAME)

When it comes to numerically generating truncated representations of unitary operators, both direct calculation and the recurrent formulae have fundamental issues leading to significant rounding errors or numerically invalid expressions. The matrix exponential function avoids these issues mostly at the cost of truncation errors and their subsequent amplification. However, the observations in Figure 3.2 also suggest that these errors tend to be significant only in higher regions of said matrices.

This opens up a new possibility of approximating the exponential operators. The matrix exponential can be computed on a sufficiently higher dimension d_1 and only then the result truncated to the required d_0, thus avoiding the erroneous areas, while, at the same time, keeping the computational dimension d_1 low enough to avoid needlessly increasing the time of computation. We call this approach **truncated approximate matrix exponential** (TAME).

Consider the approximation of the truncated displacement operator constructed this way,

$$\operatorname*{trunc}_{d_0}\{\hat{D}(\xi)\} \approx \operatorname{tame}(\hat{Q}, d_1, d_0) \coloneqq \operatorname*{trunc}_{d_0}\left\{\operatorname{expm}\left(\operatorname*{trunc}_{d_1}\{\hat{Q}\}\right)\right\} . \tag{3.22}$$

Here d_1 represents the initial working dimension and d_0 the final dimension of the target TFS. Following (3.13) we set $\operatorname{trunc}_{d_1}\{\hat{Q}\} \coloneqq \xi \operatorname{trunc}_{d_1}\{\hat{a}^\dagger\} - \xi^* \operatorname{trunc}_{d_1}\{\hat{a}\}$.

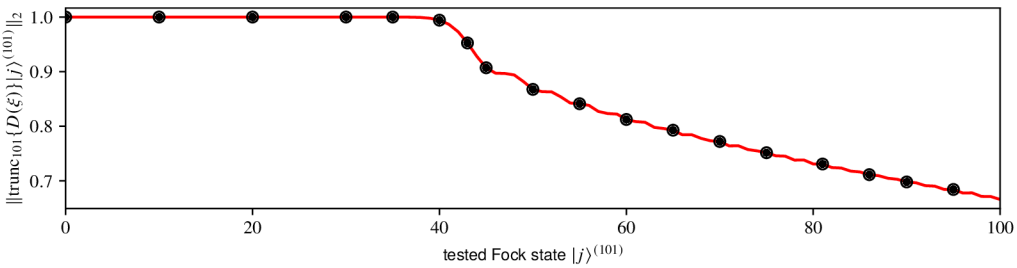

Figure 3.3. Normalisation $\|\operatorname{trunc}_{101}\{\hat{D}(3-2\imath)\}\,|j\rangle^{(101)}\|_2$ of displaced Fock states $0 \le j \le 100$. The matrix was constructed using the closed form formula (black bullets) and approximated with TAME (red, solid) where we set $d_0 = 101$ and $d_1 = 161$. In both plots the dimension d_1 for TAME was determined via Algorithm 3.1.

Comparison of $\operatorname{trunc}_{101}\{\hat{D}(3-2\imath)\}$ constructed using the closed form formula (3.14) and approximated with TAME is presented in Figure 3.3. The dimension d_0 as well as the displacement magnitude $|\xi|$ were chosen to accommodate the established limitations of (3.14). The secondary dimension $d_1 = 161$ was chosen high enough to suppress the effects of truncation errors. The plot suggests that our method produces results equal to the closed form formula in terms of the normalisation (3.20). Further comparison of individual matrix elements reveals that, on average, the approximate matrix matches (3.14) up to 14 decimal places with the worst difference matching only up to 11 decimal places.

What remains to be determined is the proper choice, or rather the methodology of choosing a sufficiently large working dimension d_1 given the target dimension d_0. In the subsequent paragraphs we are going to show that it is practical to set the dimension d_1 as small as possible. The de-facto standard **scaling and squaring** matrix exponentiation algorithm [206, 207] relies on matrix multiplication with the actual number of matrix products depending on the binary logarithm of the 1–norm [208] of the exponentiated matrix. The 1–norm [208] of the $\operatorname{trunc}_{d_1}\{\hat{Q}\}$ argument reads

$$\|\operatorname*{trunc}_{d_1}\{\hat{Q}\}\|_1 = \|\xi \operatorname*{trunc}_{d_1}\{\hat{a}^\dagger\} - \xi^* \operatorname*{trunc}_{d_1}\{\hat{a}\}\|_1 = |\xi|\left(\sqrt{d_1 - 1} + \sqrt{d_1 - 2}\right) \approx 2|\xi|\sqrt{d_1} , \tag{3.23}$$

where the final approximation holds asymptotically. Therefore the asymptotic computational complexity of the matrix exponential in scales as $O(\log_2 d_1)$ in terms of matrix products. The complexity of each matrix multiplication, specified in terms of FP operations, depends on the

algorithm it utilizes. A naive textbook implementation scales as poorly as $O(d_1^3)$, whereas the more sophisticated Strassen algorithm [209] scales approximately as $O(d_1^{2.807})$. Consequently the computational complexity of (3.22) scales as $O(d_1^{2.807} \log_2 d_1)$ under optimal conditions. It is therefore imperative to keep the dimension d_1 as low as possible.

```
1:  procedure FindDimension ( d_0, ε_1 := 10^{-13}, h := 10 )
2:      q := d_0 + 1
3:      M_q := tame(Q, q, d_0)
4:      while q < h · d_0 do
5:          p := q + 1
6:          M_p := tame(Q, p, d_0)
7:          if ‖M_q − M_p‖_max < ε_1 then
8:              return q
9:          end if
10:         q := p
11:         M_q := M_p
12:     end while
13:     raise error No solution found.
14: end procedure
```

Algorithm 3.1. A simple iterative search for the least dimension q such that there is a match on d_0 dimensional region between two q and $p := q + 1$ dimensional matrices constructed using TAME. Here, the element-wise matrix max-norm is defined with $\|M\|_{\max} := \max_{ij}|[M]_{ij}|$.

We propose a simple iterative algorithm for finding optimal d_1. Suppose a sufficiently sized $\mathrm{expm}(\mathrm{trunc}_q\{\hat{Q}\})$ matrix is correct on some region spanning $\{|0\rangle^{(u)}, \ldots, |u-1\rangle^{(u)}\}$ where $u \leq q$. Suppose the matrix exponential (expm) algorithm is also consistent: for a differently sized $\mathrm{trunc}_p\{\hat{Q}\}$ matrix with dimension $p > q$ the computed matrix exponential is correct on a region of at least the same size. Given these assumptions, which are upheld by the standard expm implementation [206, 207], we introduce the Algorithm 3.1 as follows.

First, take the desired dimension d_0 of the correct region and set an equality tolerance ϵ_1 for small numbers. The condition with $\epsilon_1 = 10^{-13}$ proclaims two numbers identical if they match up to their twelfth decimal place. Next, search for a pair of larger matrices such that their d_0 regions match. The search process is significantly simplified by taking the dimension of the second larger matrix to be constantly shifted from the first larger matrix. To improve its speed one of the matrices is recycled in the next iteration instead of recalculating it every time. The depth of the search is specified by the factor h. Once the search algorithm finishes *successfully*, the least d_1 is obtained.

In our experience the dimension is found somewhere well below $q = 3 \cdot d_0$ in the case of displacement, hence we set the depth h above that.

D Verification of approximated matrices

In general, the matrix (3.22) constructed via TAME can not be compared simply by comparing its elements against some exact solution for the obvious reason: if the exact solution was known, we would not be in this situation in the first place.

Normalisation (3.20), or more precisely, the implied necessary condition of unitarity

$$\max_{ij}|[G]_{ij}| \leq 1 \,, \tag{3.24}$$

was used to detect outright incorrect matrices in Figure 3.2, but alas, necessary conditions alone can not be used to prove the matrix correct. It was demonstrated in the same figure that employing the recurrent formula [185] in construction of $\mathrm{trunc}_F\{\hat{D}(\xi)\}$ is ill-advised due to accumulation

and consequent amplification of rounding errors over the course of the computation. While the recurrent formula can not be used safely to construct an arbitrary truncated displacement matrix, it can still be utilized to determine whether a candidate matrix, for example one constructed via TAME (3.22), possesses the appropriate structure as the recurrent formulae define structural relations between neighboring matrix elements.

The relations relations Eq. (56–58) from [185] can be repurposed to construct an error matrix

$$\begin{aligned}
[E]_{0,0} &= [G]_{0,0} - \exp\left(-\frac{1}{2}|\xi|^2\right) \\
[E]_{i,0} &= [G]_{i,0} - \frac{\xi}{\sqrt{i}}[G]_{i-1,0} \\
[E]_{i,j} &= [G]_{i,j} - \left(\frac{\sqrt{i}}{\sqrt{j}}[G]_{i-1,j-1} - \frac{\xi^*}{\sqrt{j}}[G]_{i,j-1}\right)
\end{aligned} \tag{3.25}$$

for a given candidate matrix G. The rounding errors are not amplified in computation of the error matrix as there is no recursion. Its elements $[E]_{ij}$ give the difference between the actual elements $[G]_{ij}$ of the candidate matrix and the values they should have been based on their neighbors, $[G]_{i-1,j-1}$ and $[G]_{i,j-1}$, and the structural constraints given in [185].

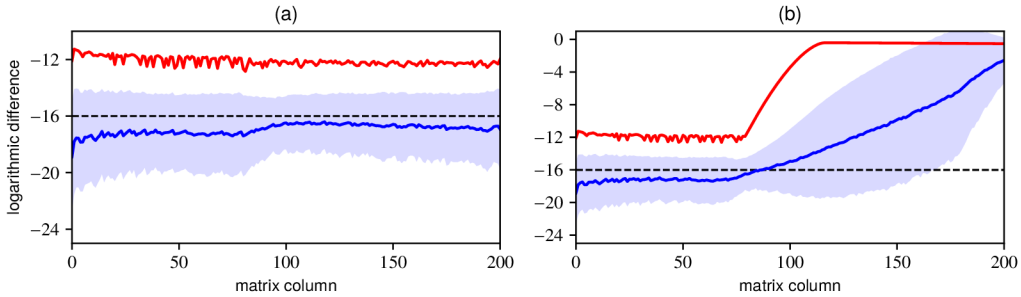

Figure 3.4. Verification of the $\mathrm{trunc}_{201}\{\hat{D}(3-2\imath)\}$ matrix approximated using **(a)** TAME ($d_0 = 201$ and $d_1 = 277$) and **(b)** plain matrix exponential ($d_0 = 201$). Blue lines mark the row-wise $\mathrm{mean}_i(L_{ij})$ values, light-blue region stretches a standard deviation $\mathrm{std}_i(L_{ij})$ away from the mean. The maximal difference $\max_i(L_{ij})$ within each column is represented by the red line. The dashed horizontal line corresponds to the unit round-off in double precision floating point number representation. **(a)** The matrix is structurally correct. The average differences are negligible, their values falling below the unit round-off. The maximal differences match up to 11 decimal places. **(b)** The matrix maintains correct structure in its first third. The truncation errors manifest in the rest of the matrix as an exponential explosion in the maximal difference (around the 100th column) and a steady rise in the mean value.

The decimal logarithm of the difference $[L]_{ij} = \log_{10}|[E]_{ij}|$ for $\mathrm{trunc}_{201}\{\hat{D}(3-2\imath)\}$ approximated using (a) TAME ($d_0 = 201$, $d_1 = 277$) and (b) the plain matrix exponential ($d_0 = 201$) is compared in Figure 3.4. Each plot shows the row-wise $\mathrm{mean}_i([L]_{ij})$ value with blue line. The surrounding light-blue area stretches one standard deviation $\mathrm{std}_i([L]_{ij})$ from the mean. The maximal difference $\max_i([L]_{ij})$ within each column is represented by the red line. Finally the dashed black horizontal line (at -16) roughly corresponds to the double precision unit round-off [191].

In Figure 3.4 (a) the matrix is structurally correct, with the maximal difference still matching up to 11 decimal places. On average the differences fall below the unit round-off, essentially making the errors negligible. In Figure 3.4 (b) the matrix constructed using the plain matrix exponential maintains the correct structure in the first third of its columns, however, the truncation errors begin to manifest at that point. This can be observed as an exponential explosion in the maximal difference (around the 75th column) and a steady rise in the mean value. A similar manifestation of truncation errors was observed in Figure 3.2 where the columns incorrectly retained their normalization as if the truncated matrix remained unitary.

E Conclusions

We analyzed the numerical accuracy of several currently available methods [185, 199] used in construction of the truncated coherent displacement operator, an essential ingredient of state preparation in quantum optics [50, 87, 92, 93] and many protocols used in quantum information processing [19, 50, 82, 158, 159, 199]. We proposed an alternative approach promising a better accuracy. Our method is based on the standard matrix exponential [206, 207] with truncated argument. We compute the matrix exponential on a higher-dimensional space and truncate the resulting matrix to the target dimension, thus stripping erroneous matrix elements away from the truncated displacement operator. To avoid negatively impacting computational performance, the higher dimension should be ideally kept as low as possible. To this end we provide an off-line search algorithm that can be used to determine its optimal value. To ascertain the accuracy of the resulting matrix we complement the construction method with a verification strategy based on the recurrent formulae discussed in [185].

The proposed method was successfully used in numerical simulation of a simple photonic circuit designed for construction of approximate cubic states discussed in Chapter 2: Preparing Approximate Cubic States.

Chapter 4

Protecting Coherent Schrödinger States in Transit

This chapter summarizes the methods and discusses the main results of the upcoming article *"Adapting coherent-state superpositions in noisy channels"* [210].

Coherent Schrödinger (CS) states, defined as quantum superposition of coherent states with different amplitudes, can be used directly to encode quantum information [51, 52, 75, 102, 129, 131–135] in quantum computation protocols, used for error correction [134] and exploited in GKP state production [50], where they serve the role of non-Gaussian building blocks [50, 102, 135]. They can be further employed in quantum communication protocols [75, 139–141], quantum sensing [142] and spectroscopy [143].

Their utility in various applications comes from their non-Gaussian nature. Their non-Gaussian features diminish in the presence of Gaussian loss [109, 144–149] and additive noise. One of the challenges faced in quantum optics is decoherence, mainly due to optical loss and thermal noise, and while high quality non-Gaussian quantum states can be used for error correction [50, 134, 136–138], this decoherence severely limits their preparation and propagation [88, 103]. Energy loss can never completely remove certain quantum non-Gaussian features from quantum states [211], however, losing half of the state to the environment is enough to completely obliterate any negativity of the Wigner function, thus preventing any possibility of quantum advantage [126]. Loss combined with noise present in the environment makes decay of CS states even faster.

Effects of loss in photonic qubit systems can be mitigated by pre-processing of the optical signals [212–214] or through channel engineering [215]. Similarly, CS states can be made more resilient to loss by applying a suitable deterministic squeezing operation [109, 144–149] before their transmission. This mitigation protocol has been demonstrated for purely lossy channels in [109].

The extent to which these methods can be used to mitigate loss combined with added channel noise had not been, to the best of our knowledge at the time, studied before. To address this question we considered a CS state propagating through a general sequence of quantum channels incorporating loss and added phase-sensitive noise. Based on optimal deterministic squeezing operations maximizing the central negativity of the Wigner function, we derived a sufficient and necessary condition, that must to be satisfied for any negativity present in the Wigner function of the odd-parity CS state to be preserved. In addition, we generalized the condition to include even-parity CS states as well, however, at the cost of sufficiency. If there are any negative values of the Wigner function to exist, the generalized necessary condition must be satisfied, however, their existence is not guaranteed. Our analysis focusing mainly on the negativity of the Wigner function was complemented by adapting the squeezing operations to maximize the Hilbert-Schmidt

distance between CS states of opposite parities transmitted through the decohering channels.

This chapter is divided into three sections; the mathematical and physical methodology is introduced at first, followed by the discussion of results, and closed off with a summary of the findings presented in this chapter and the referenced paper [210].

A Methodology

Coherent Schrödinger (CS) states are quantum superpositions of two coherent states with identical amplitudes and opposite phases. We recognize two types of CS states based on their parity,

$$|\xi,\pm\rangle = \frac{1}{\sqrt{2}}\frac{|\xi\rangle \pm |-\xi\rangle}{\sqrt{1\pm\exp(-2|\xi|^2)}} \tag{4.1}$$

where $|\xi\rangle$ denotes coherent states — eigenstates of the annihilation operator $\hat{a}$. The symbol $|\xi,+\rangle$ stands for the even-parity and $|\xi,-\rangle$ the odd-parity CS state. Their respective Wigner functions,

$$W_{\xi,\pm}(X,P) = \frac{1}{2}\frac{w_{\xi,\xi}(X,P) \pm \left[w_{\xi,-\xi}(X,P) + w_{-\xi,\xi}(X,P)\right] + w_{-\xi,-\xi}(X,P)}{1\pm\exp(-2|\xi|^2)}\,, \tag{4.2}$$

defined in variables corresponding to quadrature operators with $[\hat{x},\hat{p}] = \imath$, are expressed in terms of the complex-exponential building blocks

$$\begin{aligned} w_{\xi,\xi}(X,P) &= \frac{1}{\pi}\exp\left(-(X-X_0)^2-(P-P_0)^2\right)\,,\\ w_{\xi,-\xi}(X,P) &= \frac{1}{\pi}\exp\left(-(X-\imath P_0)^2-(P+\imath X_0)^2\right)\exp\left(-2|\xi|^2\right)\,, \end{aligned} \tag{4.3}$$

where we set $\sqrt{2}\xi \equiv X_0 + \imath P_0$ and therefore $2|\xi|^2 \equiv X_0^2 + P_0^2$. As for the final building block, omitted in (4.3), we have $w_{-\xi,\xi}(X,P) \equiv \{{}^*w_{\xi,-\xi}(X,P)\}$. These two complex-exponential blocks add up to a real-valued cosine; the total Wigner function (4.2) remains real.

The Gaussian channels under our consideration can be described with a Gaussian kernel

$$K(X,P,X',P') = \frac{\pi^{-1}}{\sqrt{\sigma_X\sigma_P}}\exp\left(-\frac{(X'-f_X X)^2}{\sigma_X}-\frac{(P'-f_P P)^2}{\sigma_P}\right) \tag{4.4}$$

where $f_X, f_P, \sigma_X, \sigma_P \in \mathbb{R}$ parametrize the channel and their exact values depend on the particular channel. The kernel function (4.4) accommodates a broad range of channels beyond loss, including those where the transmitted states are squeezed before and after their interaction with the environment. It is, however, limited to channels preserving the separability of the quadrature variables. In our analysis we only consider channels with thermal environment, where the thermal state is axis-aligned with the transmitted CS state. This can be guaranteed by a using a phase-shift operation before their transmission.

The Wigner function $W'_{\xi,\pm}(X',P')$ of the transmitted state is given by the integral transform

$$W'_{\xi,\pm}(X',P') = \iint W_{\xi,\pm}(X,P)K(X,P,X',P')\,\mathrm{d}X\mathrm{d}P \tag{4.5}$$

of its initial Wigner function $W_{\xi,\pm}(X,P)$ facilitated by the kernel function $K(X,P,X',P')$ representing the quantum channel (4.4). When the CS state propagates through the channel, its complex-exponential building blocks (4.3) transform into

$$\begin{aligned} w'_{\xi,\xi}(X',P') &= \frac{1}{\pi}\frac{1}{\sqrt{V_X V_P}}\exp\left(-\frac{(X'-f_X X_0)^2}{V_X}-\frac{(P'-f_P P_0)^2}{V_P}\right)\,,\\ w'_{\xi,-\xi}(X',P') &= \frac{1}{\pi}\frac{1}{\sqrt{V_X V_P}}\exp\left(-\frac{(X'-\imath f_X P_0)^2}{V_X}-\frac{(P'+\imath f_P X_0)^2}{V_P}\right)\exp\left(-2|\xi|^2\right)\,, \end{aligned} \tag{4.6}$$

where $V_X = \sigma_X + f_X^2$ and $V_P = \sigma_P + f_P^2$. Together, these form the transformed Wigner function

$$W'_{\xi,\pm}(X',P') = \frac{1}{2}\frac{w'_{\xi,\xi}(X',P') \pm \left[w'_{\xi,-\xi}(X',P') + w'_{-\xi,\xi}(X',P')\right] + w'_{-\xi,-\xi}(X',P')}{1 \pm \exp(-2|\xi|^2)} \tag{4.7}$$

with structure similar to the initial Wigner function (4.2) since both the integral kernel (4.5) and the complex-exponential fragments (4.3) are Gaussian functions separable in terms of X and P.

Criteria for Negativity

Negative Wigner functions exclude Gaussian behavior of quantum states [125, 127]. One of the prominent features of odd-parity CS states is the central negativity of their Wigner function. While it is only a sufficient condition for quantum non-Gaussianity [127], its reduction can be used as a qualitative indicator of observability of the transmitted CS state above measurement and statistical noise [109, 149]. Central negativity also offers an experimental advantage as its measurement does not require a full state tomography [216–219]. In quantum optics, its value can be obtained directly as an expectation value of the photon number parity operator [220] or computed from its photon number distribution [184].

It is convenient to rewrite the complex-exponential Wigner function (4.7) of the transformed CS state into its manifestly real form. Its coefficients $f_X, f_P, \sigma_X, \sigma_P, V_X$ and V_P are all real and positive.

$$\begin{aligned} W'_{\xi,\pm}(X',P') = \; & 2f_\pm \exp\left(-\frac{X'^2}{V_X} - \frac{P'^2}{V_P}\right)\Bigg\{ \\ & \exp\left(-\frac{f_X^2}{V_X}X_0^2 - \frac{f_P^2}{V_P}P_0^2\right)\cosh\left(2\left[\frac{f_X}{V_X}X_0X' + \frac{f_P}{V_P}P_0P'\right]\right) \\ & \pm \exp\left(-\frac{\sigma_X}{V_X}P_0^2 - \frac{\sigma_P}{V_P}X_0^2\right)\cos\left(2\left[\frac{f_P}{V_P}X_0P' - \frac{f_X}{V_X}P_0X'\right]\right)\Bigg\}, \end{aligned} \tag{4.8}$$

where the factors $f_\pm$ represent the normalization, given as

$$f_\pm^{-1} = 2\pi\sqrt{V_XV_P}\left(1 \pm \exp(-X_0^2 - P_0^2)\right) . \tag{4.9}$$

Let us begin with the **sufficient and necessary** condition for the existence of any negative area in the Wigner function of the odd-parity CS state. It is only natural to consider the central negativity in this particular case. The formula (4.8) simplifies into

$$W'_{\xi,-}(0,0) = 2f_-\left\{\exp\left(-\frac{f_X^2}{V_X}X_0^2 - \frac{f_P^2}{V_P}P_0^2\right) - \exp\left(-\frac{\sigma_X}{V_X}P_0^2 - \frac{\sigma_P}{V_P}X_0^2\right)\right\} \tag{4.10}$$

This expression will be negative if and only if

$$\exp\left(-\frac{f_X^2}{V_X}X_0^2 - \frac{f_P^2}{V_P}P_0^2\right) - \exp\left(-\frac{\sigma_X}{V_X}P_0^2 - \frac{\sigma_P}{V_P}X_0^2\right) < 0 , \tag{4.11}$$

that is, if and only if, the second exponential is greater than the first one. Comparing their arguments directly reveals the condition

$$-X_0^2\left(\frac{f_X^2f_P^2 - \sigma_X\sigma_P}{V_XV_P}\right) - P_0^2\left(\frac{f_X^2f_P^2 - \sigma_X\sigma_P}{V_XV_P}\right) < 0 \iff \boxed{f_X^2f_P^2 - \sigma_X\sigma_P > 0} . \tag{4.12}$$

The central point of the odd-parity CS state will be negative if and only if $f_Xf_P - \sigma_X\sigma_P > 0$. Notably this inequality does not depend on the state. It depends solely on the channel. This concludes the derivation for the odd-parity state. ■

The condition for even-parity states is slightly harder to obtain. Once again, we note that we are only interested in a **necessary** condition for existence of negativity anywhere within the Wigner function. In other words, we are looking for a condition that, if violated, will preclude existence of any negativity within the Wigner function. This allows us to be somewhat liberal in the manipulation of the expression (4.8).

We begin with the observation that there are infinitely many (X', P') pairs that satisfy

$$\pm\cos\left(2\left[\frac{f_P}{V_P}X_0P' - \frac{f_X}{V_X}P_0X'\right]\right) \equiv -\left|\cos\left(2\left[\frac{f_P}{V_P}X_0P' - \right]\right)\right| . \tag{4.13}$$

The rest of the proof assumes the Wigner function (4.8) is evaluated only at points of the phase space that satisfy this condition. With this assumption in mind, we can rewrite the curly braced expression from (4.8) into

$$\exp(A)\cosh(B) - \exp(C)\,|\cos(D)| < 0 \tag{4.14}$$

where we have substituted the arguments of the exponential, geometric and hyperbolic functions for simplicity. Since the hyperbolic cosine is always positive and lower bound by 1, we have

$$\begin{aligned}
\exp(A)\cosh(B) - \exp(C)\,|\cos(D)| < 0 &\iff \\
\exp(A) < \exp(C)\frac{|\cos(D)|}{\cosh(B)} &\iff \\
\exp(A) < \exp(C) &\iff \\
-X_0^2\left(\frac{f_X^2 f_P^2 - \sigma_X\sigma_P}{V_XV_P}\right) - P_0^2\left(\frac{f_X^2 f_P^2 - \sigma_X\sigma_P}{V_XV_P}\right) < 0 &\iff \\
\boxed{f_X^2 f_P^2 - \sigma_X\sigma_P > 0} .&
\end{aligned} \tag{4.15}$$

Where we obtained the third inequality $\exp(A) < \exp(C)$ as an upper bound on the right hand side of the second one. The condition $f_X^2 f_P^2 - \sigma_X\sigma_P > 0$ then follows. This concludes the derivation for even-parity CS states. ■

The **necessary** condition applies to both even and odd parity CS states. If violated, there will be **no** negative area at all present in the Wigner function of the transmitted state. Our findings are summarized in the following pair of boxes.

If the transformed Wigner function (4.7) of the transmitted CS state is to attain negative values anywhere in its domain, the channel must **necessarily** satisfy $f_X^2 f_P^2 - \sigma_X\sigma_P > 0$. In particular,

$$\exists (X,P) \in \mathbb{R}^2 : W'_{\xi,\pm}(X,P) < 0 \implies f_X^2 f_P^2 - \sigma_X\sigma_P > 0 . \tag{4.16}$$

It can be equivalently expressed in terms of its negation.

$$f_X^2 f_P^2 - \sigma_X\sigma_P < 0 \implies \forall (X,P) \in \mathbb{R}^2 : W_{\xi,\pm}(X,P) > 0 \tag{4.17}$$

precludes negativity anywhere within the Wigner function (4.7). Both conditions are independent of the magnitude and parity of the transmitted CS state and depend only on the parameters of the channel.

The condition (4.16) is both **necessary and sufficient** for the existence of the central negativity in the Wigner function of a transmitted odd-parity CS state.

The Hilbert-Schmidt distance

The opposite-parity CS states form an orthonormal computational basis [51, 52, 56, 75, 129, 131, 133]. Their orthogonality, which deteriorates as their quan-

tum non-Gaussian features decay due to decoherence, can be quantified with the directly measurable [221–224] Hilbert-Schmidt distance [225].

The Hilbert-Schmidt distance, defined in terms of Wigner functions (4.7),

$$\begin{aligned}\Delta_\xi &= 2\pi \iint_{\mathbb{R}^2} \left[W'_{\xi,+}(X,P) - W'_{\xi,-}(X,P)\right]^2 \mathrm{d}X\mathrm{d}P \\ &= P_{\xi,+} - 2Q_\xi + P_{\xi,-}\end{aligned} \tag{4.18}$$

effectively pits the purities $P_{\xi,\pm}$ of the transmitted CS states against their mutual overlap Q_ξ. The distance is bounded, $0 \leq \Delta_\xi \leq 2$, both from below and above. It can be expressed analytically; the formulae for purity and the mutual overlap read

$$\begin{aligned}P_{\xi,\pm} &= 2\pi \iint_{\mathbb{R}^2} W^2_{\xi,\pm}(X,P)\ \mathrm{d}X\mathrm{d}P \\ &= \frac{1}{\sqrt{V_X V_P}} \frac{1+M+N\pm 4L}{2\left(1\pm\exp\left[-X_0^2-P_0^2\right]\right)^2} \\ O_\xi &= 2\pi \iint_{\mathbb{R}^2} W_{\xi,+}(X,P) W_{\xi,-}(X,P)\ \mathrm{d}X\mathrm{d}P \\ &= \frac{1}{\sqrt{V_X V_P}} \frac{1+M-N}{2\left(1-\mu\exp\left[-2X_0^2-2P_0^2\right]\right)}\ .\end{aligned} \tag{4.19}$$

The individual factors in both expressions can be obtained directly by computing the underlying Gaussian integrals. Their closed forms are

$$\begin{aligned}M &= \exp\left(-2\frac{f_X^2}{V_X}X_0^2 - 2\frac{f_P^2}{V_P}P_0^2\right) \\ N &= \exp\left(-2X_0^2-2P_0^2\right) + \exp\left(-2\frac{\sigma_X}{V_X}P_0^2 - 2\frac{\sigma_P}{V_P}X_0^2\right) \\ L &= \exp\left(-\left[\frac{f_X^2}{2V_X}+\frac{f_P^2}{2V_P}+\frac{\sigma_P}{V_P}\right]X_0^2 - \left[\frac{f_X^2}{2V_X}+\frac{f_P^2}{2V_P}+\frac{\sigma_X}{V_X}\right]P_0^2\right)\times \\ &\quad \cos\left(X_0\left[\frac{f_X^2}{V_X}+\frac{f_P^2}{V_P}\right]P_0\right)\ .\end{aligned} \tag{4.20}$$

B Discussion and results

Even though the methods described within Methodology permit a broad class of Gaussian channels, our focus lies on a specific type of experimentally relevant Gaussian channels — those combining loss with additive asymmetric thermal noise. The channel of this type, its scheme depicted in Figure 4.1, can be modeled with an unbalanced beam splitter where the transmitted signal interacts with the environment in a generally asymmetrical thermal state, which can be understood as an initially symmetric thermal state that underwent squeezing. In our model we assume that the parameters of the channel are known. It has been established [109, 147, 148] that the rapid decay of negative values in Wigner functions of CS states due to pure loss (vacuum environment) can be mitigated with adaptive pre-squeezing operation prior to their transmission through the lossy channel. Our search for methods capable of increasing their resilience against noise starts extends these approaches; the protective squeezing of the signal mode is reflected within the scheme.

These channels can be associated with the kernel (4.4) and characterized through the param-

eters

$$f_X = \sqrt{\eta}\mathrm{e}^{-\gamma}, \quad \sigma_X = 2(1-\eta)\mathrm{e}^{-2\gamma_t}V\,, \\ f_P = \sqrt{\eta}\mathrm{e}^{+\gamma}, \quad \sigma_P = 2(1-\eta)\mathrm{e}^{+2\gamma_t}V\,, \tag{4.21}$$

where γ gives the squeezing rate of the pre-squeezing operation applied to the signal state, η defines the (intensity) transmittance of the channel. The signal is mixed with the environment, an asymmetric thermal state, which can be parametrized by its initial symmetric variance V and squeezing rate γ_t of the asymmetrizing operation. Asymmetric thermal states remain classical for squeezing rates $|\gamma_t| \leq \log\sqrt{V}$ as neither quadrature variance, $V_\pm = \exp(\pm 2\gamma_t)V$, becomes squeezed below the vacuum threshold. The environment noise becomes non-classical beyond this limit.

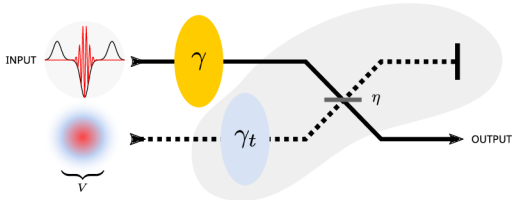

Figure 4.1. The signal (solid line) is transmitted through a lossy channel represented by a beam splitter with transmittance η where it interacts with the environment (dashed line). The environment is assumed to be in an axis-aligned asymmetric thermal state, which can be interpreted as a symmetric thermal state characterized by its variance V and the associated squeezing rate γ_t. The signal state can be protected against decoherence with an optional pre-squeezing operation. Its squeezing rate γ can be adapted to offer the best protection of the transmitted CS state.

Negative Wigner functions exclude Gaussian behavior of quantum states [125, 127]. One of the prominent features of the odd-parity CS states is the central negativity of their Wigner function. While central negativity is only a sufficient condition for quantum non-Gaussianity [127], its reduction can be used as a qualitative indicator of observability of the transmitted CS state above measurement and statistical noise [109, 149]. It also offers an experimental advantage as its measurement does not require a full state tomography [216–219]. In optics, its value can be obtained directly as an expectation value of the photon number parity operator [220] or computed from its photon number distribution [184].

This makes the central negativity (CN) of odd-parity CS states a perfect measure for quantification of the protection against decoherence offered by the pre-squeezing. The criterion (4.16) can be immediately used to determine a region of feasible parameters (4.21) of the channel, independent of both γ and γ_t, bounded by

$$\frac{2V}{1+2V} < \eta < 1 \quad \text{and} \quad 0 < V < \frac{\eta}{2(1-\eta)}\,, \tag{4.22}$$

where the negativities in the transmitted state survive. No amount of pre-squeezing γ is going to protect CS states transmitted through channels (4.21) with parameters outside of this region.

An interesting behavior can be observed by plotting out the optimal squeezing rates of the protective pre-squeezing operation for differently asymmetries of the thermal noise. As illustrated in Figure 4.1 for a particular odd-parity CS state, the individual optimal rates γ are constantly shifted from the squeezing rate respective to the case of symmetric thermal noise; the shifts equal to the asymmetry γ_t.

The optimal protective pre-squeezing operation can be interpreted as a pair of virtual squeezing operations with rates γ_0 and γ_1, joined together into a single physical squeezing operation with $\gamma = \gamma_0 + \gamma_1$ rate. The first virtual squeezer, with γ_0, realizes the protective pre-squeezing of the transmitted CS state, while the other squeezer, with squeezing rate $\gamma_1 \equiv \gamma_t$, reshapes the pre-squeezed state to match the asymmetry of the environment. The optimal squeezing rate γ_0

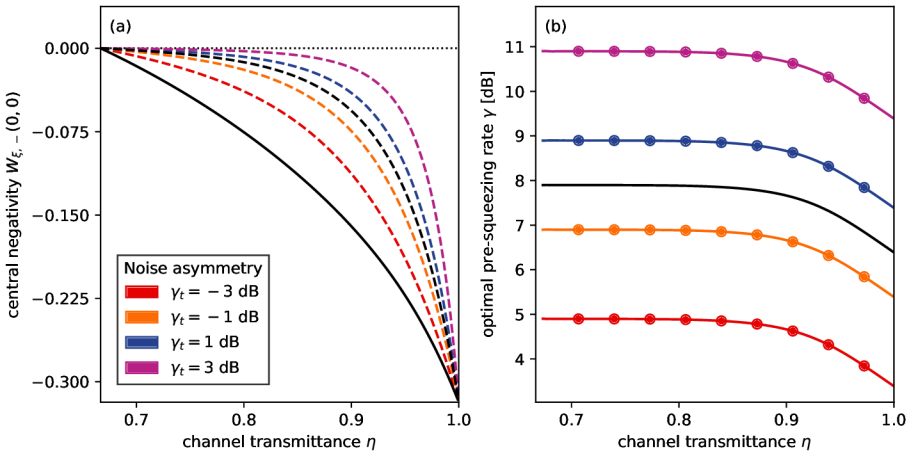

Figure 4.2. Adaptive pre-squeezing is used to protect an odd-parity CS state (with $\sqrt{2}\xi = 3$) from decoherence due to loss and thermal noise (with $V = 1$, double the variance of the vacuum state) with varying asymmetry γ_t. Distinct colors are used to encode different rates of asymmetry, whereas black represents the symmetric case with $\gamma_t = 0$. **(a)** The best attainable central negativity. Dashed lines represent the CN achieved without protection. The solid black line represents the best attainable CN; it does not depend on the asymmetry of the thermal noise. **(b)** Optimal pre-squeezing rates γ follow the same color scheme. Colored lines represent optimal rates for different asymmetries. The lines are constantly shifted by the value of γ_t from the solid black line, which represents the optimal pre-squeezing γ found for the symmetric thermal state (with $\gamma_t = 0$). The colored bullet points correspond to γ_t added to its values at regular intervals to emphasise the constant shifts.

of the protective pre-squeezing operation itself depends on the CS state, the excess of the thermal noise and the transmittance of the channel. It must be determined numerically on a case by case basis. The reshaping of the state, due to the second virtual squeezer, can be interpreted as a symmetrization of the environment. The virtual squeezing operations γ_1 and γ_t have identical squeezing rates; these two operations can be propagated through the beam splitter in Figure 4.1. The resulting scheme reduces into the actual protective pre-squeezing operation γ_0 and a regular loss channel with a symmetric thermal noise. With this interpretation, it is appropriate to focus solely on the cases with **symmetric** noise.

The adaptation of an odd-parity CS state with $\sqrt{2}\xi = 3$, transmitted through the lossy channel (4.21) with different amounts of symmetric thermal noise, is investigated in Figure 4.3. The thermal noise is characterized by its variance $V \in \{0.5, 1.0, 1.5, 2.0\}$, where the thermal state with $V = 0.5$ corresponds to pure loss. The best attainable CN of odd-parity states is shown in Figure 4.3 (a). The least viable transmittance is determined with the condition (4.22) and only the results where the transmitted CS state exhibits CN are presented in the figure. The dashed lines represent cases without any protective pre-squeezing, wheres the solid solid lines, corresponding to the optimal adaptation of the transmitted CS state, exhibit significantly improved CN. Figure 4.3 (b) demonstrates the optimal squeezing rates γ of the pre-squeezing operation. The optimal squeezing rate γ does not exhibit trivial dependence on the variance V and must be determined numerically on a case by case basis.

Adverse effects of asymmetric thermal noise can be mitigated with squeezing operations adapted to the asymmetry and the overall amount of the thermal noise in addition to adaptation for the loss rate and the transmitted CS state itself. The adaptation process can be understood as a combination of the protective pre-squeezing in the sense of [109, 147, 148] and an additional squeezing operation, which effectively removes the asymmetry. Consequently, in the analytical models used for the optimization, we can freely replace the lossy channels with asymmetrical thermal environment by lossy channels with equivalent symmetrical thermal noise.

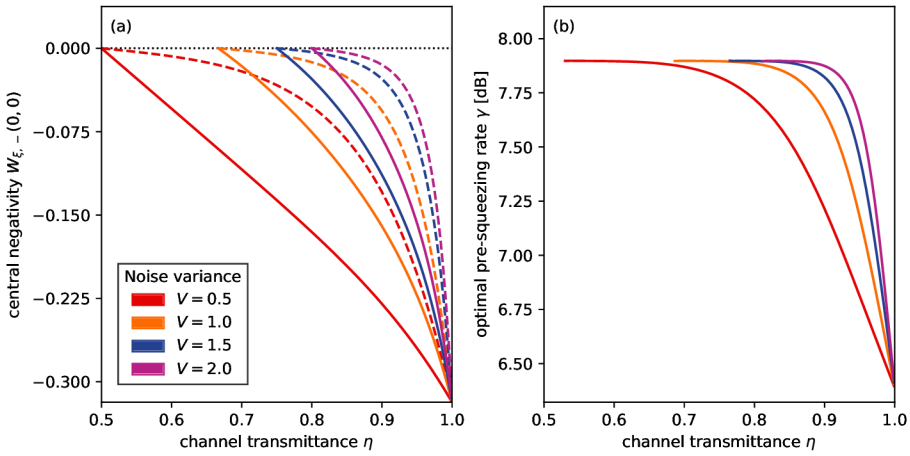

Figure 4.3. Adaptive pre-squeezing is used to protect odd-parity CS state (with $\sqrt{2}\xi = 3$) from decoherence due to loss and symmetric thermal noise characterized by its variance $V \in \{0.5, 1.0, 1.5, 2.0\}$. Colors are used to distinguish between individual variances. **(a)** Dashed lines represent CN without protection. Solid lines correspond to significantly improved CN attained by optimally pre-squeezed CS states. **(b)** Optimal pre-squeezing rate γ does not exhibit trivial dependence on the variance V of the thermal noise.

Adaptation in composite channels

Quantum states can propagate through diverse environments during their lifetime. A sequence of Gaussian channels (4.4) can be concatenated together to form another Gaussian channel which can be described with the same formalism. Similarly a Gaussian channel can be decomposed into more Gaussian channels [226]. Simple decohering Gaussian channels have been extensively discussed in the literature [109, 147, 148], as well as in the previous paragraphs with some useful observations about symmetrization of the environment.

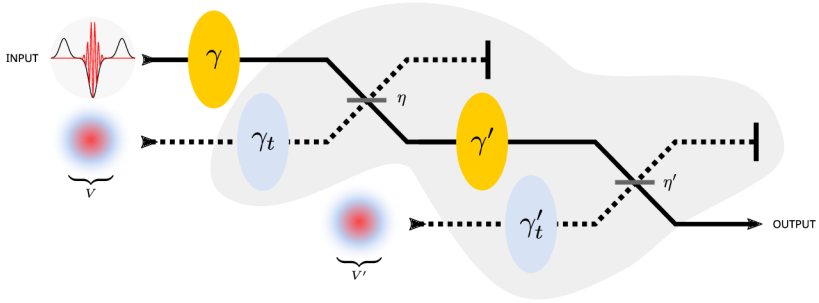

Figure 4.4. Illustration of a composite channel comprising a pair of lossy channels with pre-squeezing (γ) and mid-squeezing (γ'). The first channel is parametrized by (V, γ_t) describing the asymmetric thermal state and η determining its transmittance. Parameters of the second channel are distinguished by primes.

Protection against decoherence in composite quantum channels could benefit from intermediate squeezing between the channels, as illustrated in Figure 4.4. The signal CS state is pre-squeezed, passes through the first beam splitter. It is then squeezed again before passing through the second beam splitter. It may be optionally squeezed as it leaves the channel, however, the final squeezing does not affect the quantum non-Gaussian properties of the state; the central negativity of transmitted odd-parity CS states remains the same. The composite channel can be

parametrized with

$$\begin{aligned} f_X &= \sqrt{\eta\eta'}\mathrm{e}^{-(\gamma+\gamma')} \,, \\ \sigma_X &= 2(1-\eta')\mathrm{e}^{-2\gamma_t'}V' + 2\eta'(1-\eta)\mathrm{e}^{-2(\gamma'+\gamma_t)}V \,, \\ f_P &= \sqrt{\eta\eta'}\mathrm{e}^{+(\gamma+\gamma')} \,, \\ \sigma_P &= 2(1-\eta')\mathrm{e}^{+2\gamma_t'}V' + 2\eta'(1-\eta)\mathrm{e}^{+2(\gamma'+\gamma_t)}V' \,, \end{aligned} \tag{4.23}$$

where the transmittances of the individual channels are given by η and η', the pre-squeezing rate is γ and the intermediate mid-squeezing rate is γ'. The asymmetric thermal noises are described by the pairs of parameters (γ_t, V) and (γ_t', V') in the spirit of (4.21).

The optimal intermediate squeezing rate exhibits remarkable behavior; this is demonstrated in Figure 4.5 for an odd-parity CS state with $\sqrt{2}\xi = 3$ transmitted through a composite channel (4.23). Without a loss of generality, the transmittances in both channels are set identically to keep the visualisation two dimensional. The plots show the best attainable negativity and the optimal pre-squeezing and mid-squeezing rates. We consider a number of asymmetric thermal environments. In Figure 4.5 (a) the dashed lines represent the attainable CN without any protective squeezing operations applied. The solid black line represents the best attainable CN when optimal pre-squeezing and mid-squeezing optimal pre-squeezing and mid-squeezing operations are applied to the CS state. The optimal CN depends only on the symmetric variance of the noise, rather than its asymmetry. The solid black line can be equally obtained for the same channel where both environments are symmetric. The solid black line in Figure 4.5 (b) represents the optimal pre-squeezing rate γ obtained when there is no asymmetry in either thermal environment, whereas the colored lines correspond to different asymmetries. We recognize that these rates are constantly shifted from the symmetric case, the offset equal to γ_t of the first channel. The colored bullets, obtained by adding the respective γ_t rates to the black line, are used to highlight this observation. Furthermore, in the third plot, Figure 4.5 (c), we observe that the optimal mid-squeezing rates γ' match the differences $\gamma' \equiv \gamma_t' - \gamma_t$ between the asymmetries of both environments.

We can interpret the pre-squeezing operation as a pair of virtual squeezing operations, as we did previously in the discussion of single channels, where the first virtual squeezer, with squeezing rate γ_0 realizes the actual protective pre-squeezing, whereas the second one reshapes the transmitted state to match the asymmetry of the environment in the first channel. The mid-squeezing operation can be also understood as a composition of two virtual squeezers, where the first squeezer transforms the transmitted state back to its original shape, while the second one reshapes it once again to match the asymmetry of the environment within the second channel. Interestingly, we can also obtain the optimal mid-squeezing rate γ' by maximizing the necessary condition (4.16).

Because the optimal mid-squeezing rate depends solely on the asymmetries of individual environments, the composite channel (4.23) can be reduced into a single elementary channel (4.21) with effective transmittance η_e and thermal noise variance V_e given by

$$\begin{aligned} \eta_e &= \eta\eta' \,, \\ V_e &= \frac{(1-\eta')V' + (1-\eta)\eta' V}{1-\eta\eta'} \,. \end{aligned} \tag{4.24}$$

This brings the entire analysis of composite channels back to the previous discussion of elementary channels. The protection of the CS state is facilitated **entirely** by the initial pre-squeezing operation and composite channels (4.23) can be substituted with equivalent elementary channels (4.21) parametrized by (4.24). Consequently, it is sufficient to only analyse noisy lossy channels with symmetric thermal environment.

With these conclusions in mind, we turn our attention back to the case of a single lossy channel with symmetric thermal noise and consider an alternative way of measuring the quality of the protection offered by the pre-squeezing operation.

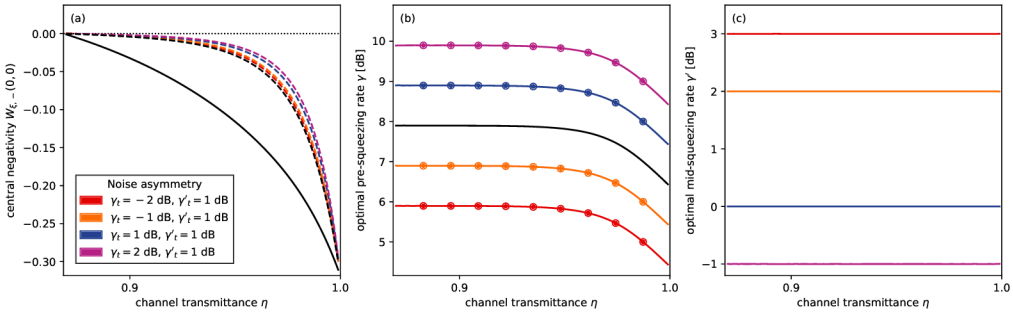

Figure 4.5. Adaptive squeezing protects odd-parity CS state ($\sqrt{2}\xi = 3$) from decoherence due to interaction with asymmetric thermal states with $V = 1$, $\gamma_t = \{-2, -1, 1, 2\}$ dB in the first channel and $V' = 2$, $\gamma'_t = 1$dB in the second channel. Solid black lines represent the cases where both thermal states are symmetric. **(a)** Attainable central negativity. Dashed lines represent the attainable negativity without any adaptation. After adaptation, a part of which effectively symmetrizes the environment, the best attainable negativities coincide. The solid black line determines this best attainable negativity. **(b)** Optimal pre-squeezing rate γ_t where the solid black line represents the optimal adaptation in the fundamental case when both thermals states of the environment are symmetric. Colored lines correspond to optimal pre-squeezing rates for asymmetric environments. These lines are shifted by a constant offset equal to γ_t. This fact is emphasized by the colored bullets that are obtained by adding γ_t to the fundamental pre-squeezing rate represented by the solid black line. **(c)** Optimal mid-squeezing rate γ'_t depends only on the asymmetry of the adjacent thermal states. Its value is determined by the difference $\gamma'_t - \gamma_t$.

Hilbert-Schmidt distance as a measure of state adaptation

The appeal of the central negativity of the odd-parity CS state stems from its availability as it can be measured directly or straightforwardly estimated. The presence of negativity within the Wigner function is also a necessary condition for the presence of quantum non-Gaussianity in the transmitted state [125, 127], contextuality [227] and advanced quantum protocols [228]. It also establishes a bound on the rest of the negative regions of Wigner function of the odd-parity CS state. However, because it is a local measure, it does not provide sufficient information about the other negative regions of the Wigner function of the transmitted CS state and its other quantum non-Gaussian aspects.

To complete the analysis, we use a directly measurable [221–224] Hilbert-Schmidt distance [225] between opposite-parity CS states transmitted through the channel (4.1). These two states form an orthonormal computational basis in quantum computation protocols [51, 52, 75, 129, 131, 133]. Their orthogonality can be measured with the Hilbert-Schmidt distance; it deteriorates as their quantum non-Gaussian features decay due to decoherence. While the distance itself does not directly indicate the presence of quantum non-Gaussian features, it provides indirect evidence of their preservation in both CS states and successfully complements the analysis based solely on central negativity as it takes both the even and odd parity CS states simultaneously into account.

In Figure 4.6 the Hilbert-Schmidt distance (4.18) is determined for a particular pair of CS states with $\sqrt{2}\xi = 3$ magnitudes transmitted through the elementary channel (4.1). It was established that it is optimal to adapt the state to the asymmetry of the environment; therefore, only symmetric thermal noise is considered. Cases with different noise variance $V \in \{0.5, 1.0, 1.5, 2.0\}$ are represented with different colors. The case of pure loss with $V = 0.5$ is displayed in red. The attainable Hilbert-Schmidt distance is presented in Figure 4.6 (a). Dashed lines represent the distance obtained without the protective pre-squeezing operation, whereas the solid lines correspond to optimally pre-squeezed CS states. The adaptation is certainly advantageous as the distance between the transmitted CS states is lower without the protective pre-

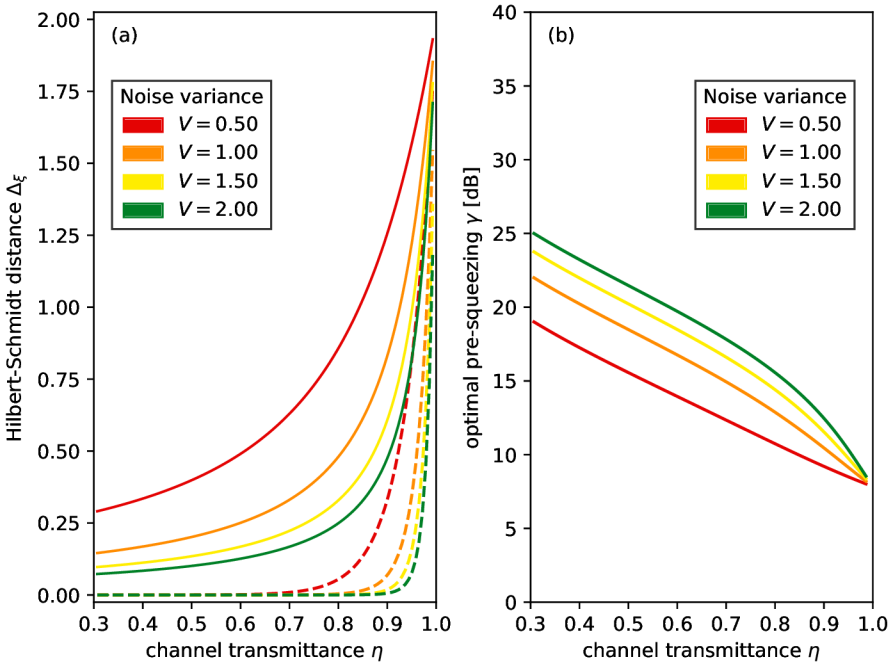

Figure 4.6. Hilbert-Schmidt distance Δ_ξ between opposite-parity CS states (with $\sqrt{2}\xi = 3$) transmitted through the channel (4.21) where the environment is a symmetric thermal noise with variance $V \in \{0.5, 1.0, 1.5, 2.0\}$. Colors indicate different thermal variance. **(a)** The attainable Hilbert-Schmidt distance without protective pre-squeezing is represented with dashed lines, whereas the solid lines correspond to optimally pre-squeezed CS states. We can surmise that pre-squeezing certainly offers advantage as the attainable distance between the transmitted states is greater. **(b)** The optimal pre-squeezing rate used to protect the CS states before their transmission.

squeezing. The optimal pre-squeezing rates, presented in Figure 4.6 (b), do not depend trivially on the amount of the noise and must be determined numerically on a case by case basis.

Suitable pre-squeezing operation can increase the distance of the states even in the cases when it is practically zero before the correction. However, unlike in the case of central negativity, where the optimal pre-squeezing depended on the channel transmission only for its high values, here the optimal pre-squeezing changes more or less linearly with the channel transmittance. This shows that there is no single universal approach towards protecting the states as their different features require different methods of protection.

C Conclusions

The loss and noise of bosonic channels deteriorating the non-Gaussian properties of quantum states is one of the main bottlenecks for scalable quantum computation with optical fields. While the noise can be, potentially, compensated by error correction [50, 52, 131, 136–138], this is costly and should be attempted only after other, more feasible avenues, are explored first. We presented one such mitigation strategy for superposed coherent states based only on feasible Gaussian operations. This operation can be realized either actively, by directly performing the Gaussian operation [229], or it can be incorporated into the state preparation stage of the protocols [109].

It can be straightforwardly extended to mitigate decoherence of the continuous variable component in quantum systems with hybrid entanglement between discrete qubits and continuous-

variable CS states [110, 111, 140, 230].

While the method is most valuable for optical fields propagating through bosonic channels, the concept is general and can be straightforwardly employed to preserve the non-Gaussian property of quantum states in other bosonic systems, such as microwave cavities, spin systems, trapped ions, or optomechanics [231–238].

Chapter 5

Faster Computation of Fock Capability of non-Gaussian Resources

This chapter summarizes the upcoming article *"Exponential improvement in the computational complexity of Fock capability of non-Gaussian Resources"* [239].

Single photon states serve an important role across many quantum disciplines, including quantum information theory [26], quantum state engineering [240–242], and quantum key distribution [243]. While their applications are abundant in theory, practical and reliable sources of single photons are scarce due to many challenges in their experimental realization. Even under ideal conditions, the presently best available single photon sources suffer from loss, thus producing states with vacuum contributions present. It is also not uncommon that the available single photon sources exhibit contributions of higher orders.

Single photons, whether ideal or not, can interfere within elaborate optical networks. These intricate breeding protocols can be theoretically employed in production of arbitrarily complex quantum states [240–242]. The attainable complexity is affected by the quality of the individual single photon states inserted into the breeding protocol. Consequently, the quality of resource states can be quantified with the attainable complexity within a specific protocol for quantum state synthesis.

The procedure proposed in [244, 245] takes an advantage of a protocol where identical copies of the resource state propagate through a perfectly balanced multi-port interferometric network as illustrated in Figure 5.1. The resulting state is post-selected on the event where all the interfering photons bunch within a particular output port of the interferometer. The procedure treats the resource states as completely incoherent mixtures. A single-photon resource state is then said to have a particular **Fock capability** C if the Wigner function of the resulting state, obtained by combining C independent incoherent copies of the resource, possesses at least as many negative annuli [244]. While the proposed approach appeared promising, its applications to both higher-dimensional resource states and greater numbers of copies were severely hindered by its exponential computational complexity [244].

An algorithm offering an exponential improvement in computational complexity over the original technique is described in the following sections and some of its applications that were previously infeasible are discussed.

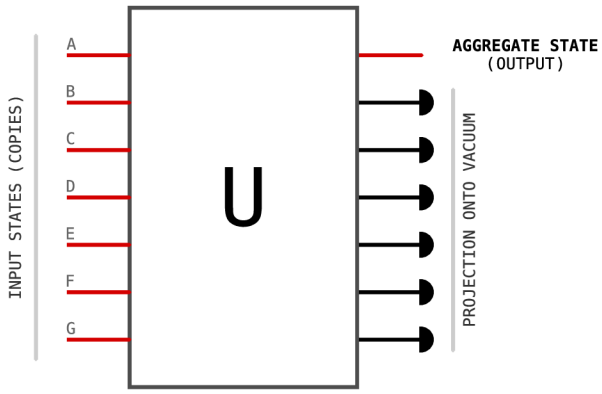

Figure 5.1. Multiple independent copies, labeled with A to G in the picture, of an incoherent quantum state propagate through a passive perfectly-balanced multi-port interferometric network [244]. The field operators $\hat{a}_i$ of individual modes undergo a passive unitary transformation $\hat{a}_i \mapsto \sum_j U_{ij}\hat{a}_j$ with matrix $|U_{ij}|^2 = C^{-1}$ where C represents the number of input states. The unitary transformation can be realized with suitably oriented beam splitters [246]. The interfered modes are measured with the exception of the output mode. Simultaneous detection of zero photons within all the measured modes heralds a formation of the desired aggregate state (5.1) where all photons bunched into the output mode.

A Exponential improvement in computational complexity

An incoherent state of at most $d-1$ photons is completely characterized by the d coefficients determining its diagonal density matrix in the Fock representation. Multiple independent incoherent states can be combined using a balanced beam splitter network as illustrated in Figure 5.1. A state with up to $C(d-1)$ photons can be potentially produced by interfering C independent states in the unlikely event when all the photons bunch together and emerge from one particular port of the optical network. The resulting state is also fully characterized by a diagonal density matrix in Fock representation [244] as the interactions in the optical network can not introduce non-classicality between the individual independent incoherent input states. The output non-normalized density matrix is obtained [244] as

$$\tilde{\varrho} = \sum_{k=0}^{C(d-1)} f_k\,|k\rangle\langle k| = \underbrace{\sum_{m_0=0}^{d-1}\frac{\sigma_{m_0}^{(0)}}{m_0!}}_{\text{1st state}}\underbrace{\sum_{m_1=0}^{d-1}\frac{\sigma_{m_1}^{(1)}}{m_1!}}_{\text{2nd state}}\cdots\underbrace{\sum_{m_{C-1}=0}^{d-1}\frac{\sigma_{m_{C-1}}^{(C-1)}}{m_{C-1}!}}_{C\text{th state}}\tau(s)\,|s\rangle\langle s| \tag{5.1}$$
$$\text{where}\quad \tau(s) \coloneqq \frac{s!}{C^s}\quad\text{and}\quad s \coloneqq \sum_{k=0}^{C-1} m_k\,.$$

The symbol $\sigma_m^{(k)}$ in (5.1) refers to the mth diagonal component of the kth input state. At first glance it is necessary to evaluate every $\sigma(\mathbf{m}) \coloneqq \sigma_{m_0}^{(0)}\sigma_{m_1}^{(1)}\cdots\sigma_{m_{C-1}}^{(C-1)}$ coefficient product for every multi-index combination $\mathbf{m} \coloneqq (m_0, m_1, m_2, \dots)$ of individual state indices.

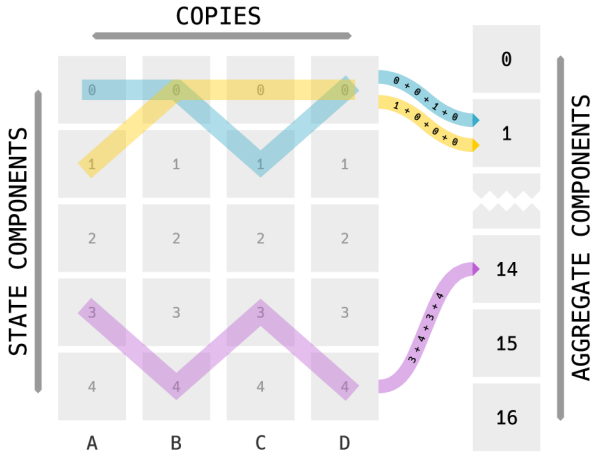

Figure 5.2. Computation of the aggregate density matrix (5.1) illustrated for the case of four copies of an incoherent state spanning the first five Fock states. Columns represent individual states, whereas rows correspond to the diagonal components of their density matrices. The resulting state is constructed from individual contributions, obtained by taking products of every possible combination of state components. The products are added to the appropriate element of the aggregate state, determined by summing up the positions of individual components comprising each product. Multiple products can contribute to the same aggregate element. The combinations of components can be visualised as paths (yellow, blue and purple) through the matrix made of the input states; three distinct paths are highlighted in the picture, along with the process (colored arrows) of determining the correct element of the aggregate state.

Computation process of the resulting aggregate density matrix (5.1) is illustrated in Figure 5.2 for the case of four copies of an incoherent state spanning the first five Fock states. Columns represent individual states, whereas rows correspond to the diagonal components of their density matrices. The resulting state is constructed from individual contributions, obtained by taking products of every possible combination of state components. The products are added to the appropriate element of the aggregate state, determined by summing up the positions of individual components comprising each product. Multiple products can contribute to the same element of the aggregate state, their values are summed up. The combinations of components can be visualised as paths through the matrix made of the input states; three distinct paths are highlighted in the picture, along with the process of determining the correct element of the aggregate state.

In total, this amounts to evaluation of $O(d^C)$ possible combinations, suggesting the computation might belong to some ostensibly non-polynomial complexity class [244]. Turns out this assessment is incorrect and the problem actually belongs to the realm of polynomial complexity.

The sequence of summations in (5.1) can be arbitrarily regrouped and evaluated, as illustrated within Figure 5.3. For example, the first two sums may be separated from the rest, the respective d^2 combinations of coefficients evaluated and the pair of sums replaced with an effective state comprising at most $2(d-1)$ photons. The next summation can be then separated from the remaining $C-2$ sums. The same procedure is then followed, that is, the $2(d-1)d$ products with the previously determined effective state are computed. This way, another effective state comprising at most $3(d-1)$ photons is determined. This procedure is repeated for the rest of the sequence until it is reduced into the final effective state — the long anticipated result.

The number of photons within each intermediate effective state does not exceed $(d-1)C$. The number of products computed within each iteration is limited by $d(d-1)C$. To reduce the entire sequence $C-1$ iterations of the procedure are needed. Consequently the asymptotic computational complexity of the procedure scales with $O(d^2C^2)$ in terms of computed products. In conclusion, the complexity of the computation is **quadratic** both in the number of input states C and the initial dimension d. ■

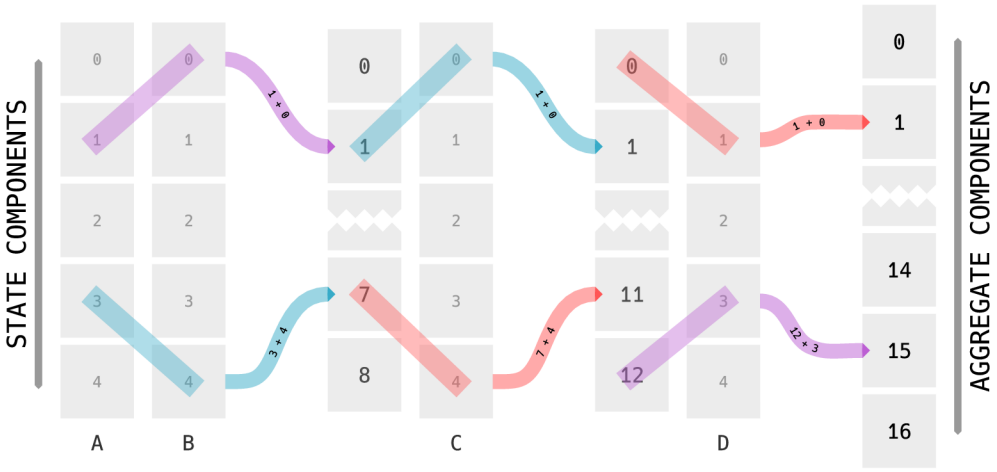

Figure 5.3. Iterative computation of the aggregate density matrix (5.1) illustrated for the case of four copies of an incoherent state spanning the first five Fock states. The computation process is divided into blocks and realized iteratively. In the first iteration, the products of the first two copies, A and B, are computed and consequently aggregated. In the second iteration, the products of the third copy, labeled with C, and the previous aggregate state are determined and distributed accordingly. In the final iteration, the same process is repeated with the last state.

Our algorithm can be immediately applied in analysis of realistic sources of single photons exhibiting potentially undesirable contributions of higher orders. The exponential improvement in computational complexity permits optimization of the tunable experimental parameters.

B Computational complexity of the whole procedure

The calculation of the aggregate matrix (5.1) is only the first step in the process of calculating the measure of capability [244]. The essence of the measure lies in counting the negative annuli in the Wigner function of the aggregate state [244]. Because the aggregate density matrix (5.1) is diagonal, its Wigner function can be expressed as a weighted sum of individual Wigner functions of the constituent Fock states,

$$W(x,p) \approx \sum_{k=0} f_k W_k(x,p) \ , \tag{5.2}$$

where the $\approx$ symbol emphasises that the Wigner function is not normalized as f_k from (5.1) are not normalized either. The constituent Wigner functions [244, 247]

$$W_k(x,p) \approx (-1)^k \exp(-x^2-p^2) L_k(x^2+p^2) \ . \tag{5.3}$$

are not normalized either. The number of negative annuli in the Wigner function is not affected by the normalization coefficients, nor is it affected by any other positive factor, such as $\exp(-x^2-p^2)$ shared among the individual components. The relevant parts of the Wigner function (5.2) can be simplified into a sum of Laguerre polynomials

$$\sum_{k=0} l_k L_k(z) \quad \text{where} \quad l_k \coloneqq (-1)^k f_k \tag{5.4}$$

with the coefficients l_k derived from the aggregate matrix (5.1). The number of negative annuli can be then determined by counting the positive real roots of the polynomial [244].

Roots of the polynomial (5.4) can be found numerically by determining the eigenvalues of its companion matrix [248]. Complexity of eigenvalue decomposition scales cubically with the

dimension of the decomposed matrix [249, Table 3.13]. The root finding routine thus scales **cubically** with the number of elements in the Laguerre series. Because the dimension of the aggregate matrix scales with $O(dC)$, the problem of finding the roots grows with $O(d^3C^3)$. This actually majorizes the quadratic complexity of computing the aggregate density matrix (5.1). ■

The asymptotic computational complexity of the quantification procedure used to determine the Fock capability [244] measure is polynomial. The complexity $O(d^3C^3)$ scales **cubically** with the number of copies C and the dimension d of the resource state.

C Application to realistic sources of single photons

It is possible to synthesize photonic Fock states by using a two mode squeezed vacuum state and a photon number resolving detector [97, 98, 178, 184]. One of the entangled modes is measured, thus projecting the other mode onto the resolved Fock state. Its successful creation is heralded by a satisfactory detection outcome. The state is discarded and the procedure is repeated upon unsatisfactory detection events. The outlined protocol builds on a few assumptions about the quality of the resources it relies on, assuming a perfect two mode squeezed vacuum state, lossless transmission and an ideal photon number resolving detector are used. The experimental implementation is plagued by loss at each step of the procedure. Detectors with limited quantum efficiency can be also modeled with loss. The resulting non-normalized marginal state is given by

$$\hat{\varrho} \approx \sum_{i=0}^{\infty}\sum_{j=0}^{\infty} \lambda^i \lambda^j \left(\sum_{k=0}^{\infty} \langle m|\, \hat{M}_k(\zeta_1)\, |i\rangle\langle j|\, \hat{M}_k^\dagger(\zeta_1)\, |m\rangle\right)\left(\sum_{k=0}^{\infty} \hat{M}_k(\zeta_2)\, |i\rangle\langle j|\, \hat{M}_k^\dagger(\zeta_2)\right) , \tag{5.5}$$

where m identifies the detected Fock state, $\lambda = \tanh(r)$ characterizes the two mode squeezed state with initial squeezing r, and the Kraus operators $\hat{M}_k(\zeta)$ describe the transmission loss with

$$\hat{M}_k(\zeta) = \sqrt{\frac{(1-\zeta)^k}{k!}}\sqrt{\zeta}^{\hat{n}}\hat{a}^k \tag{5.6}$$

where ζ gives the intensity transmittance of the lossy channel [122]. In the case of (5.5), the parameter ζ_1 corresponds to loss in the first mode, called the heralding mode, whereas ζ_2 identifies the loss affecting the mode with the prepared state. The equation (5.5) for the resulting density matrix of the prepared state can be simplified. The matrix is diagonal in the Fock basis with elements

$$\langle k|\varrho|k\rangle = \frac{[1-\lambda^2(1-\zeta_1)]^{m+1}}{[\lambda^2(1-\zeta_1)]^m}\left(\frac{\zeta_2}{1-\zeta_2}\right)^k H(k,m,x) , \tag{5.7}$$

where the substitution $x \coloneqq \lambda^2(1-\zeta_1)(1-\zeta_2)$ is used in $H(k,m,x)$, defined as

$$H(k,m,x) \coloneqq \begin{cases} \sum_{l=n}^{\infty}\binom{l}{m}\binom{l}{k}x^l & k \le m , \\ \sum_{l=k}^{\infty}\binom{l}{m}\binom{l}{k}x^l & k > m . \end{cases} \tag{5.8}$$

The series in (5.8) converge since $\lambda^2(1-\zeta_1)(1-\zeta_2) \le 1$. The formula can be expressed in terms of hypergeometric functions [200] as

$$H(k,m|x) \equiv \begin{cases} x^m\binom{m}{k}{}_2F_1(1+m,1+m,1+m-k,x) & k \le m , \\ x^k\binom{k}{m}{}_2F_1(1+k,1+k,1+k-m,x) & k > m . \end{cases} \tag{5.9}$$

Capabilities of realistic single-photon states

Detection of a favorable outcome heralds a successful preparation of a quantum state parametrized by the initial squeezing rate and the two transmission efficiencies. The preparation procedure can be simulated numerically for different parameters and the Fock capability of the prepared state, described by (5.7), can be efficiently determined with the improved algorithm.

The coefficients in the resulting density matrix of the aggregate state may be negligible — often close to zero but not exactly zero. The number of terms in the Laguerre series (5.4), and therefore the practical complexity of finding the roots, can be significantly reduced by pruning all the elements of the density matrix below some threshold ϵ. The aggregate matrix itself remains mostly unaffected. Its perturbation, calculated in terms of fidelity, is the sum of the trimmed elements and is bound from above by ϵw with w indicating the number of elements removed. In practice the computation of the capability became appreciably faster and even the numerical stability of the computed capability improved.

A collection of realistic states was obtained by simulating the procedure for different initial squeezing rates r, limited by 10 dB, and transmission efficiencies ζ_1 and ζ_2. Elements $\langle k|\varrho|k\rangle$ with $0 \leq k < 20$ were utilized to compute the capability of each state with $2 \leq C \leq 11$ identical copies. Previously, it was impossible to consider this number of elements and copies with the original algorithm; it would have taken $O(d^C)$ multiplications to obtain the final density matrix, whereas the quadratic algorithm only needs up to $O(d^2C^2)$ operations.

The information obtained this way can be interpreted in a multitude of ways. In the upper row of Figure 5.4 the simulated states are binned by their $\langle 0|\varrho|0\rangle$ and $\langle 1|\varrho|1\rangle$ elements and the minimal attainable capability is found for each bin. The capability is presented in the context of single photon sources with the two principal elements — the vacuum component and the single photon contribution. The two probabilities do not necessarily sum up to unity as realistic states comprise higher-ordered components. Consequently, the observed capability may increase as the distribution shifts towards higher-ordered elements, such as the two photon contribution.

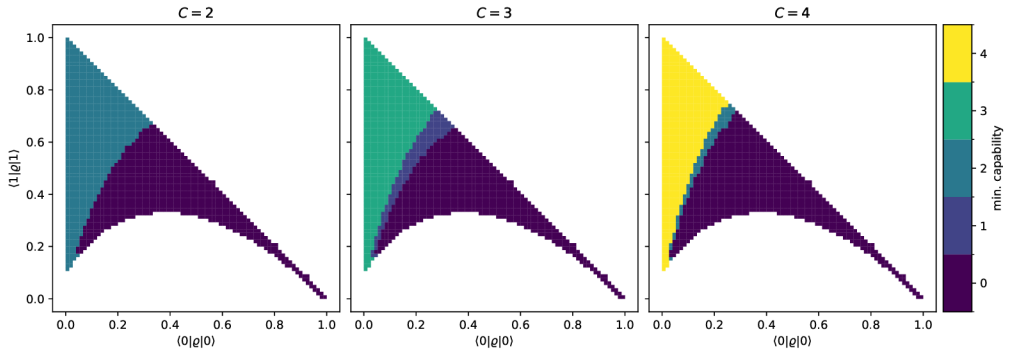

Figure 5.4. Capability of single photon states produced by a realistic preparation circuit. States produced by varying the initial squeezing rate and transmission efficiencies in the heralding and the signal modes are binned by their $\langle 0|\varrho|0\rangle$ and $\langle 1|\varrho|1\rangle$ components. Their capability is computed for $C = 2, 3, 4$ copies and the minimal capability attainable in each bin is presented.

Another way of looking at the data is presented in Figure 5.5 where the highest attainable capability $F^\star$ for $C = 2, 3, 4$ copies is found by maximizing over the squeezing rate for each combination of transmission efficiency ζ_1 and ζ_2. The observed behavior, where best attainable capability $F^\star$ is not affected by the loss ζ_1 incurred in the heralding mode, can be explained by considering the effects of loss in each mode. Without loss in either mode the prepared state is exactly the state measured. Once the heralding mode is subjected to loss ($\zeta_1 < 1$), the prepared states becomes a mixture of states $|n \geq m\rangle$. The potential capability of these mixed states can only increase compared to the states produced by the lossless protocol as the maximal order s

of the aggregate state in (5.1) increases. The effects of loss ($\zeta_2 < 1$) on the prepared state are more destructive. The loss introduces $|n < m\rangle$ states into the mixture and makes them more pronounced in combination with the heralding loss; these can only decrease the observed capability of the prepared state by contributing to lower-ordered aggregate states in (5.1) and consequently suppressing elements of higher order in the collective multi-copy state.

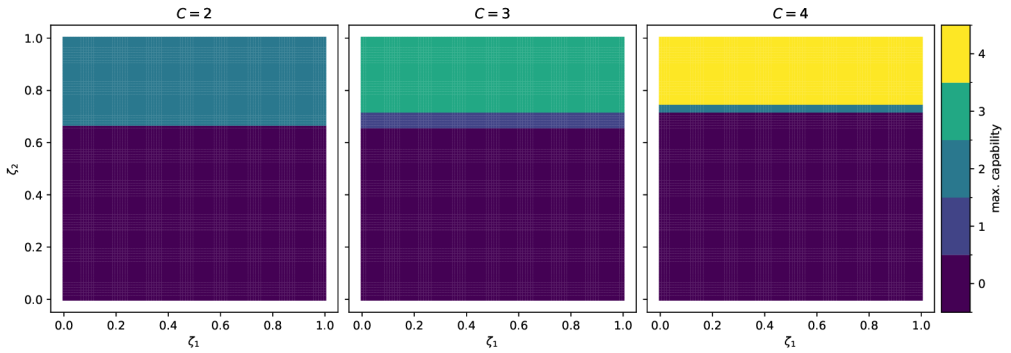

Figure 5.5. Capability of single photon states produced by a realistic preparation circuit. The best attainable capabilities of the states produced with varying transmission efficiencies in the heralding (ζ_1) and the signal (ζ_2) modes are found by maximizing over the initial squeezing rate.

D Conclusions

The Fock state capability of a state is determined as the number of negative annuli in the Wigner function of an aggregate state obtained by interfering multiple copies of the state on a perfectly balanced multi-port interferometer [244]. The exponential improvement of its computational complexity makes it possible to explore physically relevant scenarios; for example by simulating a realistic state preparation circuit and analyzing the complex effects of loss on the Fock capability of prepared states. The results presented in this chapter can be used in designing feasible experimental demonstration of the measure.

We found that the computational complexity of the calculation of the aggregate state scales quadratically with the product dC of the number of copies C considered and dimension d of the initial state, whereas the process of counting the negative annuli, based on finding the positive real roots of a Laguerre series, scales cubically. The computational complexity of the measure therefore scales with $O(d^3C^3)$, which is a major improvement over the original exponential scaling $O(d^C)$.

Furthermore, because the improvement lies in the computation of the aggregate state, the basis of the method can be employed with other qualitative measures, for example by considering the hierarchical criteria for genuine Fock states [161].

Chapter 6

Paving the Way Towards Four Photon Optical States

This chapter summarizes the upcoming article *"Paving the way towards four photon optical states"* [250].

It is often proclaimed that the quantum advantage and quantum supremacy are lurking somewhere just beyond the horizon. While that might be true, perhaps it would be best to consider why are things seemingly as trivial as the preparation of a four photon quantum state with reasonable quality still out of reach.

A measurement-based method for preparation of individual photonic states of light [97, 98, 178] is discussed in the first section of this chapter. The mathematical model of the procedure takes loss into account, both in the construction of the state in during its characterization. The resulting states are certified using hierarchical criteria [161] in the second section by evaluating the statistical behavior of the model under realistic experimental conditions. Figures presented in this section can be used to determine the minimal requirements on the efficiency of the optical components, such as squeezing and detection, in experimental realizations targeting states of two, three, and four photons.

A Cooking up states of travelling light

Photonic Fock states can be conditionally prepared by using a two mode squeezed vacuum state and a photon number resolving detector [97, 98, 178, 184]. One of the entangled modes is measured, thus projecting the other mode onto the resolved Fock state. This procedure is repeated until a satisfactory detection outcome is observed; at that point the target state is successfully prepared. The outlined protocol assumes a perfectly squeezed state, lossless transmission and an ideal detector. Some of the adverse effects of realistic inefficiencies can be effectively accounted for by considering lossy transmission of both modes. The resulting non-normalized marginal state is given by

$$\hat{\varrho} \approx \sum_{i=0}^{\infty}\sum_{j=0}^{\infty} \lambda^i \lambda^j \left(\sum_{k=0}^{\infty} \langle m| \hat{M}_k(\zeta_1) |i\rangle\langle j| \hat{M}_k^\dagger(\zeta_1) |m\rangle\right) \left(\sum_{k=0}^{\infty} \hat{M}_k(\zeta_2) |i\rangle\langle j| \hat{M}_k^\dagger(\zeta_2)\right) , \tag{6.1}$$

where m identifies the detected Fock state, $\lambda = \tanh(r)$ characterizes the two mode squeezed state with initial squeezing r, and the Kraus operators $\hat{M}_k(\zeta)$ describe the transmission loss with

$$\hat{M}_k(\zeta) = \sqrt{\frac{(1-\zeta)^k}{k!}} \sqrt{\zeta}^{\hat{n}} \hat{a}^k \tag{6.2}$$

where ζ gives the intensity transmittance of the lossy channel [122]. In the case of (6.1), the parameter ζ_1 corresponds to loss in the first mode, called the heralding mode, whereas ζ_2 identifies the loss affecting the mode with the prepared state.

The probability of successful preparation, that is, the probability of detecting m photons in the heralding mode, can be obtained analytically as

$$P_m = (1-\lambda^2)\frac{(\lambda^2\zeta_1)^m}{[1-\lambda^2(1-\zeta_1)]^{m+1}} \,. \tag{6.3}$$

The equation (6.1) for the resulting density matrix of the prepared state can be simplified. The is diagonal in the Fock basis; its properly normalized elements are obtained as

$$\langle k|\varrho|k\rangle = \frac{[1-\lambda^2(1-\zeta_1)]^{m+1}}{[\lambda^2(1-\zeta_1)]^m}\left(\frac{\zeta_2}{1-\zeta_2}\right)^k H(k,m,x) \,, \tag{6.4}$$

where the substitution $x \coloneqq \lambda^2(1-\zeta_1)(1-\zeta_2)$ is used in $H(k,m,x)$ defined as

$$H(k,m,x) \coloneqq \begin{cases} \sum_{l=n}^{\infty}\binom{l}{m}\binom{l}{k}x^l & k \le m \,, \\ \sum_{l=k}^{\infty}\binom{l}{m}\binom{l}{k}x^l & k > m \,. \end{cases} \tag{6.5}$$

The series in (6.5) converge since $\lambda^2(1-\zeta_1)(1-\zeta_2) \le 1$. The formula can be alternatively expressed in terms of hypergeometric functions [200] as

$$H(k,m|x) \equiv \begin{cases} x^m\binom{m}{k}{}_2F_1(1+m,1+m,1+m-k,x) & k \le m \,, \\ x^k\binom{k}{m}{}_2F_1(1+k,1+k,1+k-m,x) & k > m \,. \end{cases} \tag{6.6}$$

Using this form in numerical computation offers an advantage. It is possible to avoid the common pitfalls of dealing with binomial coefficients and infinite sums because the hypergeometric function is readily available through the `scipy.special.hyp2f1` interface [251].

B Certification of prepared states

The relation (6.4) provides the diagonal elements of the conditionally prepared quantum state; it is a function of the initial squeezing rate, the losses incurred in both modes and the post-selection imposed on the measurement outcome. The main experimental challenges are due to the ever present loss. The tolerable amount of loss in the circuit capable of preparing a certifiable genuine m-photon state can be determined with numerical simulation of the experiment. The preparation circuit is simulated for different amounts of loss in both modes, varying initial squeezing rates and target states $m \le 10$. Beside the probability of success P_m, the diagonal elements of the density matrix (6.4) are computed for $k \le 20$. Detection events in the simulated experiments are drawn as random samples from a multinomial distribution bootstrapped with the diagonal elements of the computed density matrix. Assuming the budget of 10^8 repetitions in a single experimental run, $\lfloor 10^8 \times P_m \rfloor$ samples are drawn from the distribution and used to estimate the experimental probability distribution $\overline{p}_k \approx \langle k|\varrho|k\rangle$. This process is repeated to obtain 100 independent experimental runs for the subsequent statistical analysis.

Certification of genuine m-photon states is done with the bespoke hierarchical criteria [161] based on probabilities of Fock state contributions in candidate states. The aggregate variables,

$$y_m = \overline{p}_m \quad \text{and} \quad x_m = 1 - \sum_{k=0}^{m}\overline{p}_k \,, \tag{6.7}$$

are computed from the estimated experimental probabilities $\overline{p}_k$ obtained in each simulated run of the experiment. Their expectation values and their standard deviations are then used to certify the quantum state resulting from the simulation with the particular choice of (m, ζ_1, ζ_2, r) parameters; the state is considered to be certifiably genuine m-photon state if the expectation values lie at least three standard deviations away from the Lachman curve $\mathcal{L}_m$. The operating principle of the certification procedure is illustrated in Figure 6.1.

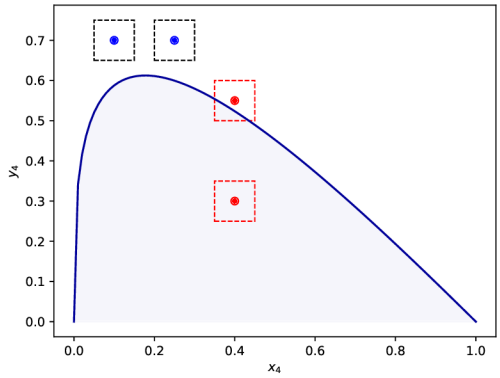

Figure 6.1. Illustration of the certification procedure. The blue line represents the Lachman curve $\mathcal{L}_4$. States with $y_4 > \mathcal{L}_4(x_4)$ are genuine Fock states $|4\rangle$. Four example states are depicted in the figure. The bullet points represent their expectation values $\langle x_4 \rangle$ and $\langle y_4 \rangle$ obtained by simulating the experiment. The dashed boxes would normally span three standard deviations in each dimension. Size of the pictured boxes are extremely exaggerated for legibility. States marked with red bullets failed the certification as they lie either under the Lachman curve or their respective boxes intersect the curve. States marked with blue bullets are certifiably genuine 4-photon states according to the criteria; their boxes are well above the curve and do not intersect the curve.

In each dataset related to the tuple (m, ζ_1, ζ_2) of parameters the maximal probability of success is found with respect to the squeezing rate $r \leq 10\,\mathrm{dB}$. Both the maximal probability $P_m^\star$ and the respective optimal squeezing rate $r^\star$ are visualised in a grid as functions of $(1-\zeta_1, 1-\zeta_2)$ for each target state m. In addition, to present only statistically significant results in the visualisation, grid cells where the probability of success lies below a reasonable threshold set to 10^{-5}, which guarantees at least 1000 successful realizations of the state within each experimental run, were blanked out.

The achievable success rate in preparation and subsequent certification of genuine m-photon states is presented in Figure 6.2. Each column pertains to the particular target state $m = 2, 3, 4$. The maximal probabilities of success $P_m^\star(1-\zeta_1, 1-\zeta_2)$ are presented in the top row, whereas the corresponding optimal squeezing rates $r^\star(1-\zeta_1, 1-\zeta_2)$ are provided in the bottom row. To reflect on the experimental limitations, the optimization is constrained to squeezing rates limited by 10 dB. The figure also effectively shows the amount of loss that can be tolerated in the experiment.

In the case of the 2-photonic state the tolerable loss exceeds 40% in both modes. The probability of success ranges from roughly 10% to 0.1%. The higher the loss, the lower the optimal squeezing rate. The tolerable loss is much lower for the state with 3 photons. The maximal probabilities of success are also reduced. If the state suffers 40% loss during preparation, it can only tolerate at most 20% loss in its characterization. Higher loss leads to success rates lower than the 10^{-5} threshold set earlier; the information obtained in the blanked out region is assumed to be unreliable. Finally, the conditions for the 4 photon state are even less favorable; while it is still possible to tolerate up to 40% loss during preparation, the limit on $1-\zeta_2$ is much more stringent, only about 10% loss is permitted.

The two mode squeezed vacuum state is assumed to be ideal. The photon number resolving

detectors are also presumed to be perfect with unit quantum efficiency. In realistic experiments these assumptions are never true, however, both the inefficiencies in detection and preparation of the squeezed state can be modeled with loss. Consequently the presented results cover these imperfect cases as well since any loss in the initial squeezed state generation are subsumed in the detection losses.

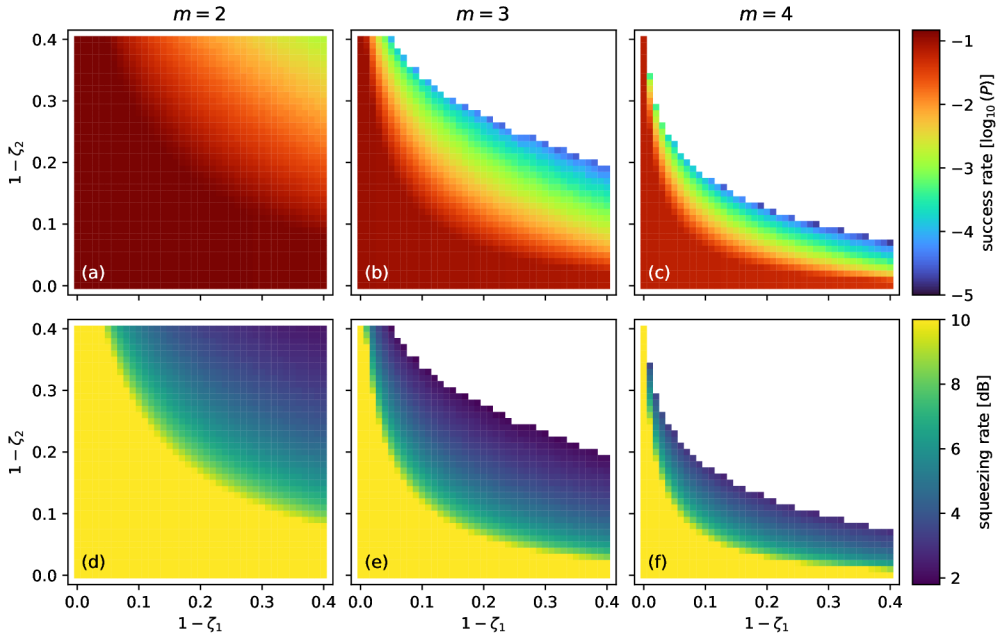

Figure 6.2. The tolerable loss in preparation and subsequent certification of genuine m-photon states. Results for target states $m = 2, 3, 4$ are shown in columns. The maximal probabilities $P_m^\star$ of successful preparation of the certifiable target state, given the particular combination of loss $1 - \zeta_1$ incurred during preparation and the loss $1 - \zeta_2$ affecting the certification, are presented using a logarithmic scale in the top row. The optimization is constrained to squeezing rates limited by 10 dB. The respective optimal squeezing rates $r^\star$ are provided in the bottom row.

C Conclusions

The results presented in this chapter offer an insight into feasible experimental preparation of certifiable genuine m-photon states for $m = 2, 3, 4$. While preparation of quantum states of travelling light of up to three photons has already seen its experimental realization [97], the construction of a 4-photon state of travelling light still remains an open problem that will perhaps benefit from the analysis.

Chapter 7

Witnessing Genuine Multi-Partite Entanglement

This chapter briefly introduces the concept of genuine multi-partite entanglement and summarizes the contribution to the articles *"Verifying genuine multipartite entanglement of the whole from its separable parts"* [252], *"Certifying emergent genuine multipartite entanglement with a partially blind witness"* [253], resulting in the subsequent development of open-source software libraries `witnessmess` [254] and `nomadlad` [255].

The roots of quantum entanglement reach deep into the history of quantum mechanics. The baffling phenomenon was first described as a paradox and an evidence of potential shortcomings of then controversial quantum theory [256]. In the following decades it came to be recognized as a resource in a variety of applications, including diverse areas such as quantum information processing [57, 61, 257–259], quantum communication [259–264] and quantum key distribution [259, 265–270].

A Witnessing Genuine Multi-Partite Entanglement

Quantum entanglement is one of the fundamental properties that distinguish the quantum world from the classical one. A general state $\hat{\varrho}_{AB}$ of a quantum system comprising two parts, A and B, is **separable** if and only if its state can be expressed as a statistical mixture of product states of its constituent parts. In particular, the state $\hat{\varrho}_{AB}$ is separable if and only if

$$\hat{\varrho}_{AB} = \sum_i p_i \hat{\varrho}_A \otimes \hat{\varrho}_B \,, \tag{7.1}$$

where $p_i \geq 0$ and $\sum_i p_i = 1$. It is **entangled** otherwise [259]. The concept of separability and entanglement can be readily extended to the case of multi-partite quantum systems despite their significantly more convoluted structure [259].

To illustrate these differences we consider a tripartite quantum system — comprising A, B, and C components — and assume its state is pure for the sake of clarity. There are several distinct arrangements possible. It can be fully separable, that is, $|\psi\rangle_{ABC} = |\varphi\rangle_A \otimes |\xi\rangle_B \otimes |\zeta\rangle_C$. It can be **separable** with respect to a particular grouping of its constituent parts; the three options are $|\varphi\rangle_A \otimes |\xi\rangle_{BC}$, $|\varphi\rangle_{AB} \otimes |\xi\rangle_C$, and $|\varphi\rangle_{AC} \otimes |\xi\rangle_B$. In each case, two parts of the system can be entangled, while the remaining part is separable from the other two. A fully separable quantum system can be seen as biseparable because its constituents can be grouped together. A **genuine tripartite entangled** pure state is neither fully separable nor biseparable with respect to any grouping [259, 271].

This concept can be straightforwardly extended to mixed states. A general mixed tripartite state $\hat{\varrho}_{ABC}$ is genuinely tripartite entangled if and only if

$$\begin{aligned}\hat{\varrho}_{ABC} \neq \lambda_A \sum_i p_i^{A|BC} \hat{\varrho}_i^A \otimes \hat{\varrho}_i^{BC} + \\ \lambda_B \sum_i p_i^{B|AC} \hat{\varrho}_i^B \otimes \hat{\varrho}_i^{AC} + \\ \lambda_C \sum_i p_i^{C|AB} \hat{\varrho}_i^C \otimes \hat{\varrho}_i^{AB}\end{aligned} \tag{7.2}$$

where $\lambda_A, \lambda_B, \lambda_C \geq 0$, and $\sum_i p_i^\tau = 1$ with $p_i^\tau \geq 0$ for $\tau \in \{A|BC, B|AC, C|AB\}$, that is, if it cannot be expressed as a statistical mixture of convex combinations of biseparable mixed states [259, 271, 272].

A possible hierarchy of separability classes naturally arises in general multi-partite scenarios; a quantum system can be k-separable with respect to its division into k non-empty subsets. Similarly, a fully k-separable system is necessarily k-separable with respect to every possible division into k non-empty subsets. Higher orders of the hierarchy induce lower ones. Separable subsets of the system can be arbitrarily merged together; k-separability with respect to some division then implies l-separability with $l < k$. The inductive behavior of the hierarchy has a direct application. Any 2-inseparable quantum system is necessarily k-inseparable for every $k \geq 2$. The definition of a genuine multi-partite entanglement (GME) then follows intuitively; a quantum system is **genuinely multi-partite entangled** if and only if it can not be expressed as a convex mixture of biseparable states with respect to any possible division into two distinct subsets of the system [259, 272].

The formal definition of entanglement is one thing, its practical detection is an entirely different matter. One possible approach employs directly measurable operators to **witness** the entanglement of the quantum system [259]. These special operators, called **entanglement witnesses**, give a necessary and sufficient condition of entanglement by the virtue of the Hahn-Banach theorem [259].

Witnesses of GME can be constructed through semi-definite programming (SDP) [273] by relaxing the problem and considering positive partially-transposed (PPT) mixtures instead of the biseparable mixtures used in the definition of GME [271]. The task of finding the witness then becomes

$$\begin{aligned}&\underset{\hat{W}\geq 0}{\text{minimize}} \ \operatorname{tr}(\hat{W}\hat{\varrho}) \\ &\text{subject to} \ \operatorname{tr}(\hat{W}) = 1 \\ &\hat{W} = \hat{P}_M + \hat{Q}_M^{T(M)} \quad \text{where} \quad \hat{Q}_M \geq 0, \hat{P}_M \geq 0 \ .\end{aligned} \tag{7.3}$$

Witnesses satisfying the final condition are **fully decomposable** with respect to all bi-partitions M of the multi-partite quantum system [271]. The primary benefit of this approach lies in the method of witness construction; the constructed operator is guaranteed to be globally optimal for the given state $\hat{\varrho}$. The glaring disadvantage, on the other hand, is that some genuine multipartite entangled states can not be detected this way as the particular witness (7.3) targets a subset of biseparable states [271].

The concept of GME can be further refined to expose more exotic quantum states. A special class of quantum states with separable two-body marginals exhibits GME which can be detected using only its separable two-body marginals [274]. Some of these states display a remarkable resilience against noise and were successfully reproduced in a contemporary experimental setting [252]. An astonishingly distinctive family exists within this class; states for which it is sufficient to only consider an incomplete set of their two-body marginals in detection of their GME [275]. The experimental demonstration of these states is the subject of an ongoing research endeavor.

Consider a k-partite quantum system characterized by its density matrix $\hat{\varrho}$. The possibly incomplete set S of its two-body marginals $\hat{\varrho}_{ij}$, used to detect the entanglement, is defined with

pairs of indices (i, j). The appropriately modified SDP [274, 275] becomes

$$\begin{aligned}
&\underset{\hat{W}\geq 0}{\text{minimize}} \ \operatorname{tr}(\hat{W}\hat{\varrho}) \\
&\text{subject to} \ \operatorname{tr}(\hat{W}) = 1 \\
&\qquad \hat{W} = \hat{P}_M + \hat{Q}_M^{T(M)} \quad \text{where} \quad \hat{Q}_M \geq 0, \hat{P}_M \geq 0 \,, \\
&\qquad \hat{W} = \sum_{(i,j)\in S} \sum_{m=0}^{3} \sum_{n=0}^{3} w_{mn}^{(ij)} \hat{\sigma}_m^{(i)} \otimes \hat{\sigma}_n^{(j)} \otimes \mathbb{1}^{\otimes(k-2)}
\end{aligned} \tag{7.4}$$

where $\hat{\sigma}_m^{(i)}$ denotes the mth Pauli matrix acting on the ith subsystem with the convention that $\hat{\sigma}_0 \equiv \hat{\mathbb{1}}$. The final constraint restricts the action of the witness matrix W to the chosen two-body marginals in the set S; each term in the sum acts only on a single two-body marginal $\hat{\varrho}_{ij}$. The coefficients $w_{mn}^{(ij)}$ give the decomposition of the witness matrix $\hat{W}$ in terms of Pauli matrices.

So far, the concept of GME was discussed within the context of discrete-variable quantum systems. The theory applies to continuous-variable systems as well; even the respective entanglement witnesses can be obtained through suitable SDP [272]. A legitimate question whether a similar class of GME states with separable two-body marginals exists within the continuous-variable setting was recently answered [253].

B Finding Witnesses of Genuine Multi-Partite Entanglement

A discrete-variable tripartite quantum state of three qubits with GME provable solely from its separable two-body marginals was experimentally prepared and certified [252] using a bespoke implementation of the SDP (7.4). The extension of the GME concept, based on (7.4), to the domain of continuous-variable Gaussian states [253] also relied on a software implementation of an appropriate SDP [272, Eq. 44–45] with the necessary modifications to ensure only partial information about the state was used.

The pertinent semi-definite programs were implemented by the author of this dissertation in a collaborative effort with the research team focusing on the theoretical and experimental aspects of the research works [252, 253].

C Conclusions

The work done both in [252] and [253] eventually culminated in the development of an open-source software library `witnessmess` [254] for Python [276] using `PICOS` [277] to interface a variety of semi-definite solvers, including the open-source convex optimization library `CVXOPT` [278] and the proprietary `MOSEK` solver [279]. The library implements the pertinent semi-definite programs adapted to search for optimal witnesses of GME utilizing only partial information about two-body marginalia. A pair of procedures is exposed; the first one determines the optimal witnesses with access to arbitrary, user-defined, subset of two-body marginalia for discrete-variable states of multiple qudits, while the other one can be used to achieve the same for continuous-variable multi-mode Gaussian states described by their covariance matrices.

The functionality of this library was supplemented by the development of another open source project, called `nomadlad` [255], providing a user-friendly interface to the blackbox optimization software `NOMAD` [280] based on the family of mesh-adaptive direct search algorithms [280–282].

Both libraries found their use in an ongoing research targeting an experimental preparation of the aforementioned exotic states, both in discrete-variable and continuous-variable settings.

Conclusions

This dissertation rests on the presented original research with general focus on contributing to the ever growing field of quantum information processing and fault-tolerant quantum computation with continuous-variable states of light. The research covered several avenues, including construction of non-Gaussian states, realization of non-Gaussian operations, quantification of non-Gaussian states in terms of their capability of producing quantum states with higher complexity, analysis and resolution of numerical issues inherent to simulation of continuous-variable quantum systems, and contributions to research of particular families of genuine multi-partite entanglement both in discrete and continuous-variable settings which resulted in publication of several open-source software libraries.

The individual conclusions regarding each research direction were summarized within the respective chapters and their abridged versions are repeated here for completeness.

Chapter 1: Improving on Single Photon Subtraction

The proposed loop-based single photon subtraction procedure achieved higher probability of success while retaining and even improving on the quality of the operation. Its performance was analyzed in several distinct applications, namely in preparation of a squeezed single photon state by subtracting a single photon from a squeezed vacuum state of light, transition between different parties of coherent Schrödinger states facilitated by photon subtraction and finally, in an entanglement distillation from a two mode squeezed vacuum state. The analysis took both realistic and ideal regimes of detection into account; in all of the applications, the procedure with ideal detectors allowed obtaining the quality of the standard single photon subtraction procedure while significantly increasing the success probability, often up to its theoretical maximum. For the realistic detectors with limited unit quantum efficiency, the maximal probabilities could no longer be reached, but the improvement was still clearly visible. In both cases the improvements were significant already for ten steps of the loop-based procedure.

Chapter 2: Preparing Approximate Cubic States

The non-Gaussian state preparation targeting cubic phase states, useful in the context of engineering non-linearly squeezed cubic states [50, 89, 176] for measurement induced cubic gates [50, 89, 90], employed a scheme based on suitable manipulation of a two mode squeezed vacuum with subsequent photon counting measurement [50, 88, 97, 198]. The effects of different detection mechanisms, including APD, PNRD and its approximations using APD cascades [184, 194] with varying number of APD detectors, were analyzed to ascertain the optimal approach towards state preparation. It was determined that in practical applications when PNRD is not available, using a single APD to engineer non-linearly squeezed states offers better performance compared to employing APD cascades comprising small numbers of detectors. This counter-intuitive result was attributed to the imperfections inherent to APD cascades [184] which are exaggerated with increased loss; the primary cause lies within the employed avalanche detectors as a single click may be triggered by multiple photons. This is a critical issue when engineering multi-photon states. The preparation circuit could be extended to utilize multiple displacements, detectors, and possibly even more complicated interactions. It could be, in principle, employed

in preparation of a wider variety of quantum states with practical applications, such as the optical grid states [50] required for fault-tolerant quantum computation.

Chapter 3: The Perils of Numerical Simulation

The analysis of the state preparation scheme relied heavily on numerical simulations. To ensure veracity of the findings, the numerical accuracy of several currently available methods [185, 199] used in construction of the truncated coherent displacement operator was analyzed. An alternative approach, based on the standard matrix exponential [206, 207] with truncated argument, was proposed, promising a better accuracy compared to the other techniques. The accuracy of the resulting matrix was ascertained using a verification strategy based on the recurrent formulae discussed in [185].

Chapter 4: Protecting Coherent Schrödinger States in Transit

The loss and noise plaguing bosonic channels deteriorates the non-Gaussian properties of quantum states. It limits the efficiency of quantum communication protocols and is one of the main bottlenecks for scalable quantum computation with optical fields. While the noise can be, potentially, compensated by error correction [50, 52, 131, 136–138], this is costly and should be attempted only after other, more feasible avenues, are explored first. One such mitigation strategy, based only on feasible Gaussian operations, was analyzed for coherent Schrödinger states. The strategy can can be realized either actively, by directly performing the Gaussian operation [229] on the state, or it can be incorporated directly into the state preparation stage of the communication protocols [109]. The mitigation strategy can be extended to reduce decoherence of the continuous variable component in quantum systems with hybrid entanglement between discrete qubits and continuous-variable CS states [110, 111, 140, 230]. While the method is most valuable for optical fields propagating through bosonic channels, the concept is general and can be straightforwardly employed to preserve the non-Gaussian property of quantum states in other bosonic systems, such as microwave cavities, spin systems, trapped ions, or optomechanics [231–238].

Chapter 5: Faster Computation of Fock Capability of non-Gaussian Resources

Single photon states — and quantum non-Gaussian states in general — serve an important role in quantum protocols. One of the possible measures of their quality can be obtained by interfering multiple incoherent copies of the state on a perfectly balanced multi-port interferometer [244] and counting the negative annuli of its Wigner function. This method was believed to be computationally intractable due to the exponential increase in computational complexity with respect to the number of copies. An alternative algorithm for the computation of the aggregate matrix of the interfered states offers an exponential improvement in the computational complexity over the original method. The calculation of the aggregate state only scales quadratically with the product dC of the number of copies C considered and dimension d of the initial state. The process of counting the negative annuli in the Wigner function, based on finding the positive real roots of a Laguerre series, scales cubically with the dimension of the aggregate state. The computational complexity of the entire measure consequently scales with $O(d^3C^3)$. The exponential improvement of the computational complexity makes it possible to explore physically relevant scenarios; for example by simulating a realistic state preparation circuit and analyzing the complex effects of loss on the Fock capability of prepared states. Furthermore, because the improvement lies in the computation of the aggregate state, the basis of the method can be employed with other qualitative measures, for example by considering the hierarchical criteria for genuine Fock states [161].

Chapter 6: Paving the Way Towards Four Photon Optical States

Individual photonic states of light can be conditionally prepared by projecting a two mode squeezed vacuum state onto the desired photonic state [97, 98, 178]. Neither the preparation of the squeezed state, its transmission, nor the detection process is ideal in a realistic experimental setting. It is possible to determine the minimal requirements on the efficiency of the experimental realization by modeling the state preparation process and taking the

effective loss into account, both in the construction of the desired state and during its characterization. The results presented in the chapter offer an insight into feasible experimental preparation of certifiable genuine m-photon states for $m = 2, 3, 4$. While preparation of quantum states of travelling light of up to three photons has already seen its experimental realization [97], the construction of a 4-photon state of travelling light still remains an open problem that may benefit from this analysis.

Chapter 7: Witnessing Genuine Multi-Partite Entanglement

Genuine multi-partite entanglement certainly is an interesting phenomenon unique to quantum physics. Exotic quantum states exist with their genuine multi-partite entangled nature provable solely from their separable two-body marginals [252, 253]. The certification of these states utilized specialised semi-definite programs. The implementation of the pertinent semi-definite programs for internal use of the research teams involved in the experimental preparation and detection of the discrete-variable versions of these states [252] and in the theoretical research of their continuous-variable counterparts [253] culminated in development and publication of open-source software libraries `witnessmess` [254] and `nomadlad` [255]. The former library implements the relevant semi-definite programs adapted to search for optimal witnesses of GME utilizing only partial information about two-body marginalia, while the latter library provides a user-friendly interface to the black-box optimization software `NOMAD` [280].

This concludes the conclusion of the dissertation.

Overview of Publications

1. P. Marek, J. **Provazník**, and R. Filip. "Loop-based subtraction of a single photon from a traveling beam of light." In: *Optics Express* 26.23 (Oct. 2018), p. 29837. DOI: 10.1364/oe.26.029837
2. M. Mičuda, R. Stárek, J. **Provazník**, O. Leskovjanová, and L. Mišta. "Verifying genuine multipartite entanglement of the whole from its separable parts." In: *Optica* 6.7 (July 2019), p. 896. DOI: 10.1364/optica.6.000896
3. J. **Provazník**, L. Lachman, R. Filip, and P. Marek. "Benchmarking photon number resolving detectors." In: *Optics Express* 28.10 (May 2020), p. 14839. DOI: 10.1364/oe.389619
4. J. **Provazník**, R. Filip, and P. Marek. "Taming numerical errors in simulations of continuous variable non-Gaussian state preparation." In: *Scientific Reports* 12.1 (Oct. 2022). DOI: 10.1038/s41598-022-19506-9
5. V. Nordgren, O. Leskovjanová, J. **Provazník**, A. Johnston, N. Korolkova, and L. Mišta. "Certifying emergent genuine multipartite entanglement with a partially blind witness." In: *Physical Review A* 106.6 (Dec. 2022). DOI: 10.1103/physreva.106.062410

Publications currently under review

6. J. **Provazník**, P. Marek, J. Laurat, and R. Filip. "Adapting coherent-state superpositions in noisy channels." In: *Under review* (2024). DOI: 10.48550/ARXIV.2406.01081

Publications in preparation

7. J. **Provazník**, O. Solodovnikova, R. Filip, and P. Marek. "Exponential improvement in the computational complexity of Fock capability of non-Gaussian Resources." In: *In preparation* (Dec. 2024)
8. J. **Provazník**, O. Solodovnikova, R. Filip, and P. Marek. "Paving the way towards four photon optical states." In: *In preparation* (Dec. 2024)

Overview of Published Software

[254] `witnessmess`

Witnessing multi-partite entanglement in Python.

- Source available through https://github.com/jan-provaznik/witnessmess
- Installable as a package via PyPi https://pypi.org/project/witnessmess
- Published under LGPL-3.0

[255] `nomadlad`

Python interface to the blackbox optimization software NOMAD (version 4.4) [280].

- Source available through https://github.com/jan-provaznik/nomadlad
- Installable as a package via PyPi https://pypi.org/project/nomadlad
- Published under LGPL-3.0

[283] `departed`

Partial trace and partial transposition for Kronecker representation of multi-partite discrete variable quantum systems. Primarily for educational purposes.

- Source available through https://github.com/jan-provaznik/departed
- Installable as a package via PyPi https://pypi.org/project/departed
- Published under LGPL-3.0

Bibliography

[1] M. Brooks. "Quantum computers: what are they good for?" In: *Nature* 617.7962 (May 2023), S1–S3. DOI: 10.1038/d41586-023-01692-9.

[2] R. P. Feynman. "Simulating physics with computers." In: *International Journal of Theoretical Physics* 21.6-7 (1982), pp. 467–488. DOI: 10.1007/bf02650179.

[3] R. P. Feynman. "Quantum mechanical computers." In: *Foundations of Physics* 16.6 (1986), pp. 507–531. DOI: 10.1007/bf01886518.

[4] A. Montanaro. "Quantum algorithms: an overview." In: *npj Quantum Information* 2.1 (Jan. 2016). DOI: 10.1038/npjqi.2015.23.

[5] P. Shor. "Algorithms for quantum computation: discrete logarithms and factoring." In: IEEE Comput. Soc. Press, Dec. 2002. DOI: 10.1109/sfcs.1994.365700.

[6] P. W. Shor. "Polynomial-Time Algorithms for Prime Factorization and Discrete Logarithms on a Quantum Computer." In: *SIAM Journal on Computing* 26.5 (1997), pp. 1484–1509. DOI: 10.1137/s0097539795293172.

[7] A. M. Childs et al. "Quantum algorithms for algebraic problems." In: *Reviews of Modern Physics* 82.1 (Jan. 2010), pp. 1–52. DOI: 10.1103/revmodphys.82.1.

[8] J. Biamonte et al. "Quantum machine learning." In: *Nature* 549.7671 (2017), pp. 195–202. DOI: 10.1038/nature23474.

[9] L. K. Grover. "A fast quantum mechanical algorithm for database search." In: ACM Press, 1996. DOI: 10.1145/237814.237866.

[10] I. M. Georgescu et al. "Quantum simulation." In: *Reviews of Modern Physics* 86.1 (Mar. 2014), pp. 153–185. DOI: 10.1103/revmodphys.86.153.

[11] B. Fauseweh. "Quantum many-body simulations on digital quantum computers: State-of-the-art and future challenges." In: *Nature Communications* 15.1 (Mar. 2024). DOI: 10.1038/s41467-024-46402-9.

[12] S. McArdle et al. "Quantum computational chemistry." In: *Reviews of Modern Physics* 92.1 (Mar. 2020). DOI: 10.1103/revmodphys.92.015003.

[13] B. Schumacher. "Quantum coding." In: *Physical Review A* 51.4 (Apr. 1995), pp. 2738–2747. DOI: 10.1103/physreva.51.2738.

[14] C. E. Shannon. "A Mathematical Theory of Communication." In: *Bell System Technical Journal* 27.3 (1948), pp. 379–423. DOI: 10.1002/j.1538-7305.1948.tb01338.x.

[15] *Mathematics of Quantum Computation*. Chapman and Hall/CRC, Feb. 2002. DOI: 10.1201/9781420035377.

[16] M. Ringbauer et al. "A universal qudit quantum processor with trapped ions." In: *Nature Physics* 18.9 (July 2022), pp. 1053–1057. DOI: 10.1038/s41567-022-01658-0.

[17] D. Deutsch. "Quantum theory, the Church–Turing principle and the universal quantum computer." In: *Proc. R. Soc. Lond.* 400.1818 (July 1985), pp. 97–117.

[18] C. A. Pérez-Delgado et al. "Quantum computers: Definition and implementations." In: *Physical Review A* 83.1 (Jan. 2011). DOI: 10.1103/physreva.83.012303.

[19] S. Lloyd et al. “Quantum Computation over Continuous Variables.” In: *Physical Review Letters* 82.8 (Feb. 1999), pp. 1784–1787. DOI: 10.1103/physrevlett.82.1784.

[20] A. M. Turing. “On Computable Numbers, with an Application to the Entscheidungsproblem.” In: *Proceedings of the London Mathematical Society* s2-42.1 (1937), pp. 230–265. DOI: 10.1112/plms/s2-42.1.230.

[21] C. E. Shannon. “Mathematical Theory of the Differential Analyzer.” In: *Journal of Mathematics and Physics* 20.1-4 (1941), pp. 337–354. DOI: 10.1002/sapm1941201337.

[22] S. Abel et al. “Simulating quantum field theories on continuous-variable quantum computers.” In: *Physical Review A* 110.1 (July 2024). DOI: 10.1103/physreva.110.012607.

[23] K. Marshall et al. “Quantum simulation of quantum field theory using continuous variables.” In: *Physical Review A* 92.6 (Dec. 2015). DOI: 10.1103/physreva.92.063825.

[24] X. Deng et al. “Continuous variable quantum optical simulation for time evolution of quantum harmonic oscillators.” In: *Scientific Reports* 6.1 (Mar. 2016). DOI: 10.1038/srep22914.

[25] M. A. Nielsen et al. *Quantum computation and quantum information*. Cambridge New York: Cambridge University Press, 2000.

[26] S. Aaronson et al. In: *Theory of Computing* 9.1 (2013), pp. 143–252. DOI: 10.4086/toc.2013.v009a004.

[27] C. S. Hamilton et al. “Gaussian Boson Sampling.” In: *Physical Review Letters* 119.17 (Oct. 2017). DOI: 10.1103/physrevlett.119.170501.

[28] R. Orús. “A practical introduction to tensor networks: Matrix product states and projected entangled pair states.” In: *Annals of Physics* 349 (2014), pp. 117–158. DOI: 10.1016/j.aop.2014.06.013.

[29] C. Oh et al. “Classical algorithm for simulating experimental Gaussian boson sampling.” In: *Nature Physics* (June 2024). DOI: 10.1038/s41567-024-02535-8.

[30] J. Tindall et al. “Efficient Tensor Network Simulation of IBM’s Eagle Kicked Ising Experiment.” In: *PRX Quantum* 5.1 (Jan. 2024). DOI: 10.1103/prxquantum.5.010308.

[31] S. D. Bartlett et al. “Efficient Classical Simulation of Continuous Variable Quantum Information Processes.” In: *Physical Review Letters* 88.9 (Feb. 2002). DOI: 10.1103/physrevlett.88.097904.

[32] S. D. Barrett et al. “Scalable quantum computing with atomic ensembles.” In: *New Journal of Physics* 12.9 (Sept. 2010), p. 093032. DOI: 10.1088/1367-2630/12/9/093032.

[33] S. D. Barrett et al. “Fault Tolerant Quantum Computation with Very High Threshold for Loss Errors.” In: *Physical Review Letters* 105.20 (Nov. 2010). DOI: 10.1103/physrevlett.105.200502.

[34] Y. Li et al. “Fault Tolerant Quantum Computation with Nondeterministic Gates.” In: *Physical Review Letters* 105.25 (Dec. 2010). DOI: 10.1103/physrevlett.105.250502.

[35] J. I. Cirac et al. “Quantum Computations with Cold Trapped Ions.” In: *Physical Review Letters* 74.20 (May 1995), pp. 4091–4094. DOI: 10.1103/physrevlett.74.4091.

[36] T. P. Harty et al. “High-Fidelity Preparation, Gates, Memory, and Readout of a Trapped-Ion Quantum Bit.” In: *Physical Review Letters* 113.22 (Nov. 2014). DOI: 10.1103/physrevlett.113.220501.

[37] C. J. Ballance et al. “High-Fidelity Quantum Logic Gates Using Trapped-Ion Hyperfine Qubits.” In: *Physical Review Letters* 117.6 (Aug. 2016). DOI: 10.1103/physrevlett.117.060504.

[38] J. P. Gaebler et al. “High-Fidelity Universal Gate Set for $^{9}Be^{+}$ Ion Qubits.” In: *Physical Review Letters* 117.6 (Aug. 2016). DOI: 10.1103/physrevlett.117.060505.

[39] N. M. Linke et al. “Experimental comparison of two quantum computing architectures.” In: *Proceedings of the National Academy of Sciences* 114.13 (Mar. 2017), pp. 3305–3310. DOI: 10.1073/pnas.1618020114.

[40] V. M. Schäfer et al. “Fast quantum logic gates with trapped-ion qubits.” In: *Nature* 555.7694 (2018), pp. 75–78. DOI: 10.1038/nature25737.

[41] J. Clarke et al. “Superconducting quantum bits.” In: *Nature* 453.7198 (2008), pp. 1031–1042. DOI: 10.1038/nature07128.

[42] E. Lucero et al. “High-Fidelity Gates in a Single Josephson Qubit.” In: *Physical Review Letters* 100.24 (June 2008). DOI: 10.1103/physrevlett.100.247001.

[43] J. M. Chow et al. “Randomized Benchmarking and Process Tomography for Gate Errors in a Solid-State Qubit.” In: *Physical Review Letters* 102.9 (Mar. 2009). DOI: 10.1103/physrevlett.102.090502.

[44] C. Rigetti et al. “Superconducting qubit in a waveguide cavity with a coherence time approaching 0.1 ms.” In: *Physical Review B* 86.10 (Sept. 2012). DOI: 10.1103/physrevb.86.100506.

[45] M. H. Devoret et al. “Superconducting Circuits for Quantum Information: An Outlook.” In: *Science* 339.6124 (Mar. 2013), pp. 1169–1174. DOI: 10.1126/science.1231930.

[46] R. Barends et al. “Superconducting quantum circuits at the surface code threshold for fault tolerance.” In: *Nature* 508.7497 (2014), pp. 500–503. DOI: 10.1038/nature13171.

[47] P. Krantz et al. “A quantum engineer’s guide to superconducting qubits.” In: *Applied Physics Reviews* 6.2 (June 2019). DOI: 10.1063/1.5089550.

[48] J. L. O’Brien. “Optical Quantum Computing.” In: *Science* 318.5856 (Dec. 2007), pp. 1567–1570. DOI: 10.1126/science.1142892.

[49] E. Knill et al. “A scheme for efficient quantum computation with linear optics.” In: *Nature* 409.6816 (2001), pp. 46–52. DOI: 10.1038/35051009.

[50] D. Gottesman et al. “Encoding a qubit in an oscillator.” In: *Physical Review A* 64.1 (June 2001). DOI: 10.1103/physreva.64.012310.

[51] T. C. Ralph et al. “Quantum computation with optical coherent states.” In: *Physical Review A* 68.4 (Oct. 2003). DOI: 10.1103/physreva.68.042319.

[52] A. P. Lund et al. “Fault-Tolerant Linear Optical Quantum Computing with Small-Amplitude Coherent States.” In: *Physical Review Letters* 100.3 (Jan. 2008). DOI: 10.1103/physrevlett.100.030503.

[53] Z. Leghtas et al. “Hardware-Efficient Autonomous Quantum Memory Protection.” In: *Physical Review Letters* 111.12 (Sept. 2013). DOI: 10.1103/physrevlett.111.120501.

[54] M. Mirrahimi et al. “Dynamically protected cat-qubits: a new paradigm for universal quantum computation.” In: *New Journal of Physics* 16.4 (Apr. 2014), p. 045014. DOI: 10.1088/1367-2630/16/4/045014.

[55] N. Ofek et al. “Extending the lifetime of a quantum bit with error correction in superconducting circuits.” In: *Nature* 536.7617 (July 2016), pp. 441–445. DOI: 10.1038/nature18949.

[56] H.-K. Lau et al. “Universal Quantum Computing with Arbitrary Continuous-Variable Encoding.” In: *Physical Review Letters* 117.10 (Aug. 2016). DOI: 10.1103/physrevlett.117.100501.

[57] N. C. Menicucci et al. “Universal Quantum Computation with Continuous-Variable Cluster States.” In: *Physical Review Letters* 97.11 (Sept. 2006). DOI: 10.1103/physrevlett.97.110501.

[58] I. Tzitrin et al. “Progress towards practical qubit computation using approximate Gottesman-Kitaev-Preskill codes.” In: *Physical Review A* 101.3 (Mar. 2020). DOI: 10.1103/physreva.101.032315.

[59] I. Tzitrin et al. “Fault-Tolerant Quantum Computation with Static Linear Optics.” In: *PRX Quantum* 2.4 (Dec. 2021). DOI: 10.1103/prxquantum.2.040353.

[60] J. E. Bourassa et al. “Blueprint for a Scalable Photonic Fault-Tolerant Quantum Computer.” In: *Quantum* 5 (Feb. 2021), p. 392. DOI: 10.22331/q-2021-02-04-392.

[61] R. Raussendorf et al. “A One-Way Quantum Computer.” In: *Physical Review Letters* 86.22 (May 2001), pp. 5188–5191. DOI: 10.1103/physrevlett.86.5188.

[62] R. Raussendorf et al. “A fault-tolerant one-way quantum computer.” In: *Annals of Physics* 321.9 (2006), pp. 2242–2270. DOI: 10.1016/j.aop.2006.01.012.

[63] S. Yokoyama et al. “Ultra-large-scale continuous-variable cluster states multiplexed in the time domain.” In: *Nature Photonics* 7.12 (Nov. 2013), pp. 982–986. DOI: 10.1038/nphoton.2013.287.

[64] M. Chen et al. “Experimental Realization of Multipartite Entanglement of 60 Modes of a Quantum Optical Frequency Comb.” In: *Physical Review Letters* 112.12 (Mar. 2014). DOI: 10.1103/physrevlett.112.120505.

[65] J.-i. Yoshikawa et al. “Invited Article: Generation of one-million-mode continuous-variable cluster state by unlimited time-domain multiplexing.” In: *APL Photonics* 1.6 (Sept. 2016). DOI: 10.1063/1.4962732.

[66] M. V. Larsen et al. “Deterministic generation of a two-dimensional cluster state.” In: *Science* 366.6463 (Oct. 2019), pp. 369–372. DOI: 10.1126/science.aay4354.

[67] W. Asavanant et al. “Generation of time-domain-multiplexed two-dimensional cluster state.” In: *Science* 366.6463 (Oct. 2019), pp. 373–376. DOI: 10.1126/science.aay2645.

[68] W. Asavanant et al. “Time-Domain-Multiplexed Measurement-Based Quantum Operations with 25-MHz Clock Frequency.” In: *Physical Review Applied* 16.3 (Sept. 2021). DOI: 10.1103/physrevapplied.16.034005.

[69] B.-H. Wu et al. “Quantum computing with multidimensional continuous-variable cluster states in a scalable photonic platform.” In: *Physical Review Research* 2.2 (May 2020). DOI: 10.1103/physrevresearch.2.023138.

[70] K. Fukui et al. “Temporal-mode continuous-variable three-dimensional cluster state for topologically protected measurement-based quantum computation.” In: *Physical Review A* 102.3 (Sept. 2020). DOI: 10.1103/physreva.102.032614.

[71] X. Zhu et al. “Hypercubic cluster states in the phase-modulated quantum optical frequency comb.” In: *Optica* 8.3 (Mar. 2021), p. 281. DOI: 10.1364/optica.411713.

[72] M. V. Larsen et al. “Fault-Tolerant Continuous-Variable Measurement-based Quantum Computation Architecture.” In: *PRX Quantum* 2.3 (Aug. 2021). DOI: 10.1103/prxquantum.2.030325.

[73] A. Inoue et al. “Toward a multi-core ultra-fast optical quantum processor: 43-GHz bandwidth real-time amplitude measurement of 5-dB squeezed light using modularized optical parametric amplifier with 5G technology.” In: *Applied Physics Letters* 122.10 (Mar. 2023). DOI: 10.1063/5.0137641.

[74] P. van Loock. “Quantum Communication with Continuous Variables.” In: *Fortschritte der Physik* 50.12 (2002), pp. 1177–1372. DOI: 10.1002/1521-3978(200212)50:12<1177::aid-prop1177>3.0.co;2-t.

[75] N. J. Cerf et al. *Quantum Information with Continuous Variables of Atoms and Light*. PUBLISHED BY IMPERIAL COLLEGE PRESS and DISTRIBUTED BY WORLD SCIENTIFIC PUBLISHING CO., 2007. DOI: 10.1142/p489.

[76] Z.-S. Yuan et al. “Entangled photons and quantum communication.” In: *Physics Reports* 497.1 (2010), pp. 1–40. DOI: 10.1016/j.physrep.2010.07.004.

[77] W. Luo et al. “Recent progress in quantum photonic chips for quantum communication and internet.” In: *Light: Science & Applications* 12.1 (July 2023). DOI: 10.1038/s41377-023-01173-8.

[78] S. Pirandola et al. “Advances in quantum cryptography.” In: *Advances in Optics and Photonics* 12.4 (Dec. 2020), p. 1012. DOI: 10.1364/aop.361502.

[79] R. Loudon. *The quantum theory of light*. 3rd ed. London, England: Oxford University Press, Sept. 2000.

[80] J. H. Shapiro. “Single-photon Kerr nonlinearities do not help quantum computation.” In: *Physical Review A* 73.6 (June 2006). DOI: 10.1103/physreva.73.062305.

[81] J. Gea-Banacloche. “Impossibility of large phase shifts via the giant Kerr effect with single-photon wave packets.” In: *Physical Review A* 81.4 (Apr. 2010). DOI: 10.1103/physreva.81.043823.

[82] C. Weedbrook et al. “Gaussian quantum information.” In: *Reviews of Modern Physics* 84.2 (May 2012), pp. 621–669. DOI: 10.1103/revmodphys.84.621.

[83] J. Eisert et al. “Distilling Gaussian States with Gaussian Operations is Impossible.” In: *Physical Review Letters* 89.13 (Sept. 2002). DOI: 10.1103/physrevlett.89.137903.

[84] J. Fiurášek. “Gaussian Transformations and Distillation of Entangled Gaussian States.” In: *Physical Review Letters* 89.13 (Sept. 2002). DOI: 10.1103/physrevlett.89.137904.

[85] G. Giedke et al. “Characterization of Gaussian operations and distillation of Gaussian states.” In: *Physical Review A* 66.3 (Sept. 2002). DOI: 10.1103/physreva.66.032316.

[86] P. Marek et al. “Resources for universal quantum-state manipulation and engineering.” In: *Physical Review A* 79.6 (June 2009). DOI: 10.1103/physreva.79.062321.

[87] P. Marek et al. “Deterministic implementation of weak quantum cubic nonlinearity.” In: *Physical Review A* 84.5 (Nov. 2011). DOI: 10.1103/physreva.84.053802.

[88] M. Yukawa et al. “Emulating quantum cubic nonlinearity.” In: *Physical Review A* 88.5 (Nov. 2013). DOI: 10.1103/physreva.88.053816.

[89] K. Miyata et al. “Implementation of a quantum cubic gate by an adaptive non-Gaussian measurement.” In: *Physical Review A* 93.2 (Feb. 2016). DOI: 10.1103/physreva.93.022301.

[90] P. Marek et al. “General implementation of arbitrary nonlinear quadrature phase gates.” In: *Physical Review A* 97.2 (Feb. 2018). DOI: 10.1103/physreva.97.022329.

[91] A. Sakaguchi et al. “Nonlinear feedforward enabling quantum computation.” In: *Nature Communications* 14.1 (July 2023). DOI: 10.1038/s41467-023-39195-w.

[92] M. Dakna et al. “Generation of arbitrary quantum states of traveling fields.” In: *Physical Review A* 59.2 (Feb. 1999), pp. 1658–1661. DOI: 10.1103/physreva.59.1658.

[93] J. Fiurášek et al. “Conditional generation of arbitrary single-mode quantum states of light by repeated photon subtractions.” In: *Physical Review A* 72.3 (Sept. 2005). DOI: 10.1103/physreva.72.033822.

[94] M. Endo et al. “Non-Gaussian quantum state generation by multi-photon subtraction at the telecommunication wavelength.” In: *Optics Express* 31.8 (Apr. 2023), p. 12865. DOI: 10.1364/oe.486270.

[95] M. Eaton et al. “Non-Gaussian and Gottesman–Kitaev–Preskill state preparation by photon catalysis.” In: *New Journal of Physics* 21.11 (Nov. 2019), p. 113034. DOI: 10.1088/1367-2630/ab5330.

[96] K. Takase et al. “Generation of optical Schrödinger cat states by generalized photon subtraction.” In: *Physical Review A* 103.1 (Jan. 2021). DOI: 10.1103/physreva.103.013710.

[97] M. Yukawa et al. “Generating superposition of up-to three photons for continuous variable quantum information processing.” In: *Optics Express* 21.5 (Feb. 2013), p. 5529. DOI: 10.1364/oe.21.005529.

[98] J. Tiedau et al. “Scalability of parametric down-conversion for generating higher-order Fock states.” In: *Physical Review A* 100.4 (Oct. 2019). DOI: 10.1103/physreva.100.041802.

[99] D. Su et al. “Conversion of Gaussian states to non-Gaussian states using photon-number-resolving detectors.” In: *Physical Review A* 100.5 (Nov. 2019). DOI: 10.1103/physreva.100.052301.

[100] N. Quesada et al. “Simulating realistic non-Gaussian state preparation.” In: *Physical Review A* 100.2 (Aug. 2019). DOI: 10.1103/physreva.100.022341.

[101] K. Fukui et al. “Efficient Backcasting Search for Optical Quantum State Synthesis.” In: *Physical Review Letters* 128.24 (June 2022). DOI: 10.1103/physrevlett.128.240503.

[102] D. J. Weigand et al. “Generating grid states from Schrödinger-cat states without postselection.” In: *Physical Review A* 97.2 (Feb. 2018). DOI: 10.1103/physreva.97.022341.

[103] M. Eaton et al. “Measurement-based generation and preservation of cat and grid states within a continuous-variable cluster state.” In: *Quantum* 6 (July 2022), p. 769. DOI: 10.22331/q-2022-07-20-769.

[104] Y. Zheng et al. “Gaussian conversion protocol for heralded generation of generalized Gottesman-Kitaev-Preskill states.” In: *Physical Review A* 108.1 (July 2023). DOI: 10.1103/physreva.108.012603.

[105] K. Takase et al. “Generation of flying logical qubits using generalized photon subtraction with adaptive Gaussian operations.” In: *Physical Review A* 110.1 (July 2024). DOI: 10.1103/physreva.110.012436.

[106] P. Marek et al. “Loop-based subtraction of a single photon from a traveling beam of light.” In: *Optics Express* 26.23 (Oct. 2018), p. 29837. DOI: 10.1364/oe.26.029837.

[107] A. Ourjoumtsev et al. “Generating Optical Schrödinger Kittens for Quantum Information Processing.” In: *Science* 312.5770 (Apr. 2006), pp. 83–86. DOI: 10.1126/science.1122858.

[108] K. Huang et al. “Experimental quantum state engineering with time-separated heraldings from a continuous-wave light source: A temporal-mode analysis.” In: *Physical Review A* 93.1 (Jan. 2016). DOI: 10.1103/physreva.93.013838.

[109] H. Le Jeannic et al. “Slowing Quantum Decoherence by Squeezing in Phase Space.” In: *Physical Review Letters* 120.7 (Feb. 2018). DOI: 10.1103/physrevlett.120.073603.

[110] H. Le Jeannic et al. “Remote preparation of continuous-variable qubits using loss-tolerant hybrid entanglement of light.” In: *Optica* 5.8 (Aug. 2018), p. 1012. DOI: 10.1364/optica.5.001012.

[111] A. Cavaillès et al. “Demonstration of Einstein-Podolsky-Rosen Steering Using Hybrid Continuous- and Discrete-Variable Entanglement of Light.” In: *Physical Review Letters* 121.17 (Oct. 2018). DOI: 10.1103/physrevlett.121.170403.

[112] M. A. Usuga et al. “Noise-powered probabilistic concentration of phase information.” In: *Nature Physics* 6.10 (Aug. 2010), pp. 767–771. DOI: 10.1038/nphys1743.

[113] A. Zavatta et al. “A high-fidelity noiseless amplifier for quantum light states.” In: *Nature Photonics* 5.1 (Nov. 2010), pp. 52–56. DOI: 10.1038/nphoton.2010.260.

[114] C. H. Bennett et al. “Purification of Noisy Entanglement and Faithful Teleportation via Noisy Channels.” In: *Physical Review Letters* 76.5 (Jan. 1996), pp. 722–725. DOI: 10.1103/physrevlett.76.722.

[115] T. Opatrný et al. “Improvement on teleportation of continuous variables by photon subtraction via conditional measurement.” In: *Physical Review A* 61.3 (Feb. 2000). DOI: 10.1103/physreva.61.032302.

[116] H. Takahashi et al. “Entanglement distillation from Gaussian input states.” In: *Nature Photonics* 4.3 (Feb. 2010), pp. 178–181. DOI: 10.1038/nphoton.2010.1.

[117] T. J. Bartley et al. “Strategies for enhancing quantum entanglement by local photon subtraction.” In: *Physical Review A* 87.2 (Feb. 2013). DOI: 10.1103/physreva.87.022313.

[118] Y. Kurochkin et al. “Distillation of The Two-Mode Squeezed State.” In: *Physical Review Letters* 112.7 (Feb. 2014). DOI: 10.1103/physrevlett.112.070402.

[119] J.-i. Yoshikawa et al. “Creation, Storage, and On-Demand Release of Optical Quantum States with a Negative Wigner Function.” In: *Physical Review X* 3.4 (Dec. 2013). DOI: 10.1103/physrevx.3.041028.

[120] S. Takeda et al. “Universal Quantum Computing with Measurement-Induced Continuous-Variable Gate Sequence in a Loop-Based Architecture.” In: *Physical Review Letters* 119.12 (Sept. 2017). DOI: 10.1103/physrevlett.119.120504.

[121] M. Fuwa et al. “Noiseless Conditional Teleportation of a Single Photon.” In: *Physical Review Letters* 113.22 (Nov. 2014). DOI: 10.1103/physrevlett.113.223602.

[122] J. S. Ivan et al. “Operator-sum representation for bosonic Gaussian channels.” In: *Physical Review A* 84.4 (Oct. 2011). DOI: 10.1103/physreva.84.042311.

[123] H. Le Jeannic et al. “High-efficiency WSi superconducting nanowire single-photon detectors for quantum state engineering in the near infrared.” In: *Optics Letters* 41.22 (Nov. 2016), p. 5341. DOI: 10.1364/ol.41.005341.

[124] R. Hudson. “When is the wigner quasi-probability density non-negative?” In: *Reports on Mathematical Physics* 6.2 (1974), pp. 249–252. DOI: 10.1016/0034-4877(74)90007-x.

[125] R. Filip et al. “Detecting Quantum States with a Positive Wigner Function beyond Mixtures of Gaussian States.” In: *Physical Review Letters* 106.20 (May 2011). DOI: 10.1103/physrevlett.106.200401.

[126] A. Mari et al. “Positive Wigner Functions Render Classical Simulation of Quantum Computation Efficient.” In: *Physical Review Letters* 109.23 (Dec. 2012). DOI: 10.1103/physrevlett.109.230503.

[127] M. Walschaers. “Non-Gaussian Quantum States and Where to Find Them.” In: *PRX Quantum* 2.3 (Sept. 2021). DOI: 10.1103/prxquantum.2.030204.

[128] C. T. Lee. “Measure of the nonclassicality of nonclassical states.” In: *Physical Review A* 44.5 (Sept. 1991), R2775–R2778. DOI: 10.1103/physreva.44.r2775.

[129] H. Jeong et al. “Efficient quantum computation using coherent states.” In: *Physical Review A* 65.4 (Mar. 2002). DOI: 10.1103/physreva.65.042305.

[130] K. Park et al. “Entangled coherent states versus entangled photon pairs for practical quantum-information processing.” In: *Physical Review A* 82.6 (Dec. 2010). DOI: 10.1103/physreva.82.062325.

[131] J. Hastrup et al. “All-optical cat-code quantum error correction.” In: *Physical Review Research* 4.4 (Oct. 2022). DOI: 10.1103/physrevresearch.4.043065.

[132] T. Rudolph. “Why I am optimistic about the silicon-photonic route to quantum computing.” In: *APL Photonics* 2.3 (Mar. 2017). DOI: 10.1063/1.4976737.

[133] S. Omkar et al. “Resource-Efficient Topological Fault-Tolerant Quantum Computation with Hybrid Entanglement of Light.” In: *Physical Review Letters* 125.6 (Aug. 2020). DOI: 10.1103/physrevlett.125.060501.

[134] D. S. Schlegel et al. “Quantum error correction using squeezed Schrödinger cat states.” In: *Physical Review A* 106.2 (Aug. 2022). DOI: 10.1103/physreva.106.022431.

[135] H. M. Vasconcelos et al. “All-optical generation of states for “Encoding a qubit in an oscillator”.” In: *Optics Letters* 35.19 (Sept. 2010), p. 3261. DOI: 10.1364/ol.35.003261.

[136] N. C. Menicucci. “Fault-Tolerant Measurement-Based Quantum Computing with Continuous-Variable Cluster States.” In: *Physical Review Letters* 112.12 (Mar. 2014). DOI: 10.1103/physrevlett.112.120504.

[137] B. Q. Baragiola et al. “All-Gaussian Universality and Fault Tolerance with the Gottesman-Kitaev-Preskill Code.” In: *Physical Review Letters* 123.20 (Nov. 2019). DOI: 10.1103/physrevlett.123.200502.

[138] G. Pantaleoni et al. “Modular Bosonic Subsystem Codes.” In: *Physical Review Letters* 125.4 (July 2020). DOI: 10.1103/physrevlett.125.040501.

[139] P. Minzioni et al. “Roadmap on all-optical processing.” In: *Journal of Optics* 21.6 (May 2019), p. 063001. DOI: 10.1088/2040-8986/ab0e66.

[140] G. Guccione et al. “Connecting heterogeneous quantum networks by hybrid entanglement swapping.” In: *Science Advances* 6.22 (May 2020). DOI: 10.1126/sciadv.aba4508.

[141] T. Darras et al. “A quantum-bit encoding converter.” In: *Nature Photonics* 17.2 (Dec. 2022), pp. 165–170. DOI: 10.1038/s41566-022-01117-5.

[142] A. Shinjo et al. “Three-Dimensional Matter-Wave Interferometry of a Trapped Single Ion.” In: *Physical Review Letters* 126.15 (Apr. 2021). DOI: 10.1103/physrevlett.126.153604.

[143] A. R. Milne et al. “Quantum Oscillator Noise Spectroscopy via Displaced Cat States.” In: *Physical Review Letters* 126.25 (June 2021). DOI: 10.1103/physrevlett.126.250506.

[144] R. Filip. “Amplification of Schrödinger-cat state in a degenerate optical parametric amplifier.” In: *Journal of Optics B: Quantum and Semiclassical Optics* 3.1 (Jan. 2001), S1–S6. DOI: 10.1088/1464-4266/3/1/351.

[145] A. Serafini et al. “Minimum decoherence cat-like states in Gaussian noisy channels.” In: *Journal of Optics B: Quantum and Semiclassical Optics* 6.6 (May 2004), S591–S596. DOI: 10.1088/1464-4266/6/6/019.

[146] R. Y. Teh et al. “Overcoming decoherence of Schrödinger cat states formed in a cavity using squeezed-state inputs.” In: *Physical Review Research* 2.4 (Dec. 2020). DOI: 10.1103/physrevresearch.2.043387.

[147] R. Filip. “Gaussian quantum adaptation of non-Gaussian states for a lossy channel.” In: *Physical Review A* 87.4 (Apr. 2013). DOI: 10.1103/physreva.87.042308.

[148] R. A. Brewster et al. “Reduced decoherence using squeezing, amplification, and anti-squeezing.” In: *Physical Review A* 98.3 (Sept. 2018). DOI: 10.1103/physreva.98.033818.

[149] X. Pan et al. “Protecting the Quantum Interference of Cat States by Phase-Space Compression.” In: *Physical Review X* 13.2 (Apr. 2023). DOI: 10.1103/physrevx.13.021004.

[150] A. Ourjoumtsev et al. “Increasing Entanglement between Gaussian States by Coherent Photon Subtraction.” In: *Physical Review Letters* 98.3 (Jan. 2007). DOI: 10.1103/physrevlett.98.030502.

[151] A. Zavatta et al. “Quantum-to-Classical Transition with Single-Photon-Added Coherent States of Light.” In: *Science* 306.5696 (Oct. 2004), pp. 660–662. DOI: 10.1126/science.1103190.

[152] V. Parigi et al. “Probing Quantum Commutation Rules by Addition and Subtraction of Single Photons to/from a Light Field.” In: *Science* 317.5846 (Sept. 2007), pp. 1890–1893. DOI: 10.1126/science.1146204.

[153] G. Adesso et al. “Entanglement in continuous-variable systems: recent advances and current perspectives.” In: *Journal of Physics A: Mathematical and Theoretical* 40.28 (June 2007), pp. 7821–7880. DOI: 10.1088/1751-8113/40/28/s01.

[154] G. Vidal et al. “Computable measure of entanglement.” In: *Physical Review A* 65.3 (Feb. 2002). DOI: 10.1103/physreva.65.032314.

[155] M. M. Wolf et al. “Extremality of Gaussian Quantum States.” In: *Physical Review Letters* 96.8 (Mar. 2006). DOI: 10.1103/physrevlett.96.080502.

[156] J. Provazník et al. “Taming numerical errors in simulations of continuous variable non-Gaussian state preparation.” In: *Scientific Reports* 12.1 (Oct. 2022). DOI: 10.1038/s41598-022-19506-9.

[157] H.-S. Zhong et al. “Quantum computational advantage using photons.” In: *Science* 370.6523 (Dec. 2020), pp. 1460–1463. DOI: 10.1126/science.abe8770.

[158] S. L. Braunstein et al. “Quantum information with continuous variables.” In: *Reviews of Modern Physics* 77.2 (June 2005), pp. 513–577. DOI: 10.1103/revmodphys.77.513.

[159] G. Adesso et al. “Continuous Variable Quantum Information: Gaussian States and Beyond.” In: *Open Systems & Information Dynamics* 21.01n02 (Mar. 2014), p. 1440001. DOI: 10.1142/s1230161214400010.

[160] M. V. Larsen et al. “Deterministic multi-mode gates on a scalable photonic quantum computing platform.” In: *Nature Physics* 17.9 (July 2021), pp. 1018–1023. DOI: 10.1038/s41567-021-01296-y.

[161] L. Lachman et al. “Faithful Hierarchy of Genuine n-Photon Quantum Non-Gaussian Light.” In: *Physical Review Letters* 123.4 (July 2019). DOI: 10.1103/physrevlett.123.043601.

[162] U. Chabaud et al. “Stellar Representation of Non-Gaussian Quantum States.” In: *Physical Review Letters* 124.6 (Feb. 2020). DOI: 10.1103/physrevlett.124.063605.

[163] U. Chabaud et al. “Certification of Non-Gaussian States with Operational Measurements.” In: *PRX Quantum* 2.2 (June 2021). DOI: 10.1103/prxquantum.2.020333.

[164] J.-W. Pan et al. “Multiphoton entanglement and interferometry.” In: *Reviews of Modern Physics* 84.2 (May 2012), pp. 777–838. DOI: 10.1103/revmodphys.84.777.

[165] A. E. Lita et al. “Counting near-infrared single-photons with 95% efficiency.” In: *Optics Express* 16.5 (2008), p. 3032. DOI: 10.1364/oe.16.003032.

[166] B. Calkins et al. “High quantum efficiency photon-number-resolving detector for photonic on-chip information processing.” In: OSA, 2013. DOI: 10.1364/cleo_qels.2013.qm4l.1.

[167] F. Marsili et al. “Detecting single infrared photons with 93% system efficiency.” In: *Nature Photonics* 7.3 (Feb. 2013), pp. 210–214. DOI: 10.1038/nphoton.2013.13.

[168] G. Harder et al. “Single-Mode Parametric-Down-Conversion States with 50 Photons as a Source for Mesoscopic Quantum Optics.” In: *Physical Review Letters* 116.14 (Apr. 2016). DOI: 10.1103/physrevlett.116.143601.

[169] I. A. Burenkov et al. “Full statistical mode reconstruction of a light field via a photon-number-resolved measurement.” In: *Physical Review A* 95.5 (May 2017). DOI: 10.1103/physreva.95.053806.

[170] J. Sperling et al. “Detector-Independent Verification of Quantum Light.” In: *Physical Review Letters* 118.16 (Apr. 2017). DOI: 10.1103/physrevlett.118.163602.

[171] M. Endo et al. “Quantum detector tomography of a superconducting nanostrip photon-number-resolving detector.” In: *Optics Express* 29.8 (Mar. 2021), p. 11728. DOI: 10.1364/oe.423142.

[172] B. Korzh et al. “Demonstration of sub-3 ps temporal resolution with a superconducting nanowire single-photon detector.” In: *Nature Photonics* 14.4 (Mar. 2020), pp. 250–255. DOI: 10.1038/s41566-020-0589-x.

[173] J. P. Höpker et al. “Integrated transition edge sensors on titanium in-diffused lithium niobate waveguides.” In: *APL Photonics* 4.5 (2019), p. 056103. DOI: 10.1063/1.5086276.

[174] J. Hloušek et al. “Accurate Detection of Arbitrary Photon Statistics.” In: *Physical Review Letters* 123.15 (Oct. 2019). DOI: 10.1103/physrevlett.123.153604.

[175] A. Tipsmark et al. “Experimental demonstration of a Hadamard gate for coherent state qubits.” In: *Physical Review A* 84.5 (Nov. 2011). DOI: 10.1103/physreva.84.050301.

[176] S. Ghose et al. “Non-Gaussian ancilla states for continuous variable quantum computation via Gaussian maps.” In: *Journal of Modern Optics* 54.6 (Mar. 2007), pp. 855–869. DOI: 10.1080/09500340601101575.

[177] S. Konno et al. “Nonlinear Squeezing for Measurement-Based Non-Gaussian Operations in Time Domain.” In: *Physical Review Applied* 15.2 (Feb. 2021). DOI: 10.1103/physrevapplied.15.024024.

[178] J. Yoshikawa et al. “Heralded creation of photonic qudits from parametric down-conversion using linear optics.” In: *Physical Review A* 97.5 (May 2018). DOI: 10.1103/physreva.97.053814.

[179] N. Sangouard et al. “Quantum repeaters with entangled coherent states.” In: *Journal of the Optical Society of America B* 27.6 (May 2010), A137. DOI: 10.1364/josab.27.00a137.

[180] Y.-S. Ra et al. “Non-Gaussian quantum states of a multimode light field.” In: *Nature Physics* 16.2 (Dec. 2019), pp. 144–147. DOI: 10.1038/s41567-019-0726-y.

[181] A. J. Pizzimenti et al. “Non-Gaussian photonic state engineering with the quantum frequency processor.” In: *Physical Review A* 104.6 (Dec. 2021). DOI: 10.1103/physreva.104.062437.

[182] C. N. Gagatsos et al. “Efficient representation of Gaussian states for multimode non-Gaussian quantum state engineering via subtraction of arbitrary number of photons.” In: *Physical Review A* 99.5 (May 2019). DOI: 10.1103/physreva.99.053816.

[183] C. N. Gagatsos et al. “Impossibility to produce arbitrary non-Gaussian states using zero-mean Gaussian states and partial photon number resolving detection.” In: *Physical Review Research* 3.4 (Dec. 2021). DOI: 10.1103/physrevresearch.3.043182.

[184] J. Provazník et al. “Benchmarking photon number resolving detectors.” In: *Optics Express* 28.10 (May 2020), p. 14839. DOI: 10.1364/oe.389619.

[185] F. M. Miatto et al. “Fast optimization of parametrized quantum optical circuits.” In: *Quantum* 4 (Nov. 2020), p. 366. DOI: 10.22331/q-2020-11-30-366.

[186] N. Killoran et al. “Strawberry Fields: A Software Platform for Photonic Quantum Computing.” In: *Quantum* 3 (Mar. 2019), p. 129. DOI: 10.22331/q-2019-03-11-129.

[187] B. Gupt et al. “The Walrus: a library for the calculation of hafnians, Hermite polynomials and Gaussian boson sampling.” In: *Journal of Open Source Software* 4.44 (Dec. 2019), p. 1705. DOI: 10.21105/joss.01705.

[188] T. R. Bromley et al. “Applications of near-term photonic quantum computers: software and algorithms.” In: *Quantum Science and Technology* 5.3 (May 2020), p. 034010. DOI: 10.1088/2058-9565/ab8504.

[189] L. Fox. “How to get meaningless answers in scientific computation (and what to do about it).” In: *Institute of Mathematics and its Applications Bulletin* 7 (1971), pp. 296–302.

[190] D. Goldberg. “What every computer scientist should know about floating-point arithmetic.” In: *ACM Computing Surveys* 23.1 (1991), pp. 5–48. DOI: 10.1145/103162.103163.

[191] N. J. Higham. *Accuracy and Stability of Numerical Algorithms*. Society for Industrial and Applied Mathematics, 2002. DOI: 10.1137/1.9780898718027.

[192] G. Dahlquist. *Numerical methods*. Mineola, N.Y: Dover Publications, 2003.

[193] M. Heath. *Scientific computing : an introductory survey*. Philadelphia, Pennsylvania: Society for Industrial and Applied Mathematics (SIAM), 2018.

[194] H. Paul et al. “Photon Chopping: New Way to Measure the Quantum State of Light.” In: *Physical Review Letters* 76.14 (Apr. 1996), pp. 2464–2467. DOI: 10.1103/physrevlett.76.2464.

[195] R. Filip et al. “Measurement-induced continuous-variable quantum interactions.” In: *Physical Review A* 71.4 (Apr. 2005). DOI: 10.1103/physreva.71.042308.

[196] Š. Bräuer et al. “Generation of quantum states with nonlinear squeezing by Kerr nonlinearity.” In: *Optics Express* 29.14 (July 2021), p. 22648. DOI: 10.1364/oe.427637.

[197] V. Kala et al. “Cubic nonlinear squeezing and its decoherence.” In: *Optics Express* 30.17 (Aug. 2022), p. 31456. DOI: 10.1364/oe.464759.

[198] M. Bohmann et al. “Incomplete Detection of Nonclassical Phase-Space Distributions.” In: *Physical Review Letters* 120.6 (Feb. 2018). DOI: 10.1103/physrevlett.120.063607.

[199] K. E. Cahill et al. “Density Operators and Quasiprobability Distributions.” In: *Physical Review* 177.5 (Jan. 1969), pp. 1882–1902. DOI: 10.1103/physrev.177.1882.

[200] H. Bateman. *Higher transcendental functions*. Malabar, Florida: R.E. Krieger Pub. Co, 1981.

[201] M. S. C. of the IEEE Computer Society. *IEEE Standard for Floating-Point Arithmetic*. Dec. 2008. DOI: 10.1109/ieeestd.2008.4610935.

[202] R. Barlow. *Statistics : a guide to the use of statistical methods in the physical sciences*. Chichester, England New York: Wiley, 1989.

[203] P. Bevington. *Data reduction and error analysis for the physical sciences*. Boston: McGraw-Hill, 2003.

[204] H. Robbins. “A Remark on Stirling’s Formula.” In: *The American Mathematical Monthly* 62.1 (1955), p. 26. DOI: 10.2307/2308012.

[205] Xanadu. *MrMustard: A differentiable bridge between phase space and Fock space*. GitHub repository https://github.com/jan-provaznik/witnessmess. 2022.

[206] N. J. Higham. “The Scaling and Squaring Method for the Matrix Exponential Revisited.” In: *SIAM Journal on Matrix Analysis and Applications* 26.4 (2005), pp. 1179–1193. DOI: 10.1137/04061101x.

[207] A. H. Al-Mohy et al. “A New Scaling and Squaring Algorithm for the Matrix Exponential.” In: *SIAM Journal on Matrix Analysis and Applications* 31.3 (2010), pp. 970–989. DOI: 10.1137/09074721x.

[208] G. Golub. *Matrix computations*. Baltimore: The Johns Hopkins University Press, 2013.

[209] V. Strassen. “Gaussian elimination is not optimal.” In: *Numerische Mathematik* 13.4 (1969), pp. 354–356. DOI: 10.1007/bf02165411.

[210] J. Provazník et al. “Adapting coherent-state superpositions in noisy channels.” In: *Under review* (2024). DOI: 10.48550/ARXIV.2406.01081.

[211] I. Straka et al. “Quantum non-Gaussian Depth of Single-Photon States.” In: *Physical Review Letters* 113.22 (Nov. 2014). DOI: 10.1103/physrevlett.113.223603.

[212] M. Mičuda et al. “Noiseless Loss Suppression in Quantum Optical Communication.” In: *Physical Review Letters* 109.18 (Nov. 2012). DOI: 10.1103/physrevlett.109.180503.

[213] C. N. Gagatsos et al. “Heralded noiseless amplification and attenuation of non-Gaussian states of light.” In: *Physical Review A* 89.6 (June 2014). DOI: 10.1103/physreva.89.062311.

[214] H. M. Chrzanowski et al. “Measurement-based noiseless linear amplification for quantum communication.” In: *Nature Photonics* 8.4 (Mar. 2014), pp. 333–338. DOI: 10.1038/nphoton.2014.49.

[215] R. Stárek et al. “Experimental quantum decoherence control by dark states of the environment.” In: *New Journal of Physics* 22.9 (Sept. 2020), p. 093058. DOI: 10.1088/1367-2630/abb47d.

[216] D. Leibfried et al. “Experimental Determination of the Motional Quantum State of a Trapped Atom.” In: *Physical Review Letters* 77.21 (Nov. 1996), pp. 4281–4285. DOI: 10.1103/physrevlett.77.4281.

[217] P. Bertet et al. “Direct Measurement of the Wigner Function of a One-Photon Fock State in a Cavity.” In: *Physical Review Letters* 89.20 (Oct. 2002). DOI: 10.1103/physrevlett.89.200402.

[218] K. Laiho et al. “Probing the Negative Wigner Function of a Pulsed Single Photon Point by Point.” In: *Physical Review Letters* 105.25 (Dec. 2010). DOI: 10.1103/physrevlett.105.253603.

[219] G. Kirchmair et al. “Observation of quantum state collapse and revival due to the single-photon Kerr effect.” In: *Nature* 495.7440 (2013), pp. 205–209. DOI: 10.1038/nature11902.

[220] K. Banaszek et al. “Direct measurement of the Wigner function by photon counting.” In: *Physical Review A* 60.1 (July 1999), pp. 674–677. DOI: 10.1103/physreva.60.674.

[221] H. Buhrman et al. “Quantum Fingerprinting.” In: *Physical Review Letters* 87.16 (Sept. 2001). DOI: 10.1103/physrevlett.87.167902.

[222] R. Filip. “Overlap and entanglement-witness measurements.” In: *Physical Review A* 65.6 (June 2002). DOI: 10.1103/physreva.65.062320.

[223] A. K. Ekert et al. “Direct Estimations of Linear and Nonlinear Functionals of a Quantum State.” In: *Physical Review Letters* 88.21 (May 2002). DOI: 10.1103/physrevlett.88.217901.

[224] K. L. Pregnell. “Measuring Nonlinear Functionals of Quantum Harmonic Oscillator States.” In: *Physical Review Letters* 96.6 (Feb. 2006). DOI: 10.1103/physrevlett.96.060501.

[225] M. Ozawa. “Entanglement measures and the Hilbert–Schmidt distance.” In: *Physics Letters A* 268.3 (2000), pp. 158–160. DOI: 10.1016/s0375-9601(00)00171-7.

[226] F. Nicacio et al. “Phase space structure of generalized Gaussian cat states.” In: *Physics Letters A* 374.43 (2010), pp. 4385–4392. DOI: 10.1016/j.physleta.2010.08.076.

[227] R. I. Booth et al. “Contextuality and Wigner Negativity Are Equivalent for Continuous-Variable Quantum Measurements.” In: *Physical Review Letters* 129.23 (Nov. 2022). DOI: 10.1103/physrevlett.129.230401.

[228] U. Chabaud et al. “Resources for Bosonic Quantum Computational Advantage.” In: *Physical Review Letters* 130.9 (Mar. 2023). DOI: 10.1103/physrevlett.130.090602.

[229] K. Miyata et al. “Experimental realization of a dynamic squeezing gate.” In: *Physical Review A* 90.6 (Dec. 2014). DOI: 10.1103/physreva.90.060302.

[230] K. Huang et al. “Engineering optical hybrid entanglement between discrete- and continuous-variable states.” In: *New Journal of Physics* 21.8 (Aug. 2019), p. 083033. DOI: 10.1088/1367-2630/ab34e7.

[231] B. Vlastakis et al. “Deterministically Encoding Quantum Information Using 100-Photon Schrödinger Cat States.” In: *Science* 342.6158 (2013), pp. 607–610. DOI: 10.1126/science.1243289.

[232] A. Omran et al. “Generation and manipulation of Schrödinger cat states in Rydberg atom arrays.” In: *Science* 365.6453 (Aug. 2019), pp. 570–574. DOI: 10.1126/science.aax9743.

[233] Y.-H. Chen et al. “Shortcuts to Adiabaticity for the Quantum Rabi Model: Efficient Generation of Giant Entangled Cat States via Parametric Amplification.” In: *Physical Review Letters* 126.2 (Jan. 2021). DOI: 10.1103/physrevlett.126.023602.

[234] I. Shomroni et al. “Optomechanical generation of a mechanical catlike state by phonon subtraction.” In: *Physical Review A* 101.3 (Mar. 2020). DOI: 10.1103/physreva.101.033812.

[235] H. Tan et al. “Generation of macroscopic quantum superpositions of optomechanical oscillators by dissipation.” In: *Physical Review A* 88.2 (Aug. 2013). DOI: 10.1103/physreva.88.023817.

[236] F.-X. Sun et al. “Remote Generation of Magnon Schrödinger Cat State via Magnon-Photon Entanglement.” In: *Physical Review Letters* 127.8 (Aug. 2021). DOI: 10.1103/physrevlett.127.087203.

[237] C. Flühmann et al. “Encoding a qubit in a trapped-ion mechanical oscillator.” In: *Nature* 566.7745 (2019), pp. 513–517. DOI: 10.1038/s41586-019-0960-6.

[238] Y. Miwa et al. “Exploring a New Regime for Processing Optical Qubits: Squeezing and Unsqueezing Single Photons.” In: *Physical Review Letters* 113.1 (July 2014). DOI: 10.1103/physrevlett.113.013601.

[239] J. Provazník et al. “Exponential improvement in the computational complexity of Fock capability of non-Gaussian Resources.” In: *In preparation* (Dec. 2024).

[240] O. Steuernagel. “Synthesis of Fock states via beam splitters.” In: *Optics Communications* 138.1-3 (1997), pp. 71–74. DOI: 10.1016/s0030-4018(97)00019-9.

[241] B. M. Escher et al. “Synthesis of arbitrary Fock states via conditional measurement on beam splitters.” In: *Physical Review A* 72.4 (Oct. 2005). DOI: 10.1103/physreva.72.045803.

[242] K. R. Motes et al. “Efficient recycling strategies for preparing large Fock states from single-photon sources: Applications to quantum metrology.” In: *Physical Review A* 94.1 (July 2016). DOI: 10.1103/physreva.94.012344.

[243] E. Diamanti et al. “Practical challenges in quantum key distribution.” In: *npj Quantum Information* 2.1 (Nov. 2016). DOI: 10.1038/npjqi.2016.25.

[244] P. Zapletal et al. “Multi-copy quantifiers for single-photon states.” In: *Scientific Reports* 7.1 (May 2017). DOI: 10.1038/s41598-017-01333-y.

[245] P. Zapletal et al. “Experimental Fock-state bunching capability of non-ideal single-photon states.” In: *Optica* 8.5 (May 2021), p. 743. DOI: 10.1364/optica.419230.

[246] M. Reck et al. “Experimental realization of any discrete unitary operator.” In: *Physical Review Letters* 73.1 (July 1994), pp. 58–61. DOI: 10.1103/physrevlett.73.58.

[247] U. Leonhardt. *Measuring Quantum State of Light*. Cambridge University Press, 1997.

[248] C. R. Harris et al. “Array programming with NumPy.” In: *Nature* 585.7825 (Sept. 2020), pp. 357–362. DOI: 10.1038/s41586-020-2649-2.

[249] E. Anderson et al. *LAPACK Users’ Guide*. Third. Philadelphia, PA: Society for Industrial and Applied Mathematics, 1999.

[250] J. Provazník et al. “Paving the way towards four photon optical states.” In: *In preparation* (Dec. 2024).

[251] P. Virtanen et al. “SciPy 1.0: fundamental algorithms for scientific computing in Python.” In: *Nature Methods* 17.3 (Feb. 2020), pp. 261–272. DOI: 10.1038/s41592-019-0686-2.

[252] M. Mičuda et al. “Verifying genuine multipartite entanglement of the whole from its separable parts.” In: *Optica* 6.7 (July 2019), p. 896. DOI: 10.1364/optica.6.000896.

[253] V. Nordgren et al. “Certifying emergent genuine multipartite entanglement with a partially blind witness.” In: *Physical Review A* 106.6 (Dec. 2022). DOI: 10.1103/physreva.106.062410.

[254] J. Provazník. *Witnessing multi-partite entanglement in Python*. GitHub repository https://github.com/jan-provaznik/witnessmess.

[255] J. Provazník. *NOMAD interface for Python*. GitHub repository https://github.com/jan-provaznik/nomadlad.

[256] A. Einstein et al. “Can Quantum-Mechanical Description of Physical Reality Be Considered Complete?” In: *Physical Review* 47.10 (May 1935), pp. 777–780. DOI: 10.1103/physrev.47.777.

[257] J. Zhang et al. “Continuous-variable Gaussian analog of cluster states.” In: *Physical Review A* 73.3 (Mar. 2006). DOI: 10.1103/physreva.73.032318.

[258] R. N. Alexander et al. “One-way quantum computing with arbitrarily large time-frequency continuous-variable cluster states from a single optical parametric oscillator.” In: *Physical Review A* 94.3 (Sept. 2016). DOI: 10.1103/physreva.94.032327.

[259] O. Gühne et al. “Entanglement detection.” In: *Physics Reports* 474.1-6 (2009), pp. 1–75. DOI: 10.1016/j.physrep.2009.02.004.

[260] C. H. Bennett et al. “Teleporting an unknown quantum state via dual classical and Einstein-Podolsky-Rosen channels.” In: *Physical Review Letters* 70.13 (Mar. 1993), pp. 1895–1899. DOI: 10.1103/physrevlett.70.1895.

[261] D. Boschi et al. “Experimental Realization of Teleporting an Unknown Pure Quantum State via Dual Classical and Einstein-Podolsky-Rosen Channels.” In: *Physical Review Letters* 80.6 (Feb. 1998), pp. 1121–1125. DOI: 10.1103/physrevlett.80.1121.

[262] D. Bouwmeester et al. “Experimental quantum teleportation.” In: *Nature* 390.6660 (Dec. 1997), pp. 575–579. DOI: 10.1038/37539.

[263] T. Feng et al. “Quantum information transfer between a two-level and a four-level quantum systems.” In: *Photonics Research* 10.12 (Nov. 2022), p. 2854. DOI: 10.1364/prj.461283.

[264] J. Yin et al. “Satellite-based entanglement distribution over 1200 kilometers.” In: *Science* 356.6343 (June 2017), pp. 1140–1144. DOI: 10.1126/science.aan3211.

[265] A. K. Ekert. “Quantum cryptography based on Bell’s theorem.” In: *Physical Review Letters* 67.6 (Aug. 1991), pp. 661–663. DOI: 10.1103/physrevlett.67.661.

[266] L. S. Madsen et al. “Continuous variable quantum key distribution with modulated entangled states.” In: *Nature Communications* 3.1 (Sept. 2012). DOI: 10.1038/ncomms2097.

[267] J. Yin et al. “Entanglement-based secure quantum cryptography over 1,120 kilometres.” In: *Nature* 582.7813 (June 2020), pp. 501–505. DOI: 10.1038/s41586-020-2401-y.

[268] F. Basso Basset et al. “Quantum key distribution with entangled photons generated on demand by a quantum dot.” In: *Science Advances* 7.12 (Mar. 2021). DOI: 10.1126/sciadv.abe6379.

[269] D. P. Nadlinger et al. “Experimental quantum key distribution certified by Bell’s theorem.” In: *Nature* 607.7920 (July 2022), pp. 682–686. DOI: 10.1038/s41586-022-04941-5.

[270] W. Zhang et al. “A device-independent quantum key distribution system for distant users.” In: *Nature* 607.7920 (July 2022), pp. 687–691. DOI: 10.1038/s41586-022-04891-y.

[271] B. Jungnitsch et al. “Taming Multiparticle Entanglement.” In: *Physical Review Letters* 106.19 (May 2011). DOI: 10.1103/physrevlett.106.190502.

[272] P. Hyllus et al. “Optimal entanglement witnesses for continuous-variable systems.” In: *New Journal of Physics* 8.4 (Apr. 2006), pp. 51–51. DOI: 10.1088/1367-2630/8/4/051.

[273] L. Vandenberghe et al. “Semidefinite Programming.” In: *SIAM Review* 38.1 (1996), pp. 49–95. DOI: 10.1137/1038003.

[274] N. Miklin et al. “Multiparticle entanglement as an emergent phenomenon.” In: *Physical Review A* 93.2 (Feb. 2016). DOI: 10.1103/physreva.93.020104.

[275] M. Paraschiv et al. “Proving genuine multiparticle entanglement from separable nearest-neighbor marginals.” In: *Physical Review A* 98.6 (Dec. 2018). DOI: 10.1103/physreva.98.062102.

[276] G. Van Rossum et al. *Python 3 Reference Manual*. Scotts Valley, CA: CreateSpace, 2009.

[277] G. Sagnol et al. "PICOS: A Python interface to conic optimization solvers." In: *Journal of Open Source Software* 7.70 (Feb. 2022), p. 3915. DOI: 10.21105/joss.03915.

[278] M. Andersen et al. *CVXOPT: Convex Optimization*. Astrophysics Source Code Library, record ascl:2008.017. Aug. 2020.

[279] M. ApS. *The MOSEK optimization toolbox for Python manual. Version 10.1*. 2024.

[280] C. Audet et al. "Algorithm 1027: NOMAD Version 4: Nonlinear Optimization with the MADS Algorithm." In: *ACM Transactions on Mathematical Software* 48.3 (Sept. 2022), pp. 1–22. DOI: 10.1145/3544489.

[281] C. Audet et al. "Mesh Adaptive Direct Search Algorithms for Constrained Optimization." In: *SIAM Journal on Optimization* 17.1 (2006), pp. 188–217. DOI: 10.1137/040603371.

[282] C. Audet et al. *Derivative-Free and Blackbox Optimization*. Springer International Publishing, 2017. DOI: 10.1007/978-3-319-68913-5.

[283] J. Provazník. *Partial trace and partial transposition for Kronecker representation of multi-partite discrete variable quantum systems*. GitHub repository https://github.com/jan-provaznik/departed.